

The Degradation in Creep Strength of ASME Grade 122 Steel

Manabu TAMURA¹ & Fujio ABE²

¹ 6-45-2 Hiniminami, Konan-ku, Yokohama, 2340055, Japan

² National Institute for Materials Science, 1-2-1 Sengen Tsukuba 3050047, Japan

Correspondence: Manabu TAMURA, 6-45-2 Hiniminami, Konan-ku, Yokohama, 234-0055, Japan. E-mail: mtamura.1943@pep.ne.jp

Received: May 21, 2023

Accepted: June 20, 2023

Online Published: July 10, 2023

doi:10.5539/jmsr.v12n2p1

URL: <https://doi.org/10.5539/jmsr.v12n2p1>

Abstract

The degradation of the long-term rupture strength of ASME Grade 122 steel occurs earlier than that of Grade 92 steel. To investigate the reasons for this phenomenon, the long-term creep curves of Grade 122 steel pipe, plate, and tube product forms were analyzed by applying an exponential law to the temperature, stress, and time parameters. The activation energy (Q), activation volume (V), and Larson–Miller constant (C) were obtained as functions of creep strain. All Q , V , and C (QVC) decreased simultaneously with an increase in creep strain during the transient creep in a data group (*Gr.IIIa*), where an unexpected drop in the long-term rupture strength was experienced. Metallurgical considerations of the variations in QVC meant that “heterogeneous recovery and heterogeneous deformation” (HRHD) should occur during the simultaneous decreases in QVC . The Z-phase is easily formed by the consumption of the strengthening particles of MX in the HRHD zone, which causes the degradation of the long-term strength of Grade 122 steel. The higher hardness of Grade 122 steels promotes the coarsening of the Laves phase particles and, in addition to this, the amount of MX inside the subgrains is estimated to be less than Grade 92 steel, which cause severe HRHD and the resultant degradation in rupture strength compared to Grade 92 steel. In a data group subjected to lower stresses than those of *Gr.IIIa*, the degradation rate is mitigated, and a deformation mechanism was proposed. The improvement in the long-term rupture strength of Grade 122 steel was also discussed.

Keywords: creep, degradation mechanism, exponential law, Grade 92, Grade 122, long-term rupture strength

1. Introduction

The development of high-strength high-Cr martensitic heat-resistant steel has rapidly grown since the proposal of 9Cr-1Mo-VNbN steel (now registered in ASME as Grade 91 steel) by Sikka, Cowgill, and Roberts (1983). Since the development of such high-strength martensitic steel, the unexpected degradation of the base metal during creep test longer than several tens of thousands of hours has surfaced (Kushima, Kimura, & Abe, 1999; Sawada, Kushima, Kimura, & Tabuchi, 2007). However, since the development of Grade 92 steel, whose degradation is not so severe at 600 °C (Hasegawa, 2014), it has been widely used in many power stations, which reduces its contribution to global warming (Masuyama, 2001; Kimura, Sato, Bergins, Imano, & Saito, 2011; Muroki, 2017).

Grade 122 steel was originally developed to exhibit higher oxidation resistance than Grade 92 steel (Iseda et al., 1988; Masuyama et al., 1998). However, the long-term rupture strength of Grade 122 steel degrades much earlier than that of Grade 92 steel (Kimura & Takahashi, 2012a; Maruyama, Nakamura, & Yoshimi, 2015; Tamura, 2015).

Many researchers (Kushima et al., 1999; Suzuki, Kumai, Kushima, Kimura, & Abe, 2003; Sawada, Kushima, & Kimura, 2006; Danielsen, 2007; Hald, 2008; Kimura, Sawada, Kushima, & Toda, 2013) agree that the primary cause of the unexpected degradation in the long-term rupture strength of martensitic high-strength steel is the partial disappearance of the finely dispersed strengthening factor of MX due to the formation of the Z-phase. Here, MX represents carbonitride with a cubic structure; M indicates metallic elements such as V, Nb, and Cr; and X indicates C, N, or both.

To investigate the root causes of the unexpected degradation in the long-term rupture strength of martensitic high-strength steel, Tamura and Abe (Tamura & Abe, 2021a; 2021b; Tamura, 2022) analyzed the creep curves of Grades 91 and 92 steel as well as 9Cr-1W and 9Cr-4W experimental steels, by applying an exponential law to the temperature, stress, and time parameters. The parameters of QVC were obtained as functions of creep strain

without using adjustable parameters and the variations in QVC with strain were discussed based on metallurgical considerations, which led to the following conclusions:

- 1) Subgrain boundary strengthening based on the swept-out dislocations (SBSD) from subgrains is an essential process during the initial creep stage of martensitic steel. The hardening caused by the dissolution, the dissolving and finely re-precipitation (DFRP) of $M_{23}C_6$ particles, and the precipitation of the Laves phase are added to the SBSBD for high-Cr high-strength martensitic steel, which increases QVC and consequently decreases the strain rate with increasing strain.
- 2) After the QVC peaks, the heterogeneous recovery and simultaneous heterogeneous deformation (HRHD) should begin at an early stage of transient creep in the vicinity of several of the weakest boundaries owing to the occasional coarsening of the Laves phase. This triggers an unexpected degradation in the long-term rupture strength owing to the easy formation of the Z-phase in the HRHD zone, which consumes finely dispersed MX particles.

The driving force behind Z-phase formation in 12Cr steel is larger than that in 9Cr steel when in equilibrium (Kocer, Abe, & Soon, 2009). Therefore, the Z-phase should form earlier in 12Cr steel than in 9Cr steel, as was confirmed by Sawada et al. (2007), using ruptured specimens. However, Sawada, Kushima, Hara, Tabuchi, and Kimura (2014) also showed that the driving force behind Z-phase formation does not always cause the unexpected degradation in the long-term rupture strength of Grade 91 steel.

Therefore, the long-term creep curves for Grade 122 steel were analyzed by applying an exponential law, and the QVC variations calculated as functions of strain were interpreted according to the above-mentioned conclusions obtained for Grades 91 and 92 steel. Based on the study findings and metallurgical knowledge, the reasons for lowering the long-term rupture strength of Grade 122 steel were clarified, and the countermeasures to mitigate the unexpected degradation in the long term-rupture strength of Grade 122 steel are discussed.

2. Analysis Method

2.1 Calculation of Q , V , and C

The calculation method has been described in detail in previous works (Tamura & Abe, 2021a; 2021b; Tamura, 2022) and is briefly explained here. The time to rupture (t_r) or time to a specific strain (t_ε), where ε is strain in %, can be expressed as

$$t_r \text{ or } t_\varepsilon = 10^{-C} \exp\{(Q - \sigma V)/RT\}, \quad (1)$$

where R , T , and σ are the gas constant, absolute temperature (K), and applied normal tensile stress under uniaxial loading, respectively (Tamura et al., 1999). Equation 1 can be rearranged as

$$\log(t_r \text{ or } t_\varepsilon) = Q/2.3R \cdot 1/T - V/2.3R \cdot \sigma/T - C = [Q] - [V] - C. \quad (2)$$

Based on Equation 2, the regression analysis of $\log(t_r \text{ or } t_\varepsilon)$ as a function of $1/T$ and σ/T yields three parameters: Q , V , and C using an Excel software. In Equation 2, $[Q] = Q/2.3RT$ and $[V] = \sigma V/2.3RT$ are absolute numbers used in the subsequent sections. The Larson–Miller constant C (Larson & Miller, 1952) can be calculated as the third term in Equation 2, and it is well-known that the value of C is ~ 20 for many heat-resistant steels when the units for the test temperature and t_r or t_ε are Kelvin and hours, respectively (Tamura, Abe, Shiba, Sakasegawa, & Tanigawa, 2013). Typically, C is treated as an absolute number; therefore, the units for C are omitted in this study.

The Q and V in Equation 1 represent the apparent activation energy and apparent activation volume at rupture or a specific strain, respectively. For simplicity, we refer to those as activation energy and activation volume, respectively. Typically, the σ vs. t_r data are plotted in a double logarithmic diagram based on Norton law (Norton, 1929). However, for Equation 1 or 2, a linear relationship for the σ - $\log t$ is obtained in a semi-logarithmic diagram, where the x-axis indicates the logarithm of t_r or t_ε and the y-axis indicates linear stress. Tamura, Esaka, and Shinozuka (1999) confirmed that when rupture data for several heat-resistant steels are classified into two or three groups based on their test conditions, the rupture data for each group satisfies Equation 1. A technical merit of applying an exponential law to rupture data is that it is easy to estimate the long-term rupture strength by extrapolating the linear relationship obtained from a specific data group. This is performed using Equation 1 in a semi-logarithmic diagram to a given test condition beyond the test conditions of the data group. Alternatively, estimation can be performed graphically because the regression lines at different temperatures obtained using Equation 2 are approximately parallel.

To study the creep phenomena throughout the entire duration of the creep life of the investigated materials, it is necessary to investigate the variations in the creep rate. The strain rate $\dot{\epsilon}(\epsilon_i)$ at a strain of ϵ_i , where i denotes the order number from the minimum strain reported in the referred datasheets, is calculated as

$$\dot{\epsilon}(\epsilon_i) = (\epsilon_i - \epsilon_{i-1}) / (t_i - t_{i-1}), \quad (3)$$

where t_i is the time to the i^{th} strain.

The accuracy of the strain rate calculated using Equation 3 is not very high because the strain intervals used in this study are rather large. In particular, the accuracy of creep rates near the minimum creep rate may be insufficient because the strain rate near the minimum creep rate is small. In addition, the sign of increasing strain rate changes from negative to positive with increasing creep strain. Furthermore, creep rates immediately before rupture are calculated utilizing t_r data and rupture elongation (EL); however, the strain rates are largely affected by necking for $t_\epsilon/t_r > 0.9$ (Lim et al., 2011). Despite these problems, the creep curves of Grade 122 can be satisfactorily interpreted with the aid of metallurgical knowledge gathered from previous studies.

When similar analyses like Equations 1 and 2 are performed on the strain rates obtained using Equation 3, following equations are obtained:

$$\dot{\epsilon} = 10^{C_s} \exp\{-(Q_s - \sigma V_s) / RT\}, \quad (4)$$

and

$$\log(\dot{\epsilon}) = -[Q_s] + [V_s] + C_s, \quad (5)$$

where Q_s, V_s , and C_s ($[QVC]_s$) correspond to QVC , respectively. Here, $[Q_s]$ and $[V_s]$ have similar meanings as $[Q]$ and $[V]$, respectively.

2.2 Physical and Metallurgical Meanings of Q , V , and C

2.2.1 Time-Temperature Parameter

Kimura (2009) reviewed the prediction methods for the creep-rupture life of heat-resistant steels. In many cases, a time-temperature parameter such as the Larson–Miller parameter $P = T(\log t_r + C)$ is regarded as a function of σ , and a long-term rupture strength is estimated by conducting multiple regression analyses. In this case, plural numbers of adjustable parameters, including C , are required to fit the data closely. In this approach, even C is treated as one of the adjustable parameters. The physical and metallurgical meanings of these adjustable parameters cannot be completely understood; therefore, the variations in rupture strength do not reasonably correlate with changes in the microstructure. However, Equation 1 indicates three experimental variables, T , σ , and t_r or t_ϵ , can be converted to three variables of QVC without using additional adjustable parameters. Therefore, QVC should have specific physical and metallurgical meanings.

2.2.2 Activation Energy

For a model based on crystallography, Q is defined as the magnitude of the energy barrier that must be overcome for a dislocation in an activation process. However, Q calculated from Equation 2 is the apparent activation energy calculated from the measurable and macroscopic variables T , σ , and t_r or t_ϵ . Therefore, the value of Q is obtained assuming that C does not depend on T . Thus, Q contains not only the magnitude of the average gliding resistance to mobile dislocations, but also the effect of the temperature dependence of C (Schoeck, 1980). In addition, Q contains the effect of the back stress against a moving dislocation caused by the grain boundaries, sub-boundaries, and stress fields arising from other dislocations and precipitates (Tamura, Esaka, & Shinozuka, 2000). Therefore, the Q decreases because of the reduction of the back stress when the subgrains grow, the dislocation density decreases, and the precipitates are coarsened during long-term creep at high temperatures. Here, subgrain refers to the minimum region in which identical slip systems are operating. Thus, subgrains denote the lath martensite, block, packet, and subgrain itself. However, the value of Q of martensitic steel does not decrease without limits. It is established that the value of Q in the high-temperature creep of materials is approximately equivalent to the activation energies for self-diffusion (Sherby, Orr, & Dorn, 1953; Tamura, 2017); therefore, the lower limit of Q approximately approaches that for the self-diffusion of the α -iron, i.e., 267 kJmol^{-1} (Oikawa, 1982). The magnitude of the back stress can also be roughly estimated using an exponential law; the details are discussed in a previous paper (Tamura & Abe, 2021b).

2.2.3 Activation Volume

From Equation 2, V is formulated as

$$V = -2.3RT(\partial \log t_r / \partial \sigma)_T. \quad (6)$$

Thus, the magnitude of V is visually understood in a semi-logarithmic diagram of the $\sigma - \log t_r$ relationship because V is inversely proportional to the magnitude of the slope of the $\sigma - \log t_r$ relationship at a constant temperature, where the x-axis means $\log t_r$. The term σV in Equation 1 is equal to the work performed by a specimen on a loading system in an activated state, or the potential drop of the loading system (Esheryby, 1956; Mura & Mori, 1976). In addition, the potential drop is equal to the force on a dislocation τb times the area swept out of the dislocation in an activated state, where τ denotes a shear stress on a slip plane and is proportional to σ and b is the length of Burgers vector. The V generally increases after long-term creep and/or at high temperatures because the swept-out area by dislocation motion increases inside a subgrain when the size of a subgrain increases or the densities of obstacles for a dislocation decrease because of recovery (Tamura et al., 2000). However, we frequently observe a decrease in V with an increase in strain during creep and this should be caused by phenomena which decrease the mobile area of a dislocation such as precipitation hardening inside subgrains.

2.2.4 Larson–Miller Constant

The Larson–Miller constant C can be calculated as the third term in Equation 2, and it is well-known that the value of C is ~ 20 for many heat-resistant steels (Tamura et al. 2013). The Larson–Miller constant is regarded as a function of

$$C = \log(\rho \lambda v_{\text{eff}} b / 2C_{\text{MG}}) + \Delta S / 2.3R, \quad (7)$$

where ρ , C_{MG} , λ , v_{eff} , and ΔS denote the dislocation density that contributes creep strain, Monkman–Grant constant (Monkman & Grant, 1956), maximum distance that a dislocation can move from a starting point to the next stable position through the activation process, effective attempt frequency per unit time to overcome the obstacles, and entropy change involved in the activation process, respectively (Tamura et al., 2013). Although the first term of Equation 7 depends on ρ , the value of the first term of Equation 7 is approximately 13 for typical heat-resistant steels (Tamura & Abe, 2021a; 2021b). Therefore, the second term of the entropy term is approximately $20 - 13 = 7$ for $C = 20$, a part of which corresponds to the entropy change related to the formation and migration of vacancies during creep controlled by self-diffusion. High values of C (> 30) are reported for many martensitic steels with high-strength. The increase in C is caused by an increase in the entropy term of Equation 7 because the increase in the first term caused by the high dislocation density of martensitic steel with high strength is not large (Tamura & Abe, 2021a).

Moving dislocations experience not only the applied stress but also the back stress arising from the surroundings. Simultaneously, the surroundings are affected by the stress fields of the moving dislocations. However, these influences and the kinetic energy of the moving dislocations are irrelevant to the observed creep strain. Therefore, these energies are treated as heat loss in the system at a constant temperature when we analyze $\dot{\epsilon}$ and t_r , assuming a thermally activated process. The heat loss is accounted for in the formulation of the Gibbs free energy as entropy change, i.e., as a part of C . Furthermore, the influence of the back stress is accounted for in Q as the barrier to be overcome. Therefore, both Q and C increase with increasing dislocation density and the formation of finer substructures. Consequently, the values of Q and C for martensitic steels are large—typically $Q = 800 \text{ kJmol}^{-1}$ and $C = 35$. In contrast, both Q and C are small when the dislocation density is low and the subgrain size (d) increases after long-term creep. In extreme cases, the values of Q and C for the creep of a single crystal of pure iron are calculated as 294.0 kJmol^{-1} and 12.06 , respectively, from the analysis of creep data reported by Karashima, Iikubo, Watanabe, and Oikawa (1971).

However, the value of C does not decrease without limits. It is established that dislocations can move with the help of vacancies (Sherby et al., 1953; Tamura, 2017). Therefore, the lower limit of C approaches $\Delta S / 2.3R$ based on the nucleation and migration of vacancies, when the first term of Equation 7 is zero, i.e., $\rho = 1 \text{ m}^{-2}$, and the entropy change caused by the dislocation motion can be neglected. The entropy change caused by the nucleation and migration of single vacancies relates to the pre-factor of self-diffusion (Mehrner, 2007) as

$$D_0 = Z/6 \cdot a^2 v \cdot \exp(\Delta S/R), \quad (8)$$

where Z , a , and v are the coordinate number, interplanar spacing, and thermal frequency, respectively. Substituting $a=2.5\text{E}-10 \text{ m}$, $Z=8$, and $v=1\text{E}13 \text{ s}^{-1}$ into Equation 8, the entropy change for self-diffusion is estimated to be $\Delta S = 6.0R$ for α -Iron (Tamura et al., 2013) and thus, the contribution to the second term of Equation 7 owing to self-diffusion is small, i.e., $\Delta S/2.3R \sim 2.6$. However, when the dislocation density increases, the first and second terms of Equation 7 increase and, therefore, $C \gg 2.6$.

The values of Q and C for the creep of the polycrystals of pure iron are calculated as 259.2 kJmol^{-1} and 10.94 , respectively from the creep data reported by Karashima, Iikubo, and Oikawa (1972). Moreover, the values of $Q = 259.2 \text{ kJmol}^{-1}$ and $C = 18.56$ for 0.2% carbon steel (Tamura et al., 2013) and $Q = 418 \text{ kJmol}^{-1}$ and $C =$

20.99 as the average for three heats of 0.5Cr-0.5Mo steel (Tamura et al., 1999) were obtained. For many heat-resistant steels, $C \sim 20$ is confirmed and the value of C for the creep of the studied martensitic heat-resistant steels is considerably larger, i.e., $C > 30$. This is because martensitic steels contain many dislocations and possess extremely fine sub-structures. Therefore, energy loss, i.e., an increase in entropy, becomes considerably large for the dislocation movements. The changes in C can largely be regarded as changes in the entropy term of $\Delta S/2.3R$ in Equation 7 when martensitic sub-structures are maintained even after the long-term creep of high-Cr martensitic steel exhibiting high strength properties.

2.2.5 Inter-Relationships Among Q , V , and C

Even though Q is an important parameter for creep strength, it is not always true that the creep strength is high when Q is large. This is because it is found from Equation 1 that the t_r is the product of an extremely large value, i.e., $\exp\{(Q - \sigma V)/RT\}$, and an extremely small value of 10^{-C} . Since Q is large compared to σV , Q and C should have a strong positive correlation. Tamura and Abe confirmed that the two parameters Q and C have a considerably strong positive correlation (2021b); however, Q and C have the different meanings.

Q denotes the magnitude of the barrier that must be overcome for a moving dislocation which is caused by nearby precipitates, dislocations, and boundaries throughout the entire specimen. However, V is also an important parameter for creep, whereas V is a factor reflecting the movable area applicable to a dislocation. Namely, V is a parameter that only relates to the microstructures inside the subgrains, which is essentially different from Q .

2.3 Heterogeneous Deformation

In early stages of creep of high-strength martensitic steel, QVC increases simultaneously with an increase in strain, which is caused by a combination of SBS, DFRP of $M_{23}C_6$ carbides, and the precipitation of Laves phase (Tamura & Abe, 2021a; 2021b; Tamura, 2022). Frequently we can also observe simultaneous decreases in QVC with an increase in strain even during the early stages of transient creep (Tamura & Abe, 2021a; 2021b; Tamura, 2022). However, it may be impossible to successfully explain the simultaneous decreases in QVC from a general metallurgical sense of perspective.

The QVC s for the ruptured specimens of the welded joint for high-strength martensitic steel are smaller than those for both the parent metal and the material, where the heat history simulates the heat-affected zone of the welded joint (Tamura & Abe, 2021a). The welded joints deform nonuniformly under low stresses. Therefore, it is intuitive that nonuniform deformation, i.e., HRHD, starts to occur even during early stages of transient creep of high-strength martensitic steel when QVC decreases simultaneously. The HRHD zone mentioned here indicates heterogeneity on a microscopic scale, unlike a heat-affected zone of the welded joint. Kushima et al. (1999) reported that the extremely recovered zone in the vicinity of the prior austenite grain boundaries (PAGBs) with a width of approximately 1 μm was formed in a ruptured specimen of Grade T91 tested at 600 °C under 100 MPa ($t_r = 34$ 141 h), where the unexpected drop in rupture strength was clearly confirmed. Experimentally, a locally recovered zone is observed also in the crept specimens for accelerating creep near the minimum creep rate point of Grade T91 (Kimura, Suzuki, Toda, Kushima, & Abe, 2002).

The stress and strain surrounding large particles near the boundaries are concentrated; therefore, the recovery and degradation of the microstructure are promoted, which is an embryo of the HRHD zone. In a developed HRHD zone, recovery and mass transfer is promoted because of the strain concentration, and large particles of the Laves phase, $M_{23}C_6$, and Z-phase are occasionally formed on the boundaries. These large particles lead to larger or newly formed HRHD zones. This vicious cycle degrades the long-term rupture strength of high-strength martensitic steel consuming strengthening particles of MX, the details of which are shown in the previous studies (Tamura & Abe, 2021a; 2021b; Tamura, 2022). The simultaneous decreases in QVC with an increase in strain during the stress and strain concentrations and the microstructural degradations in the HRHD zone can be simulated using Equation 1 or 3 (Tamura & Abe, 2021a). Experimentally, the simultaneous decreases in QVC are observed from a later stage of transient creep of 9Cr-4W steel and from the extremely early stage of transient creep of Grade 91 and 92 steels at approximately 600 °C under low stresses. For these cases, HRHD should start to occur during transient creep, although a microstructural investigation is not yet performed (Tamura & Abe, 2021b).

Therefore, in this study, the assertion that HRHD occurs when QVC simultaneously decreases with an increase in strain even during transient creep is made. When the unexpected degradation of long-term rupture strength is observed, QVC start to decrease from the onset of creep and decrease to considerably low values with an increase in creep strain. Thereafter, they remain approximately flat until rupture. These cases are referred to as severe or significant HRHD. The severe or significant HRHD means the roughly two cases that the number of HRHD zones increases and/or the average area of the HDHR zones is enlarged.

3. Materials and Notation

Recent creep data for ASME Grade 122 steel have been reported in NIMS Creep Data Sheet No. 51B (2020) and No. 52B (2021). Table 1 shows the product form, thermal history, prior austenite grain-size number (PAGSn), hardness (Rockwell hardness C scale; HRC), and chemical composition (percentage by mass (%)) of the steels analyzed: T122/RHU, P122/RHQ, pl-122/RhA, and DTB/RHT, where RHU, RHQ, RhA, and RHT are NIMS reference code names given for a single heat. In this study the results for Grades 91 and 92 (Tamura & Abe, 2021b; Tamura, 2022) are also quoted as references. To conform to the ASME standard and NIMS code name, the convention of T91/MGC for a tube, pl-91/MgC for a plate, T92/MJT for a tube, and P92/MJP for a pipe were used as steel names for Grades 91 and 92 steel in addition to the steel names mentioned above. In addition, the results for the laboratory prepared 9Cr-1W and 9Cr-4W steels are referred to (Tamura & Abe, 2021a). The abbreviated names, 1W, 4W, MGC, MgC, MJP, MJT, RHU, RHQ, RhA, and RHT are also frequently used. The term Grade 122 is also used, and it indicates a general term for four heats of RHU, RHQ, RhA, and RHT. In addition, the terms Grade 91 and Grade 92 are used, which indicate a general term for two heats of MGC and MgC and that of MJT and MJP, respectively. However, when referring to the previous works or generally descriptions of the scientific facts, for example Grade T91, ASME Grade 91, or Type 91 are used.

Table 1. Characteristics of materials analyzed. The chemical composition is given in mass %. PAGS means prior austenite grain size.

| Steel | T122/RHU | P122/RHQ | pl-122/RhA | DTB122/RHT |
|------------------|----------|----------|------------|------------|
| Product form | Tube | Pipe | Plate | Tube |
| Normalizing (°C) | 1050 | 1050 | 1050 | 1050 |
| Tempering (°C) | 770 | 770 | 770 | 790 |
| PAGS number | 5.8 | 4.6 | 6.8 | 9.2 |
| Hardness, HRC | 20 | 19 | 18 | 20 |
| C | 0.13 | 0.12 | 0.12 | 0.11 |
| Si | 0.31 | 0.30 | 0.24 | 0.27 |
| Mn | 0.60 | 0.60 | 0.63 | 0.59 |
| Ni | 0.38 | 0.32 | 0.36 | 0.33 |
| Cu | 0.86 | 0.85 | 0.97 | 0.82 |
| Cr | 10.85 | 10.62 | 10.73 | 12.10 |
| Mo | 0.33 | 0.34 | 0.38 | 0.34 |
| W | 1.87 | 1.89 | 1.97 | 1.82 |
| V | 0.19 | 0.19 | 0.22 | 0.19 |
| Nb | 0.05 | 0.05 | 0.056 | 0.06 |
| N | 0.057 | 0.054 | 0.072 | 0.066 |
| B | 0.0024 | 0.0029 | 0.0039 | 0.0030 |
| Al | 0.007 | 0.007 | 0.006 | 0.016 |

Prior to creep testing, the Grade 122 was composed of tempered martensite with $M_{23}C_6$ and MX particles (Iseda et al., 1988; Sawada et al., 2006), where M of $M_{23}C_6$ denotes metallic elements such as Cr, Fe, W, and Mo, and MX is (Nb,V,Cr)(C,N) with a cubic structure. The phase calculation of Grade 122 using a thermodynamic data calculation system (Sundman, Jansson, & Andersson, 1985) indicated that MX particles are composed of MX with high Nb content and MX with high V content, where Nb-rich MX and V-rich MX are formed during normalizing and tempering, respectively. BN was also considered to form prior to creep testing according to the solubility product of B and N in austenite (Abe et al., 2007a). DTB122/RHT is tubing with 12% Cr and contains approximately 5 % of δ -ferrite and coarse particles of Cr_2N , as well as $M_{23}C_6$ and MX (Sawada et al., 2006).

Sawada et al. (2006; 2007) reported that during creep and/or creep exposure of T122/RHU and DTB122/RHT coarse particles of Z-phase are formed around PAGBs and/or packet boundaries for both steels, as well as around

matrix/ δ -ferrite boundaries for RHT consuming finely dispersed MX particles. Iseda et al. (1988) reported that the Laves phase is formed during high temperature services at an actual power boiler for 21 956 h of similar steel with 30 % δ -ferrite to RHT, and reported that plate-like precipitates of VN are finely dispersed in δ -ferrite which stabilizes the long-term rupture strength of this steel.

Six parameters formulated in Equation 1 (T , σ , t , and QVC) for Grade 122 are fully explained in this paper and symbols such as σ_{XX} , t_{XX} , Q_{XX} , V_{XX} , and C_{XX} are frequently used. Here, suffixes XX denote strain in %, material name (ex., T91, T92, T122, RHU, RHQ, 1W, and 4W), time in h, or a name of data group (*I*, *II*, *III*, etc.). For example, $\sigma_{0.5}$, σ_{1E5} , and σ_{IIIa} represents the strengths for $\varepsilon = 0.5\%$, 1E5 h, and *Gr.IIIa*, respectively.

4. Analysis Results

4.1 Time to Rupture and Analysis of Creep Curves for T122/RHU

Figure 1 shows the $\sigma - t_r$ relationship for T122/RHU (NIMS, 2020). The data were classified into seven groups, *Gr.I-IV*. In the classification, the $\sigma - t_r$ relationships for Grades 91 and 92 (Tamura & Abe, 2021b; Tamura, 2022) and the $\sigma - t_\varepsilon$ relationships for Grade 122/RHU were referred to. Creep tests were conducted at 25 °C intervals; however, test temperatures were only shown for 50 °C intervals (this documentation is the same for other similar diagrams and is hereinafter omitted). The regression analyses for each data group were made using Equation 2 and the regression lines are shown in the figure using the QVC s. The degradation behavior at 600 °C from *Gr.I* to *Gr.IV* is similar to those of Grades 91 and 92: *Gr.I* is positioned at low temperatures and high stresses and the creep behavior of *Gr.I* is directly affected by the initial microstructure. The t_r of *Gr.II* is longer than that estimated from the data of *Gr.I*. This hardening is caused by the precipitation of the Laves phase. The rupture strength breakdown in *Gr.IIIa* is the most significant; that is, the slope $\Delta\sigma/\Delta\log t_r$ is the steepest. The degradation of t_r for *Gr.IIIa* is primarily caused by the formation of the Z-phase which consumes the strengthening particles of MX (Tamura & Abe, 2021b; Tamura, 2022).

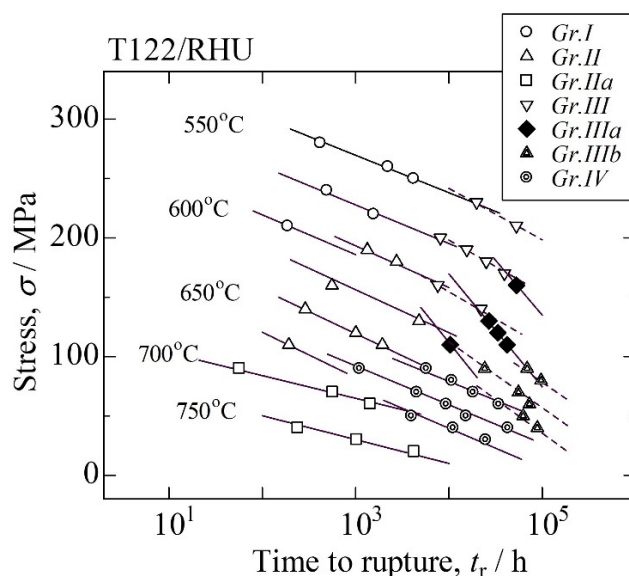


Figure 1. Stress vs. time to rupture relationship for T122/RHU and regression lines for each data group

The strain rate was calculated using Equation 3. Figure 2 shows the relationship between the strain and the average normalized creep rate (NCR) plotted in a double logarithmic diagram, where NCR is the average strain rate at a specific strain is divided by the minimum creep rate (MCR) for each data group. In the figure, the strain on the far right for each group is the average of the EL (the same, hereafter, but the explanation is omitted). In Figure 2, characteristics of each group are clearly shown. That is, the slope, $\Delta\log(\text{average NCR}) / \Delta\log\varepsilon$, is steep for *Gr.IIIa* at an early stage of transient creep; resultantly, the increasing rate of NCR in accelerating creep is high as compared to those of other data groups. In contrast, the NCR at $\varepsilon = 0.5\%$ in the transient creep of *Gr.IIIb* is the lowest, or the initial hardening rate at $\varepsilon < 0.5\%$ may be high. Additionally, the recovery rate, i.e., NCR at $\varepsilon = 2\%$ in accelerating creep, becomes high as compared to *Gr.IIIa*. However, the increasing rate of NCR for *Gr.IIIb*

is slower than that of *Gr.IIIa*, which should be related to the longer t_r s of *Gr.IIIb* than those estimated from the data in *Gr.IIIa* as seen in Figure 1.

Table 2 shows the average test temperature (T), stress (σ), time to strain (t_ε ($\varepsilon = 0.5, 1, 2,$ and 5%)), time to rupture (t_r), and MCR for each data group of T122/RHU. The start time for Laves phase formation TLF, and start time for Z-phase formation TZF are also shown in Table 2. The TLFs are estimated from the time-temperature-precipitation (TTP) curve for the Laves phase of Fe_2W formed in aged specimens of 8Cr-2WVTa steel (Tamura, Hayakawa, Yoshitake, Hishinuma, & Kondo, 1988). The TZFs are estimated from the TTP curve for the Z-phase obtained using rupture specimens of T122/RHU (Sawada et al., 2006).

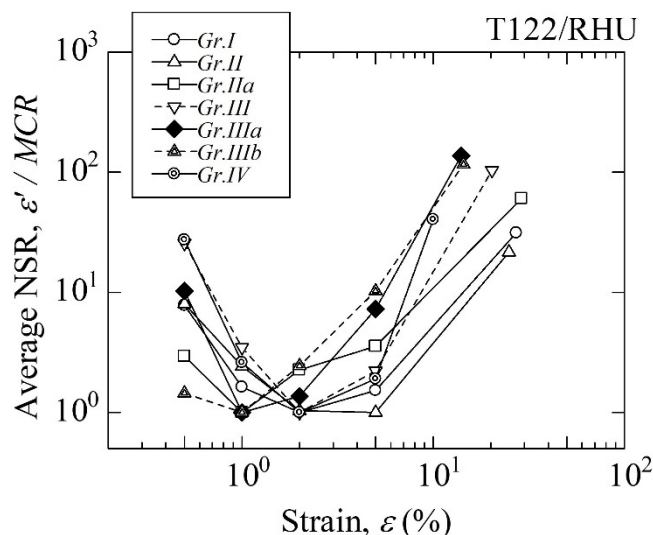


Figure 2. Average normalized creep rate (NCR) vs. strain relationship for T122/RHU

Table 2. Average test temperature T ($^{\circ}C$), stress σ (MPa), time to strain t_ε ($\varepsilon = 0.5, 1, 2,$ and 5%), time to rupture t_r , MCR, start time for Laves phase formation (TLF), and start time for Z-phase formation (TZF) for each data group of T122/RHU. Strains corresponding to each MCR and time are shown in % in each parenthesis.

| | $T/^{\circ}C$ | σ | 0.5 | 1 | 2 | 5 | t_r | MCR/ $\%h^{-1}$ | TLF/h | TZF/h |
|----------------|---------------|----------|--------|--------|--------|--------|--------|--------------------|-------------|-------------|
| <i>Gr.I</i> | 567 | 243.3 | 19.2 | 152 | 554 | 1318 | 1507 | 7.00E-3 (2, 2) | 3112 (-) | 6100 (-) |
| <i>Gr.II</i> | 634 | 142.5 | 16.9 | 127 | 697 | 1456 | 1605 | 6.66E-3 (2-5, 2) | 1865 (-) | 880 (2.9) |
| <i>Gr.IIIa</i> | 725 | 51.7 | 71.4 | 222 | 553 | 1035 | 1254 | 1.75E-2 (1-2, 1) | 14 863 (-) | >10000 (-) |
| <i>Gr.III</i> | 572 | 185.6 | 288 | 4214 | 12 644 | 22 800 | 23 782 | 1.23E-4 (1-5, 2) | 3587 (1) | 5100 (1.2) |
| <i>Gr.IIIa</i> | 600 | 126.0 | 927 | 11 202 | 25 430 | 32 230 | 33 125 | 5.14E-5 (1-2, 1) | 2479 (0.7) | 1800 (0.6) |
| <i>Gr.IIIb</i> | 625 | 68.6 | 16 833 | 36 686 | 52 200 | 63 757 | 67 090 | 1.91E-5 (0.5-1, 1) | 1920 (<0.5) | 1000 (<0.5) |
| <i>Gr.IV</i> | 673 | 60.8 | 1060 | 4350 | 9729 | 14 589 | 15 134 | 4.67E-4 (1-2, 2) | 1975 (0.7) | 1220 (0.5) |

The strains corresponding to each time point are shown as % in parentheses, which were estimated from the average creep curve for each group. The data groups where strains for TLF and/or TZF are not shown, for example, *Gr.I* indicate that the Laves phase and/or Z-phase do not formed within the average t_r for these data group. Two strains for the MCR are shown for each group; the former indicates a strain or strain range corresponding to the minimum creep rate (mcr) of an individual creep curve that constitutes the same data group, and the latter indicates the average strain corresponding to the MCR of the average creep curve for each group. The minimum creep rate for individual test conditions is designated as “mcr”, which is distinguished from the MCR of the average minimum creep rate for each data group. Therefore, the strain rates near each MCR shown in Figure 2 should be interpreted to be corresponding to a mixed state composed of transient and accelerating creep in an individual creep curve.

The $\sigma - t_\epsilon$ ($\epsilon = 0.5, 1, 2,$ and 5%) relationships for T122/RHU (NIMS, 2020) can be obtained according to the grouping, same as that for the time to rupture. Figure 3 shows the $\sigma - t_1$ relationship as a typical example. Figures 1 and 3 indicate clear hardening in the t_1 strength of *Gr.II* because the slope $\Delta\sigma/\Delta\log t_1$ decreases as compared with that for *Gr.I*; however, the corresponding slope in the $\sigma - t_r$ relationship shown in Figure 1 or the hardening in *Gr.II* is not clear. The hardening in the t_1 strength of *Gr.II* is considered to be caused by the precipitation of the Laves phase (Tamura & Abe, 2021b; Tamura, 2022).

It can also be confirmed from Figure 3 that the degradation in creep strength for *Gr.IIIa* starts from $\epsilon = 1\%$, because the slopes of the regression lines for $\epsilon = 1\%$ of *Gr.IIIa* is slightly steeper than those for *Gr.III*, and in addition, some data at lower stresses are below the regression lines for *Gr.IIIa*.

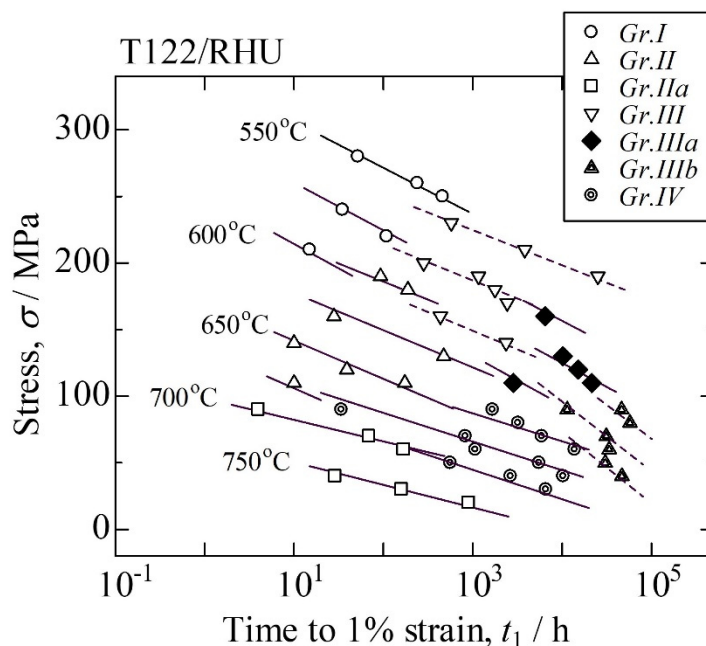


Figure 3. Stress vs. time to 1% strain relationship for T122/RHU and regression lines for each data group

4.2 Variations of QVC with Strain for T122/RHU

Figure 4 shows the variations of QVC as functions of strain for each group. Strains in the MCR are marked by solid symbols for each group (the same for all similar figures). The starting strains for Z-phase formation are indicated in the figure for each data group, where applicable. On the right side of each figure, the guidelines for the metallurgical reactions corresponding to the increase and decrease of each variable (QVC) are indicated (the same for similar figures, hereafter).

Although the QVC begin to increase with an increase in strain at an early stage of transient creep for *Gr. II* and *III*, the QVC s for the other data groups, excluding *Gr.I*, decrease with increasing strain for the entire creep duration. The values of Q at rupture for *Gr. I, II, IIIa*, and *III* are larger than 500 kJmol^{-1} and those for *Gr. IIIa, IIIb*, and *IV* are significantly small. Although the rupture strengths for *Gr. I, II*, and *IIIa* depend on the initial microstructure or hardening that occurs at an early stage of creep, the recovery and resultant degradation controls the rupture strengths for *Gr. IIIa, IIIb*, and *IV*. The values of Q for *Gr. IIIa, IIIb*, and *IV* at rupture are approximately 400 kJmol^{-1} and are slightly larger than the activation energy for the self-diffusion of α -iron (Oikawa, 1982). Moreover, the values of C at rupture for *Gr. IIIa* and *IV* are ~ 20 , which are the same values confirmed in many heat-resistant steels that are fully tempered or annealed (Tamura et al., 1999; Tamura et al., 2013). The value of C at rupture for *Gr. IIIb* is extremely small, which is explained in Section 5.8. The QVC for *Gr. IIIa* decreases simultaneously and largely with an increase in strain up to 2%. Therefore, HRHD takes place progressively during this time. Furthermore, the V for *Gr. IIIa* maintains the low values ($\sim 200 \text{ cm}^3 \text{ mol}^{-1}$) during accelerating creep; therefore, HRHD occurs continuously during accelerating creep and an unexpected drop in rupture strength is experienced in *Gr. IIIa*. In contrast, a full recovery inside the subgrains may take place in *Gr. IIIa* because the V of *Gr. IIIa* is considerably large: $V \sim 2000 \text{ cm}^3 \text{ mol}^{-1}$.

4.2.1 *Gr.I*

As shown in Table 2, both the Laves and Z-phases are not estimated to form under the average test conditions for *Gr.I*. Reflecting this estimation, the changes in *QVC* during creep shown in Figure 4 are not as large: $Q \sim 800 \text{ kJmol}^{-1}$, $V \sim 500 \text{ cm}^3 \text{ mol}^{-1}$, and $C \sim 40$. Therefore, the microstructure recovered at a slow pace during creep and maintained the martensite lath structure with M_{23}C_6 and fine MX particles. However, minor SBSD may take place during creep of $\varepsilon < 5\%$, because both Q and V increase slightly.

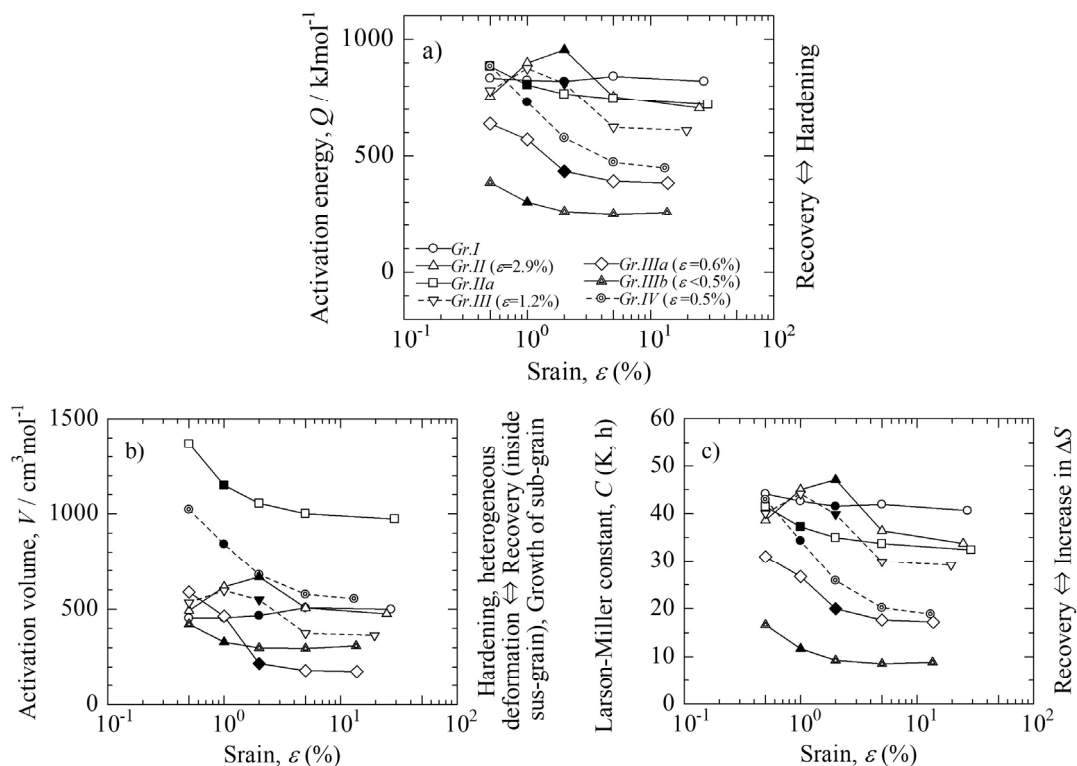


Figure 4. Results of the *QVC* analysis are shown as functions of creep strain for each group of T122/RHU steel; a) activation energy, b) activation volume, and c) Larson–Miller constant. Solid symbols indicate MCR points (the same for all similar figures), and strains in parentheses indicate the start strain for the Z-phase formation of each data group

4.2.2 *Gr.II*

The Laves phase is not formed under the average test conditions for *Gr.II* as listed in Table 2. However, this phase should be formed at an early stage of transient creep ($\varepsilon < 0.5\%$) for the following reasons: (i) The slope $\Delta\sigma/\Delta\log t_1$ at 600°C of *Gr.II* in Figure 3 at 600°C is smaller than that of *Gr.I*; therefore, *Gr.II* is a hardening region similar to the cases of Grades 91 and 92 (Tamura & Abe, 2021b; Tamura, 2022). (ii) The values of Q for *Gr.II* of RHU at $\varepsilon = 0.5, 1, \text{ and } 2\%$ strains are considerably large, $Q_{0.5,1,2} = 756, 899, \text{ and } 956 \text{ kJmol}^{-1}$, respectively. These values are slightly smaller than those of *Gr.II* for Grade 92; however, they are comparable to those for Grade 91, where the *Gr.II*s for these steels are hardened by the precipitation of the Laves phase (Tamura & Abe, 2021b; Tamura, 2022). Therefore, the observed phenomenon in *Gr.II* for RHU is estimated to indicate that the precipitation of the Laves phase is promoted by the gliding motion of dislocations during creep, as in the cases of Grades 91 and 92. However, during accelerating creep, the *QVC* decreases simultaneously with increasing strain, as shown in Figure 4. These decreases in *QVC* are also observed in *Gr.II* for each Grade 92 steel (Tamura & Abe, 2021b). However, a decrease in Q at rupture from the maximum Q (Q_{max} , hereinafter) for T122/RHU is larger than that for T92/MJT; that is, the differences of $\Delta Q = Q_{\text{max}} - Q_{\text{tr}}$ are $955.5 - 705.1 = 250.4 \text{ kJmol}^{-1}$ for T122/RHU and $1077.8 - 899.7 = 178.1 \text{ kJmol}^{-1}$ for T92/MJT. In other words, the recovery in the RHU proceeds faster than that in MJT. When $\varepsilon \geq 2.9\%$, the Z-phase is also formed, as shown in Table 2. However,

hardening in *Gr.II* is confirmed even at the rupture of MJT, although the formation of the Z-phase also occurs in accelerating creep for *Gr.II* of MJT (Tamura & Abe, 2021b). Therefore, the Laves phase particles formed in T122/RHU are thought to be easily coarsened as compared to MJT; thus the Laves hardening in *Gr.II* of RHU seems to be weakened at rupture as shown in Figure 1, owing to the overlapping of the softening by the Z-phase formation over the Laves phase hardening.

To account for these estimations, the relationship between the changes in Q_s , V_s , and C_s with increasing strain, and the changes in the corresponding strain rate, were analyzed. Table 3 shows the differences in the $[Q_s]$, $[V_s]$, C_s , and $\log\dot{\epsilon}_\epsilon$ in Equation 5 between two adjacent strains, $\Delta[Q_s]$, $\Delta[V_s]$, ΔC_s , and $\Delta\log\dot{\epsilon}_\epsilon$ at an average temperature and stress for *Gr.II* of T122/RHU steel (hereinafter termed the $\Delta[QVC]_s$ analysis method). Negative values for $\Delta[Q_s]$ are listed in Table 3 to set the summation of the above three parameters in each column equal to $\Delta\log\dot{\epsilon}_\epsilon$ and the determinant terms for the strain rate are indicated in bold-italics (this documentation is the same for other similar Tables, and hereinafter omitted).

Table 3 indicates that the changes in $\Delta\log\dot{\epsilon}_\epsilon$ can be explained by the changes in $\Delta[Q_s]$, i.e., the magnitude of resistance to the mobile dislocations, through the entire creep strain range. Namely, it is validated by Table 3 that the precipitation of the Laves phase increases $\Delta[Q_s]$ which decreases creep rate up to an MRC stage ($\epsilon \leq 2\%$). However, $\Delta[Q_s]$ largely decreases mainly because of the coarsening of the Laves phase particles precipitated, with a secondary reason being the formation of the Z-phase, which consumes the finely dispersed strengthening factor of MX particles. This increases the creep rate in an accelerating stage; that is, especially $\epsilon = 2 - 5\%$.

Table 3. Changes in Q_s , V_s , C_s , and $\log\dot{\epsilon}_\epsilon$ for two adjacent strains of *Gr.II* for T122/RHU steel

| Strain range | [0.5–1%] | [1–2%] | [2–5%] | [5%– t_r] |
|--|----------------------|---------------------|---------------------|---------------------|
| $-\Delta[Q_s]$ | <i>-11.07</i> | <i>-2.59</i> | <i>20.67</i> | <i>10.02</i> |
| $\Delta[V_s]$ | 1.42 | 0.35 | -2.41 | -0.75 |
| ΔC_s | 9.08 | 1.84 | -18.11 | -7.83 |
| $\Delta\log(\dot{\epsilon}, \%h^{-1})$ | -0.575 | -0.397 | 0.152 | 1.437 |

4.2.3 *Gr.IIa*

According to Table 2, both the Laves and Z-phases are not formed under the average test conditions for *Gr.IIa*. High values of QVC are observed throughout the creep duration shown in Figure 4. Therefore, after SBSB at an early stage of transient creep, the solid-solution hardening mainly caused by W and Mo should continue throughout the entire duration of creep, in addition to the DFRP process by $M_{23}C_6$. The QVC decreases simultaneously in transient creep, as shown in Figure 4; therefore, HRHD should occur. However, high values of V ($V \geq 1000 \text{ cm}^3 \text{ mol}^{-1}$) suggests that subgrains grow larger, and the decomposition of MX particles is less severe.

4.2.4 *Gr.III*

The QVC of *Gr.III* increase up to 1% strain with an increase in strain, which are caused by SBSB, DFRP of $M_{23}C_6$, and the strain-promoted precipitation of the Laves phase similar to the case for *Gr.II*. The QVC simultaneously decreases for $\epsilon = 1 - 5\%$, after which it remains approximately constant until rupture. In this strain range, the precipitation of both the Laves and Z-phases are confirmed (Table 2). Therefore, the simultaneous decreases in QVC during $\epsilon = 1 - 5\%$ indicate the occurrence of HRHD. An HRHD zone occasionally forms near the coarse particles of the Laves phase and/or the Z-phase grown near the PAGBs. The stress and strain concentrations generated around coarse particles promotes recovery. Therefore, the Laves phase particles grow larger and the formation of the Z-phase consumes the strengthening particles of MX in an HRHD zone, which decrease the QVC (Tamura & Abe, 2021a; 2021b). The QVC at rupture for *Gr.III* are smaller than those for *Gr.II*. Therefore, the occurrence of HRHD is more significant for *Gr.III* as compared to *Gr.II*. Thus, the t_r s for *Gr.III* are shorter than the estimated rupture lives from *Gr.II* as observed in Figure 1.

4.2.5 *Gr.IIIa*

The breakdown in the rupture strength in *Gr.IIIa* is the most significant, and the degradation in strength begins at approximately 1% strain (Figure 3). Both the Laves and Z-phases are formed from an early stage of transient creep ($\epsilon \geq 0.6\%$) as shown in Table 2. The QVC decrease with increasing strain up to 2% strain (an MCR point) and decrease slowly in accelerating creep up to rupture, as seen in Figure 4. The HRHD is significant during transient

creep because of the simultaneous and large decreases in QVC , and the severe HRHD continues in accelerating creep because the values of V are the lowest throughout the entire strain range in all groups.

The decreases in QVC between $\varepsilon = 1 - 2\%$ are much more significant than those for $\varepsilon = 0.5 - 1\%$. To investigate these results, the $\Delta[QVC]_s$ analysis at an average temperature and stress for *Gr.IIIa* were performed in the same manner as that shown in Table 3, and the results are shown in Table 4.

For a transient creep of $\varepsilon \leq 1\%$, the decrease in $\Delta[V_s] + \Delta C_s$ is the determinant term, even though $\Delta[Q_s]$ decreases because of the coarsening of precipitates and the formation of the Z-phase. Here, the decrease in $\Delta[V_s]$, i.e., the occurrence of HRHD, is necessary to maintain transient creep; however, the experimental evidence for the existence of HRHD has not yet been obtained. For $\varepsilon \geq 1\%$, the decreases in $\Delta[Q_s]$, i.e., the progress in recovery, are the determinant terms for increasing creep rate with an increase in strain. For $\varepsilon = 1 - 2\%$, $\Delta[V_s]$ still decreases; therefore, the HRHD is still active. In an accelerating creep for $\varepsilon \geq 2\%$, significant recovery occurs because $\Delta[V_s]$ increases and both $\Delta[Q_s]$ and ΔC_s decrease. However, the values of V remains the lowest throughout the entire strain range in all the data groups (Figure 4). Therefore, the severe HRHD continues and the decomposition of microstructure, i.e., the formation of the Z-phase consuming the strengthening particles of MX, is significant inside the HRHD zone, which leads to the unexpected large drops in rupture strength in *Gr.IIIa*. The detailed mechanisms for the degradation are discussed in Sections 5.5–5.7.

Table 4. Changes in Q_s , V_s , C_s , and $\log \dot{\varepsilon}_\varepsilon$ between two adjacent strains for *Gr.IIIa* of T122/RHU steel

| Strain range | [0.5–1%] | [1–2%] | [2–5%] | [5%– t_r] |
|--|--------------|--------------|-------------|--------------|
| $-\Delta[Q_s]$ | 4.46 | 16.08 | 3.16 | 1.39 |
| $\Delta[V_s]$ | -0.95 | -3.13 | 0.06 | 0.68 |
| ΔC_s | -4.50 | -12.79 | -2.46 | -0.76 |
| $\Delta \log(\dot{\varepsilon}, \%h^{-1})$ | -1.00 | 0.16 | 0.79 | 1.31 |

4.2.6 *Gr.IIIb*

In Figure 1, *Gr.IIIb* is clearly different from *Gr.IIIa*, where the slope $\Delta\sigma/\Delta \log t_r$ is smaller than that for *Gr.IIIa*, or the rate of degradation in rupture strength for *Gr.IIIb* is mitigated as compared with that for *Gr.IIIa*. In *Gr.IIIb*, both the Laves and Z-phases are formed within a smaller strain $\varepsilon < 0.5\%$ than that in *Gr.IIIa*. Therefore, the average NCR at $\varepsilon = 0.5\%$ shown in Figure 2 is the lowest; that is, the hardening proceeds fast and resultantly the recovery rate or the increase in the average NCR in accelerating creep, is highest in all data groups. Reflecting these circumstances, the values of Q and C are considerably small throughout the entire creep life duration; however, the V is larger than those for *Gr.IIIa*, as seen in Figure 4. This indicates that the HRHD is not as severe in *Gr.IIIb* although the recovery progresses significantly through processes such as the new generation of subgrains. This is discussed in detail in Section 5.8.

4.2.7 *Gr.IV*

Gr.IV is an intermediate region between *Gr.IIIa* and *IIIb*. Both the Laves and Z-phases are formed within a smaller strain of approximately $\varepsilon = 0.5\%$. The values of QVC are smaller than those for *Gr.IIIa*, but larger than those for *Gr.IIIb*. Therefore, the HRHD in *Gr.IV* was not as severe as those for *Gr.IIIa* and *IIIb*.

4.3 Creep Behavior of Grade 122 Steels (RHQ, RhA, and RHT) Other than RHU

4.3.1 $\sigma - t_r$ Relationship

The $\sigma - t_r$ relationships for P122/RHQ, p1-122/RhA (NIMS, 2020), and DTB122/RHT (NIMS, 2021) are shown in Figures A1–A3 in Appendix, respectively. The data for each steel were classified into seven groups: *Gr.I–IV*. In the classification, the $\sigma - t_r$ and t_ε relationships for T122/RHU (Figures 1 and 3) and Grades 91 and 92 (Tamura & Abe, 2021b; Tamura, 2022) were referred to.

The Laves phase hardening in the rupture strength in each *Gr.II* of RhA and RHT is clearly confirmed, similar to the cases for Grades 91 and 92 (Tamura & Abe, 2021b; Tamura, 2022); as shown in Figures A2 and A3, the slopes of regression lines for *Gr.II* of RhA and RHT are smaller than those for *Gr.I*, respectively, although the Laves hardening for *Gr.II* of RHQ (Figure A1) is not as clear as the case of RHU (Figure 1).

The largest and unexpected drops in rupture strength are observed in each *Gr.IIIa* of Grade 122 investigated as shown in Figure 1, and Figures A1–A3. Each unexpected drop in rupture strength of Grade 122 begins relatively

early, from approximately 15 000 h at 600 °C, as compared to those for Grade 92/MJP and MJT steels (Tamura & Abe, 2021b). Reflecting the early starts of *Gr.IIIa* in Grade 122 the unexpected drops in strength for each steel finishes long before 100 000 h and then each *Gr.IIIb* starts, respectively, where the degradation rates ($\Delta\sigma/\Delta\log t_r$) are mitigated.

4.3.2 Comparison of the $\sigma - t_r$ Relationships Among Grade 122

Figure 5 shows a comparison of the $\sigma - t_r$ relationships among Grade 122 at 600 °C. Regression lines for *Gr.s.I, II, III, IIIa*, and *IIIb* are drawn only for the RHU by the solid and dashed lines, as indicated in Figure 5. The rupture strengths for *Gr.s.I* and *II* of RHU and RHQ are higher than those of RhA and RHT, and the degradation rates of the rupture strength for *Gr.s.IIIb* of Grade 122 seem to be mitigated, although the rupture strengths for *Gr.s.IIIa* of all heats of Grade 122 dropped significantly. The differences in the rupture strength of each heat in *Gr.IIIa* seem to be smaller than those in *Gr.s.I* and *II*. However, there were inter-heat-differences among the rupture strengths of Grade 122 for 1E5 h. These differences and their related root causes are discussed in Sections 5.6–5.9.

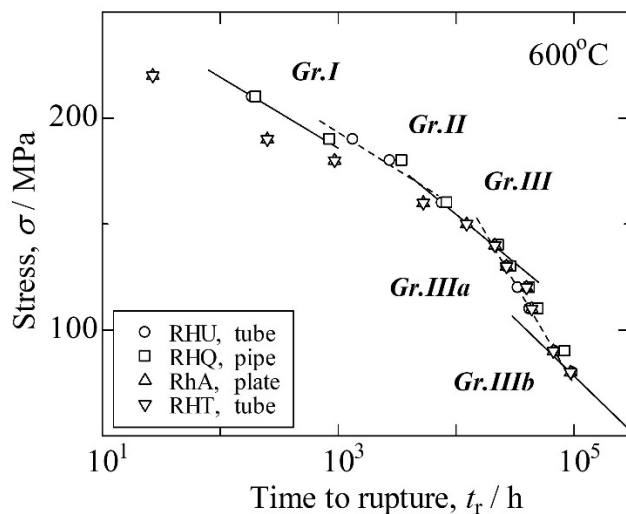


Figure 5. $\sigma - t_r$ relationships for Grade 122 at 600 °C and the regression lines are only for RHU

4.3.3 $\varepsilon - QVC$ Relationship

Figures A4–A10 show the relationships between strain and *QVC* for *Gr.I–Gr.IV* of RHQ, RhA, and RHT, respectively, compared to those for RHU. The $\varepsilon - QVC$ behaviors of Grade 122 are similar with each other for all data groups. Namely, the *QVC* for each *Gr.I* increase with increasing strain at an early stage of creep, after which it remains approximately constant. The *QVC* for each *Gr.s. II* and *III* decrease with increasing strain after an initial increase. The initial values at $\varepsilon = 0.5\%$ of the *QVC* for the other four data groups, *Gr.s.IIIa, IIIa, IIIb*, and *IV*, were already relatively high and subsequently decreased up to rupture.

The hardening processes of SBSBD by the swept-out dislocations from subgrains and the DFRP mechanism operating on $M_{23}C_6$ particles continue throughout the entire strain range of each *Gr.I* of all steels investigated, and the Laves phase precipitation hardening is possibly superimposed on the SBSBD and DFRP at a later stage of creep.

In *Gr.s.II* and *III*, the hardening processes of the SBSBD, DFRP, and Laves phase precipitation start at an initial stage of creep and continue up to approximately 1% strain. Thereafter, recovery become superior to the hardening and, the *QVC* begin to decrease simultaneously, in which case HRHD should occur. In the later stage of creep for *Gr.s.II* of RHU and RHQ, the formation of the Z-phase consuming the strengthening particles of MX is estimated to become active and mask the Laves phase hardening. Therefore, the Laves phase hardenings in *Gr.II* for the rupture strength of RHU and RHQ are unclear as compared with those for RhA and RHT (Figures 1 and A1–A3). However, the occurrence of the Z-phase formation cannot be disputed in RhA and RHT, because the considerable decreases in *V* during accelerating creep of RhA and RHT are confirmed, as shown in Figure A5. Therefore, it is difficult to conclude which one is a major masking factor against the hardening in *Gr.II*; the coarsening of the Laves phase particles or the Z-phase formation consuming finely dispersed MX particles. This problem is further discussed in Section 5.7 relating to the degradation of the rupture strength in *Gr.IIIa*.

In *Gr.IIIa* for Grade 122, the Laves phase is not estimated to be formed according to Table 2. Therefore, the drag mechanism for W and Mo by dislocations (Hayakawa, Terada, Yoshida, Nakashima, & Goto, 2003a; Hayakawa, Terada, Yoshida, Nakashima, & Goto, 2003b; Hayakawa et al., 2007) should operate in addition to the SBSB and DFRP mechanism. Furthermore, HRHD should occur, because the *QVC*s decrease gradually throughout the entire creep range. However, the values of *V* for *Gr.122* are considerably high, larger than approximately $1000 \text{ cm}^3 \text{ mol}^{-1}$. Therefore, in these cases, subgrains are newly formed and the stress and strain concentrations inside the subgrains are relaxed. Therefore, the harmful effect of HRHD is not significant.

The values of *Q* at $\varepsilon = 0.5\%$ for *Grs.IIIa*, *IIIb*, and *IV* of all steels investigated are considerably high; therefore, the Laves phase hardening, in addition to the SBSB and DFRP mechanism, should be completed before reaching 0.5% strain.

Concerning *Gr.IIIa*, the *QVC* of Grade 122 decrease rapidly up to approximately $\varepsilon = 2\%$, after which they remain approximately constant up to rupture. When the *V* decreases with increasing strain, or the value of *V* is small, significant HRHD should occur. The microstructural degradation, such as the formation of the Z-phase consuming the strengthening particles of MX inside an HRHD zone and the coarsening of precipitated particles near the boundaries of an HRHD zone, proceeds significantly. Therefore, the values of *Q* and *C* becomes small. That is, the recovery proceeds up to 2% strain even in transient creep, as explained in Table 4, and the deformation is concentrated in a locally recovered zone: HRHD. When $\varepsilon > 2\%$, the values of *V* are small ($\sim 200 \text{ cm}^3 \text{ mol}^{-1}$) and subsequently remain approximately constant. Therefore, HRHD occurs throughout the entire strain range of *Gr.IIIa*.

Similar HRHD occurs throughout the entire strain range of *Grs.IIIb* and *IV* for Grade 122 and in a strain range of $\varepsilon = 1 - 5\%$ of *Grs.II* and *III*; however, the values of *V* for each are relatively large. Therefore, the drop in strength owing to the harmful effect of HRHD are not as large.

Concerning *Gr.IIIb* for Grade 122, the degradation rates ($\Delta\sigma/\Delta\log t_r$) become slower than those of *Gr.IIIa* (Figures 1 and A1–A3). Although the values of *Q* and *C* for each steel are smaller than those of *Gr.IIIa* throughout the entire strain range of creep (Figures 4, A8, and A9), the values of *V* in accelerating creep of *Gr.IIIb* for each steel are larger than those of *Gr.IIIa*. Therefore, the harmful effect of HRHD at rupture in *Gr.IIIb* is mitigated compared to that of *Gr.IIIa*. Therefore, the rupture lives in *Gr.IIIb* for all steels of Grade 122 become longer than those estimated in *Gr.IIIa*.

4.3.4 Variations of *QVC*

The values of *QVC* for Grade 122 tend to decrease with increasing strain until rupture, as seen in Figures A4–A10, except for Figure A4 for *Gr.I* and initial states of *Grs.II* and *III*. However, there are large differences at specific strains in *QVC* among each data group. The maximum differences at $\varepsilon = 0.5\%$ in each *QVC* among all data groups seem to be larger than those at rupture. For example, the difference in *Q* at $\varepsilon = 0.5\%$ for *Gr.II* reaches $Q \sim 500 \text{ kJmol}^{-1}$ and in contrast, $\Delta Q < 200 \text{ kJmol}^{-1}$ at rupture. However, even if a value of one of the *QVC* is the highest at 0.5% strain, the high ranking does not always hold throughout the entire creep duration, as seen in Figures A4–A10. These facts indicate that the variations of *QVC* during creep, including rupture, should be interpreted adequately based on metallurgical knowledge, because t_ε or t_r is strictly calculated only from *QVC* with temperature and stress conditions according to Equation 1 without using any adjustable parameters.

The values of *QVC* for *Grs.I* of RHU and RHQ are approximately higher than those of RhA and RHT throughout the entire creep duration (Figure A4). The *QVC* values at $\varepsilon = 0.5\%$ for each steel are strongly affected by each initial microstructure because the average test temperatures of each *Gr.I* are relatively low and the creep strain of 0.5% is small. These values of *QVC* for Grade 122 are discussed in detail Section 5.2, which combines the related data of Grades 91 and 92.

The *QVC* for *Gr.II* of Grade 122 increase with increasing strain, peak during transient creep, and subsequently decrease monotonically until rupture, as shown in Figure A5. Among these *QVC*s of Grade 122, the values of *QVC* for *Gr.II* of RHT are the highest up to $\varepsilon = 2\%$ (Figure A5). This is because the Laves phase easily precipitates inside δ -ferrite with enriched Mo and W, which causes hardening and a resultant increase in the *Q*. On the other hand, the ranking of each value of *QVC* for a specific data group of each steel in Grade 122 changes complicatedly with increasing strain, independent of the existence of δ -ferrite (Figures A4–A10). The reasons for these changes are as follows. First, the degree of recovery in each steel depends on a progressing speed of each recovery reaction and second, each reaction interacts with each other.

Concerning the maximum difference in each *QVC* for a specific strain, it is observed that the differences in each *QVC* for *Gr.IIIa* are minimum among the data groups irrelevant to creep strain, where the unexpected drops in

long-term rupture strength are experienced (Figures A4–A10). In this group, the QVC largely decreased up to $\varepsilon \sim 2\%$ and subsequently maintain each low level up to rupture in all steels investigated. Therefore, HRHD should occur throughout the entire creep duration. In addition, the maximum differences in each QVC for *Gr.IIIa* are particularly small as compared to those of the other data groups. This denotes that the microstructure of Grade 122 in the test conditions of *Gr.IIIa* mainly depends on only nominal creep strain as opposed to the initial microstructure or situation of each steel. In other words, the microstructures inside the HRHD zone at a given nominal strain, which determines the nominal creep rate of each steel, are roughly similar with each other. That is, the number density of MX inside the HRHD zone (ρ_{MXi}) is estimated to decrease similarly with increasing nominal strain, as pointed out by Sawada, Kushima, Tabuchi, and Kimura (2011). When the finely dispersed MX particles inside the HRHD zone is almost consumed, the creep mode of *Gr.IIIa* ought to finish locally. Therefore, the number of such HRHD zone without finely dispersed MX particles should increase or the area of such an HRHD zone should be enlarged during the deformation of *Gr.IIIa*. In other words, in *Gr.IIIa*, creep is progressing heterogeneously, and the average creep rate in heterogeneously deformed areas controls the nominal strain rate of the specimen. Finally, macroscopically, the creep mode of *Gr.IIIa* finishes when the heterogeneously deformed areas cover the entire specimen, and then, a creep mode of *Gr.IIIb* initiates, where the degradation rate is mitigated. This is further discussed in Section 5.8.

However, clear differences in rupture strength for *Gr.IIIa* still exist among four steels of Grade 122 as shown in Figure 5. These differences can be explained by the existing small differences in QVC , which is discussed in Section 5.7 (Figures 30 and 31).

The maximum difference in each QVC for *Gr.IIIb* appears to become greater than those for *Gr.IIIa* (Figures A8 and A9). The values of V at rupture for RHU and RhA are larger than those for RHQ and RHT. The higher values of V possibly mitigate the harmful effects of HRHD; therefore, the prolongation of rupture lives is expected under the test conditions of *Gr.IIIb*, which are near the service conditions of actual power plants.

The rupture lives (strengths) of material are not determined by the values of QVC themselves, but by the deduction of $[Q]$, $[V]$, and C according to Equation 2. If we assume $\log t > 1$, $\log t$ becomes small when Q is small because $[Q]$, $[V]$, and C are positive. Therefore, the initial values of Q are designed to be high and the values of Q are expected to be high as long as possible. Therefore, the development of new high-strength martensitic steels is performed along this line (Sawada & Kimura, 2019). The relationships between rupture strength and the values of QVC are discussed in detail in Sections 5.6 and 5.8.

4.3.5 $\Delta[QVC]_s$ Analysis for *Gr.IIIa*

The $\Delta[QVC]_s$ analysis with increasing strain at an average temperature and stress for each *Gr.IIIa* of Grade 122 other than RHU were also performed in the same manner leading to the results in Table 4, although these results are omitted for simplicity. In a transient creep of $\varepsilon \leq 1\%$, the decrease in $\Delta[V_s] + \Delta C_s$ is the determinant term, even though $\Delta[Q_s]$ decreases owing to the coarsening of precipitates and formation of the Z-phase. Here, the decrease in $\Delta[V_s]$, i.e., the occurrence of HRHD, is absolutely necessary to maintain transient creep although the microstructural evidence for the existence of HRHD has not yet been obtained. For $\varepsilon \geq 1\%$, the decreases in $\Delta[Q_s]$ or the increase in $\Delta[V_s] + \Delta C_s$, i.e., the progress in recovery, are the determinant term(s) for increasing creep rate with an increase in strain. For $\varepsilon \geq 2\%$, significant recovery starts because $\Delta[V_s]$ increases and both $\Delta[Q_s]$ and ΔC_s decrease. However, the values of V remain the lowest throughout the entire strain range among all the groups; therefore, the severe HRHD continues and the decomposition of microstructure, i.e., the formation of the Z-phase responsible for consuming the strengthening particles of MX, occurs significantly.

5. Discussion

5.1 Beginning of HRHD

5.1.1 Transmission Electron Microscopy (TEM) Observations

Kushima, Kimura, and Abe (2002) investigated the TEM of ruptured specimens of T91/MGC tested at 600 °C in detail, and the following results were obtained:

[i] 160 MPa (871.2 h): A slightly recovered microstructure with increases in lath width and subgrain size and a decrease in dislocation density was observed as compared to tempered martensite prior to the test. The test conditions for 160 MPa correspond to *Gr.II* in the $\sigma - t_r$ relationship of T91/MGC (Tamura & Abe, 2021b).

[ii] 120 MPa (12 858.6 h): Significant progress was observed in the recovery of the tempered martensite microstructure and annihilation of the martensite lath structure. The test conditions for 120 MPa correspond to *Gr.III* in the $\sigma - t_r$ relationship of T91/MGC (Tamura & Abe, 2021b).

[iii] 100 MPa (34 141 h): Significantly recovered regions were observed along the PAGBs; however, the microstructure inside the grains is still finer than that along the PAGBs. Heterogeneous progress in the recovery of the tempered martensite microstructure was observed under this stress, in contrast to the homogeneous process at higher stresses (Kushima et al., 1999; 2002). The test conditions for 100 MPa correspond to *Gr.IIIa* in the $\sigma - t_r$ relationship of T91/MGC (Tamura & Abe, 2021b).

Kimura, Sawada, Kubo, and Kushima (2004), Sawada et al. (2011), and Kimura, Sawada, Kushima, and Toda (2012b) investigated TEM of the creep interrupted specimens of T91/MGC tested at 600 °C in detail and the following results of observation were clarified.

[i] 140 MPa (classified as *Gr.II* of T91/MGC):

- a) Crept for 263.5 h: Fine lath martensitic microstructure was observed.
- b) Crept for 1200 h: Recovered and coarsened subgrains were observed along the PAGBs and/or packet boundaries. The creep is interrupted at the mcr stage.
- c) Crept for 3000 h: Extension of the recovered region consisting of coarsened subgrains with a low dislocation density was observed. Therefore, HRHD may occur; however, the harmful effect on the strength of HRHD should not be significant. A significant decrease in the hardness was confirmed in this accelerating creep stage.
- d) Ruptured for 3414.7 h: The microstructure of coarsened subgrains with a low dislocation density throughout the grains was covered.

[ii] 120 MPa (classified as *Gr.III* of T91/MGC):

- a) Crept for 1200 h: The fine lath martensitic microstructure was still maintained, although recovered and coarsened subgrains were observed in the specimen crept for the same duration but under a higher stress of 140 MPa, as explained in the above case [i]-b) of 140 MPa. This crept duration corresponds to 0.4% strain in transient creep of the average creep curve of *Gr.III* and this strain is slightly smaller than each peak strain for *QVC* of *Gr.III*. The classification to a specific data group and estimation of strain are due to the previous work (Tamura & Abe, 2021b). This documentation is the same for other similar explanation in this section 5.1.1, and hereinafter omitted. The values of *QVC* at this stage were high, for example $V \sim 660 \text{ cm}^3 \text{ mol}^{-1}$ (Tamura & Abe, 2021b).
- b) Crept for 3000 h: A few coarsened subgrains with a lower dislocation density were observed in the vicinity of the PAGBs and/or packet boundaries. The creep was interrupted at the mcr stage under this creep conditions.
- c) Crept for 7900 h: Slightly coarsened subgrains were observed in the vicinity of the PAGBs and/or packet boundaries in the specimen crept and interrupted in the accelerating creep. A significant decrease in hardness was also confirmed in this accelerating creep stage.
- d) Ruptured after 12 858 h: The microstructure was completely covered by coarsened subgrains with a rather low dislocation density. The significant decrease in hardness in the final stage of the accelerating creep is caused by the spreading of such coarse subgrains throughout the entire prior austenite grain.

[iii] 70 MPa (classified as *Gr.IIIa* of T91/MGC):

- a) Crept for 3000 h: Tempered martensitic fine lath microstructure was observed in this specimen. This crept duration corresponds to 0.3% strain in transient creep of the average creep curve of *Gr.IIIa* and this strain is slightly larger than each strain for the maximum *QVC* ($\epsilon = 0.2\%$) of *Gr.IIIa* and is an early stage of the MCR point ($\epsilon = 1\%$).
- b) Crept for 9992 h: A tempered martensitic fine lath microstructure was observed in this specimen, and no obvious difference in microstructure was detected between the crept specimens of [iii]-a) and -b). This creep duration corresponds to 0.4% strain also in transient creep of the average creep curve of *Gr.IIIa* and this strain is slightly larger than each strain for the maximum *QVC* ($\epsilon = 0.2\%$) of *Gr.IIIa*.
- c) Crept for 20 000 h: Slightly coarsened subgrains were observed in the vicinity of the PAGBs and/or packet boundaries in the specimen crept and interrupted in the mcr stage under the test conditions. This crept duration corresponds to 0.75% strain also in the transient creep or a slightly earlier stage of the MCR point of the average creep curve of *Gr.IIIa*.
- d) Crept for 30 030 h: Spreading of the coarsened subgrain area from the vicinity of the PAGBs and/or packet boundaries in the specimen crept to the onset of the accelerating creep stage. That is, the progress in recovery is inhomogeneous. This creep duration corresponds to 1.2% strain or a slightly later stage of the MCR point of the average creep curve of *Gr.IIIa*.
- e) Crept for 50 064 h: Growth of subgrain size was observed in parts of the specimen.

f) Crept for 70 000 h: Equiaxed subgrains were observed over the entire area of the gauge portion.

g) Ruptured after 80 767 h: Significant coarsening of subgrain and reduction of dislocation density was observed.

Figure 6 schematically shows the above-mentioned variations of the TEM microstructure during creep at 600 °C of T91/MGC using symbolized marks in a $\sigma - t$ diagram. The symbol marks on the far right in Figure 6 correspond to the ruptures for each data group. The recovery stages are classified into four groups; little or slight change (\times), recovery along the PAGBs and/or packet boundaries (\circ), spreading recovery region into the inside each grain (\odot), and full recovery or heterogeneous recovery (solid or semi-solid), where the details are explained above. Figure 6 shows that recovery starts to occur heterogeneously near a PAGB or packet boundary at a strain of each mcr point, and the heterogeneously recovered region spreads toward the center of each prior austenite grain or packet. Furthermore, it is found that although the heterogeneous recovered region reaches the center of a grain or packet at rupture at a high stress in *Gr.III*, at a lower stress of 100 MPa in *Gr.IIIa*, rupture occurs with a recovered band structure along a PAGB of an approximate width of 1 μm , which may lead to shortening the rupture life (Kushima et al., 1999). A similar large recovered band to T91/MGC is also reported in a specimen of T92/MJT ruptured at 600 °C and 120 MPa for $t_r = 65\,363.4$ h (Sawada & Kimura, 2019), where the test conditions corresponded to *Gr.IIIa* of T92/MJT (Tamura & Abe, 2021b). Under a lower stress of 70 MPa equiaxed subgrains covered the entire area of the gauge portion of the specimen, which crept for 70 000 h. Thereafter, the subgrains coarsened significantly. Therefore, a recovered band structure along the PAGBs is not always a characteristic feature of the ruptured specimens in *Gr.IIIa*.

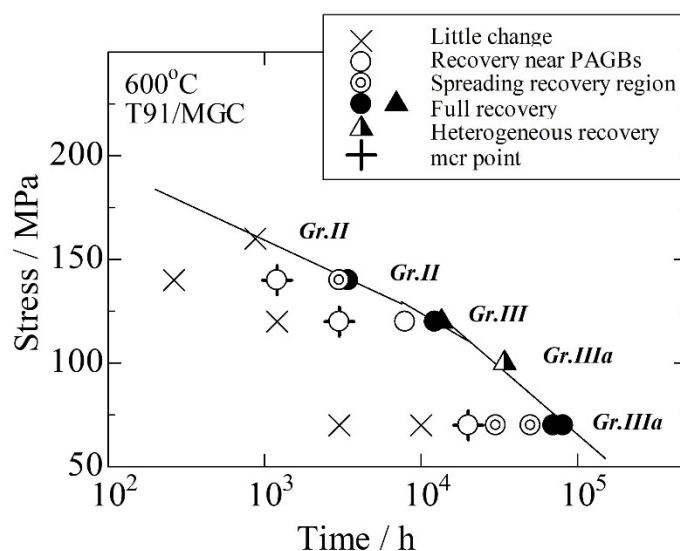


Figure 6. Schematic illustration of the results of the TEM observations in a stress vs. time diagram at 600 °C for T91/MGC. A cross mark at 160 MPa and triangles are from Kushima et al. (1999; 2002), and cross marks are at 140 MPa or less and circles are from Kimura et al. (2004; 2012b). Regression lines for t_r s for *Gr.II*, *Gr.III*, and *Gr.IIIa* of T91/MGC are drawn (Tamura & Abe, 2021b). Marks on the left side of the regression lines represent the results of the creep-interrupted specimens.

It is certainly confirmed from Figure 6 that the recovery near the PAGBs begins at each mcr point of the specified creep test. However, metallurgical investigations other than the TEM observation mentioned above are necessary, because the Z-phase begins to form for approximately 7000 h at 600 °C (Sawada et al., 2007). Therefore, distinct recovery should occur during transient creep in *Gr.IIIa* of T91/MGC under 70 MPa at 600 °C.

5.1.2 Variations of Metallurgical Parameters During Creep

Figure 7 shows the relationship between subgrain size and Vickers hardness (HV) of creep-interrupted T91/MGC. Creep conditions for T91/MGC are 600°C and 70 MPa ($t_r = 80\,737$ h). Strains for a specific creep interruption time and a range of hardness in the grip portion during creep were added in the figure. These data are read from the diagrams of $t - \dot{\epsilon}$, $t - \epsilon$, $t - HV$, and $t - d$ (Sawada et al., 2011). Similar data for X20CrMoV12-1 (DIN 17176: 0.2C-11Cr-1Mo-0.3V steel, hereinafter X20/Bazazi) are plotted using squares (Bazazi, 2009). Creep

conditions for X20/Bazazi are 550°C and 120 MPa ($t_r = 139\,971$ h). An mcr point of X20/Bazazi is marked by a solid square ($\epsilon \sim 0.76\%$ and $t \sim 34\,000$ h). An mcr point of T91/MGC is reported as 20 000 h (Kimura et al., 2004) and occurs at between $\epsilon = 0.26 - 0.5\%$ (estimated to be $\epsilon \sim 0.36\%$).

Typically, the hardness decreases and the subgrain size increases with progressing creep, whereas the hardness in the gauge portion decreases significantly with increasing creep strain as compared to that of the grip portion. Furthermore, comparing the softening behaviors of T91/MGC and X20/Bazazi in Figure 7, fine particles of MX particles in MGC retard the progress of recovery when creep is in a transient stage. However, the significant recovery advances drastically between $\epsilon = 0.5 - 0.8$ or 2.5% in accelerating creep of MGC. This is possibly due to the conversion of finely dispersed MX particles to coarse Z-phase particles near the boundaries.

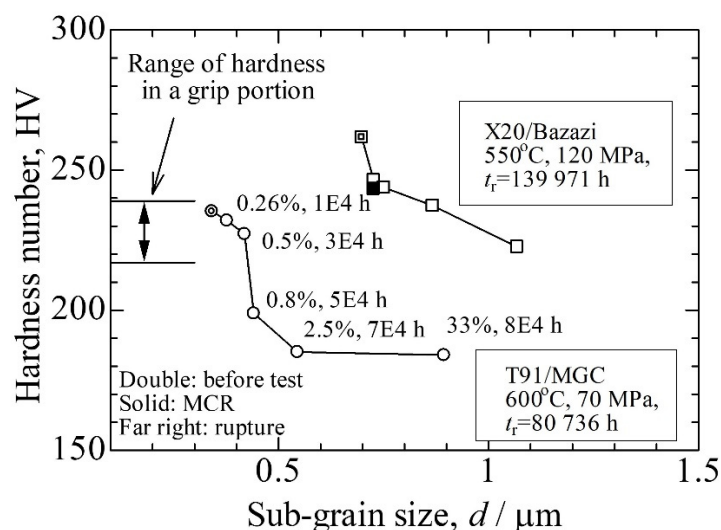


Figure 7. Relationship between subgrain size and hardness number during creep of T91/MGC and X20/Bazazi

Figure 8 shows that relationship between the dislocation density inside subgrains and subgrain size during the creep of several high-Cr martensitic steels (Straub, Meier, Ostermann, & Blum, 1993; Sawada, Maruyama, Komine, & Nagae, 1997; Taneike, Sawada, & Abe, 2003; Bazazi, 2009; Panait et al., 2010; Sawada et al., 2011; Dudova, Plotnikova, Molodov, Belyakov, & Kaibyshev, 2012; Dudko, Belyakov, Molodov, & Kaibyshev, 2013). Similar data to Bazazi's data (2009) are available in the literature (Aghajani, Somenen, & Eggeler, 2009; Pesicka, Aghajani, Somen, Hartmaier, & Eggeler, 2010). The symbol, name of the steel investigated, test conditions, time to rupture, and first author for each test are listed at the bottom of the figure. The subgrain size on the vertical axis indicates the width of the lath structure or the average subgrain size. All relationships between ρ and d are read from the diagrams of for example $t - \rho$ and $t - d$ relationships in the literature. The initial dislocation density of X20/Straub (X20 steel examined by Straub et al., 1993) is unnaturally low, however, the reason for this is unknown. Strains for specific creep-interrupted time of T91/MGC are given near each data point in Figure 8, similar to Figure 7. An mcr point of T91/MGC is reported as 20 000 h (Kimura et al., 2004) and occurs between $\epsilon = 0.26 - 0.5\%$ (estimated to be $\epsilon \sim 0.36\%$).

P91/Panait is ASME Grade P91 and was examined by Panait et al. (2010; abbreviated as P91/Panait, hereinafter). The name plate 91 in Figure 8 is given to a Type 91 steel prepared in a laboratory by Sawada et al. (1997). P92/Dudko is an abbreviated name for ASME Grade P92 and was examined by Dudko et al (2013). P92Co/Dudova is an abbreviated name for Co modified Type 92 steel prepared in a laboratory by Dudova et al. (2012). The term 0C is given to a carbon free 9Cr-3W-3Co steel strengthened by V, Nb, N, and B and was prepared in a laboratory by Taneike, Sawada, and Abe (2003). 08C is a reference steel with 0.08% carbon to a steel of 0C.

The data points at the bottom right were obtained prior to the test, and the top left of the data is at rupture for each creep test. The degree of recovery, $|\Delta \ln d / \Delta \ln \rho|$ or $|\Delta \ln \rho|$ in a transient creep range, is roughly classified by two groups excepting X20/Straub: The first group is represented by X20/Bazazi and the $|\Delta \ln d / \Delta \ln \rho|$ in transient creep is extremely small, whereas a decrease in ρ or $|\Delta \ln \rho|$ in transient creep is large. The second group is high-Cr-high-strength martensitic steels where the $|\Delta \ln d / \Delta \ln \rho|$ s are not insignificantly small, whereas the decreases in ρ or $|\Delta \ln \rho|$ s are significantly small. It is clear from Figure 8 that these groups are classified by the presence of

finely dispersed MX particles. Alternatively, finely dispersed MX particles inside subgrains trap dislocations and retard recovery. Furthermore, as shown in Figure 8, the dislocation density decreases during transient creep in all high-Cr-high-strength martensitic steel to a greater or lesser degree. This indicates that the trapping effect on dislocations by MX particles is imperfect or that finely dispersed MX particles dissolve even during transient creep.

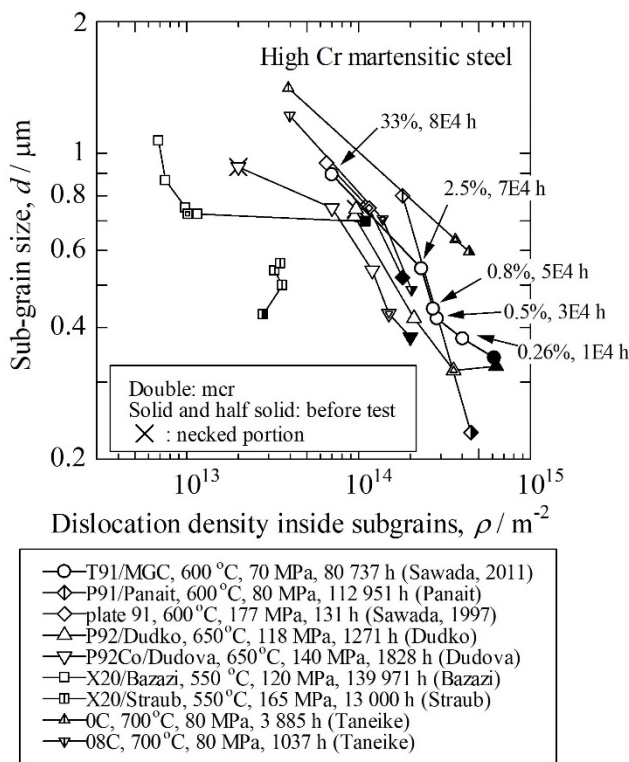


Figure 8. Relationship between dislocation density and subgrain size of high-Cr martensitic steel

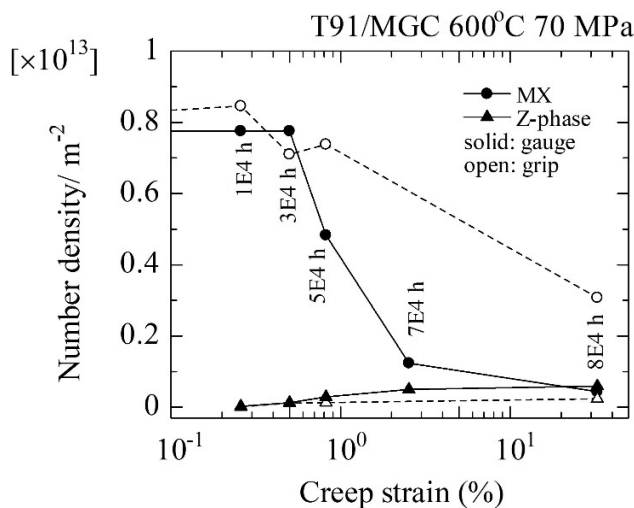


Figure 9. Number densities of MX and Z-phase particles in gauge and grip portions as functions of creep strain. The creep test of T91/MGC was performed at 600 °C and 70 MPa

Figure 9 shows the changes in number density of MX particles (ρ_{MX}) and Z-phase (ρ_Z) in gauge and grip portions of T91/MGC tested at 600 °C and 70 MPa (*Gr.IIIa*) as functions of creep strain (Sawada et al., 2011). Creep-

interrupted durations of time were provided near each data point. The mcr point occurs for 2E4 h ($\varepsilon \sim 0.36\%$). It is confirmed from Figure 9 that ρ_{MX} in a gauge portion decreases largely between 3E4 and 7E4 h. That is, in accelerating creep, which corresponds to an increase in ρ_Z . This means that the Z-phase is formed by dissolving the strengthening factor of finely dispersed MX particles. On the other hand, ρ_{MX} in a gauge portion changes little until 3E4 h, which includes transient creep. Two aspects are highlighted in Figure 9 when comparing the changes in ρ_{MX} between gauge and grip portions. First, although the ρ_{MX} of a grip portion is retained at approximately 40% of the initial value at an approximately ruptured state (8E4 h), almost all the MX particles dissolve and are converted to the Z-phase in a gauge portion. That is, the decreasing ratio in a gauge portion is approximately 94% for 8E4 h. This indicates that creep straining strongly promotes the formation of the Z-phase, consuming finely dispersed MX particles inside the subgrains. Second, the formation of the Z-phase, i.e., dissolving of MX, clearly occurs even in a transient creep stage ($t \leq 2E4$ h, including data points for 1E4 h) although the observed results may vary across the data of grip and gauge portions.

5.1.3 Existence of HRHD During Transient Creep

In Sections 5.1.1 and 5.1.2, the variations of TEM microstructure, hardness, subgrain size, dislocation density, and number densities of MX and Z-phase particles during creep for T91/MGC are explained. Figure 10 schematically illustrates these variations in metallurgical factors during the creep of T91/MGC tested at 600 °C and 70 MPa (*Gr.IIIa*). The meanings of the abbreviated terms and symbols in Figure 10 are explained in the figure caption. Drastic changes in the microstructure, including a decrease in ρ_{MX} and the consequent formation of coarse Z-phase particles, occur between 3E4–7E4 h ($\varepsilon = 0.5 - 2.5\%$) in an accelerating creep range. During these durations, the spreading of a recovered region develops from the PAGBs into the center of each prior austenite grain, and fully recovered regions are confirmed at rupture in the entire specimen range accompanying the unexpected drop in rupture strength at 600 °C and 70 MPa. In other words, no evidence of heterogeneous recovery or HRHD is obtained in the transient creep stage employing TEM observation. However, recovery signs, i.e., a decrease in hardness and ρ_{MX} , an increase in ρ_Z , and d , and a decrease in ρ are confirmed in a transient creep stage (Figures 7–9). Furthermore, microstructural changes owing to the SBS, DFRP of $M_{23}C_6$, and precipitation of the Laves phase must occur in the transient creep stage (Tamura & Abe, 2021a; 2021b; Tamura, 2022).

The QVC for *Gr.IIIa* of T91/MGC decrease sharply from the beginning of creep to an MCR point ($\varepsilon = 0.2 - 1.0\%$) and subsequently remains approximately flat or gradually increase until rupture (Tamura & Abe, 2021b). These decreases in the QVC during a transient creep stage should correspond to the metallurgical variations shown in Figures 7–10 although a strain to the MCR for *Gr.IIIa* is larger than that for the mcr of T91/MGC tested at 600 °C and 70 MPa ($\varepsilon \sim 0.36\%$). Therefore, to investigate these correspondences, the results of the $\Delta[QVC]_s$ analysis in *Gr.IIIa* of T91/MGC are shown in Table 5 (Tamura & Abe, 2021b). The analysis method is the same as that in Tables 3 and 4. Table 5 indicates that the determinants for $\dot{\varepsilon}$ in a transient creep stage are decreases in $\Delta[V_s]$ and ΔC_s , and those for $\dot{\varepsilon}$ in accelerating creep are essentially decreases in $\Delta[Q_s]$.

Table 5. Changes in Q_s , V_s , C_s , and $\log \dot{\varepsilon}$ between two adjacent strains for *Gr.IIIa* of T91/MGC steel

| Strain range | [0.2–0.5%] | [0.5–1%] | [1–2%] | [2–5%] | [5%– t_r] |
|--|---------------|--------------|-------------|-------------|--------------|
| $-\Delta[Q_s]$ | 17.09 | 9.94 | 5.52 | -6.39 | 11.55 |
| $\Delta[V_s]$ | -2.27 | -2.16 | -0.88 | 0.29 | -0.91 |
| ΔC_s | -15.91 | -8.02 | -4.24 | 6.97 | -9.40 |
| $\Delta \log(\dot{\varepsilon}, \%h^{-1})$ | -1.08 | -0.23 | 0.40 | 0.88 | 1.24 |

For $\varepsilon \geq 1\%$ during accelerating creep, the decreases in $\Delta[Q_s]$, i.e., the progress in recovery, are the determinants for increasing creep rates with an increase in strain. For $\varepsilon = 1 - 2\%$, $\Delta[V_s]$ decreases; therefore, the HRHD must already be active. In an accelerating creep stage for $\varepsilon \geq 2\%$, significant recovery should continue, because the QVC are small. However, for $2\% \leq \varepsilon \leq 5\%$, an increase in $\Delta[V_s] + \Delta C_s$ is the determinant and $\Delta[Q_s]$ increases and; however, the reason for this has not been discovered. However, the values of V remain the lowest throughout the entire strain range among all the groups (Tamura & Abe, 2021b; Figure 32). Therefore, the severe HRHD continues and the decomposition of microstructure, i.e., the formation of Z-phase consuming the strengthening particles of MX, occurs significantly, particularly during in accelerating creep (Tamura & Abe, 2021b).

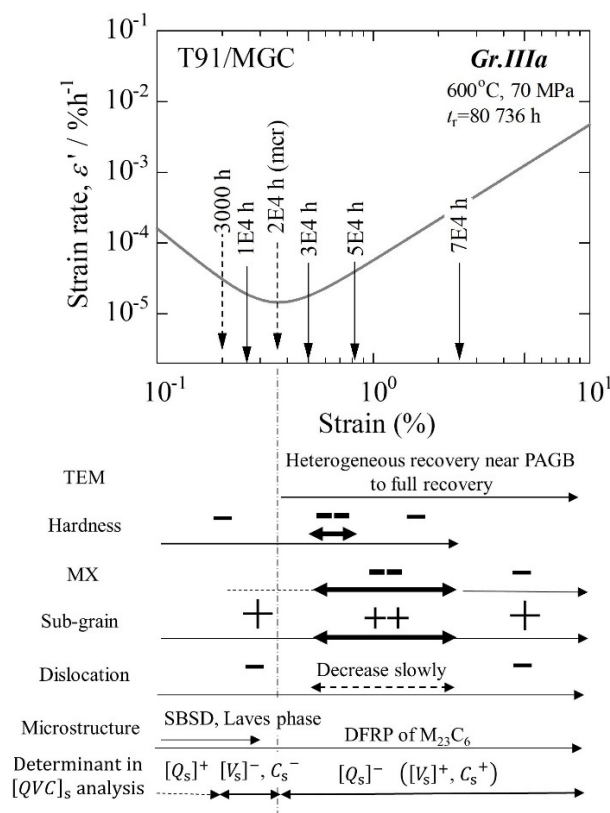


Figure 10. Schematic of the variations in TEM observation (TEM), hardness, number density of MX particles (MX), subgrain size (subgrain), dislocation density (dislocation), and hardening factors (microstructure) correlated with the creep strain (time) vs. strain-rate diagram of T91/MGC tested at 600 °C and 70 MPa. Determinant(s) in the $[QVC]_s$ analysis is(are) also indicated for each strain range. An mcr point occurs at 2E4 h (~0.36%) and are indicated by a vertical dashed line. The horizontal arrows show the strain ranges where metallurgical reactions occur. The symbols + and - on the arrows indicate the tendencies with increasing reaction strain and the bold or dashed horizontal lines indicate the qualitative degree of reactions. A superscript for each determinant in the $[QVC]_s$ analysis means an increase (+) or decrease (-) in the variable is the determinant for the changes in strain rate in a specific strain range; for example, $[Q_s]^-$ in an accelerating creep stage indicates a decrease in Q_s is a determinant for creep rate

For a transient creep of $0.2\% \leq \epsilon \leq 1\%$, a decrease in $\Delta[V_s] + \Delta C_s$ is the determinant, even though $\Delta[Q_s]$ decreases primarily owing to the coarsening of the Laves phase (Tamura & Abe, 2021b). That is, the decrease in $\Delta[V_s]$, or the decrease in V , is necessary to maintain transient creep. The decrease in V during transient creep means the heterogeneous recovery, and thus subsequent heterogeneous deformation, i.e., HRHD, occur elsewhere, because simultaneous decreases in QVC for the movement of dislocations in transient creep can never be explained successfully if the uniform deformation is assumed (Tamura & Abe, 2021a; 2021b). As shown in Figure 6, during the transient creep of the specimens for 3000 and 10 000 h at 600°C and 70MPa, the formation of the Z-phase in the gauge portion is confirmed in Figure 9 (Sawada et al., 2011). However, the amount of Z-phase in the gauge portion is considerably small; therefore, the consumption of finely dispersed MX particles is small. In these durations, in contrast to the formation of the Z-phase, the Laves phase particles grow sufficiently large. The sizes of the Laves phase particles are approximately 300 and 500 nm for 3000 and 10 000 h at 600°C, respectively, (Suzuki, Kumai, Kushima, Kimura, & Abe, 2000). However, the sizes of $M_{23}C_6$ remain approximately 100 and 200 nm for 3000 and 10 000 h at 600°C, respectively (Suzuki et al., 2000). Large particles typically accompany a recovered area around themselves; therefore, deformation is concentrated in the locally recovered area during creep. Laves phase particles typically precipitate on the PAGBs and sub-boundaries. Therefore, HRHD in the transient creep of T91/MGC should start near PAGBs or packet boundaries, although direct microstructural evidence for the existence of HRHD has not yet been discovered.

A locally recovered zone was certainly observed in a crept and ruptured specimen of T91/MGC tested with similar conditions as that of *Gr.IIIa* as shown in Figure 6. A locally recovered zone was also observed in a ruptured specimen of T92/MJT tested in conditions: 600°C, 120 MPa, and $t_r = 65\,363$ h (Sawada & Kimura, 2019), but it was not reported in the other heat or grade of high-strength martensitic steel.

However, the dislocation density decreased and the subgrain size increased in the transient creep stage of high-strength martensitic steels of P92/Dudko, P91Co/Dudova, X20/Bazazi, 0C, and 08C similar to T91/MGC, as shown in Figure 8. The QVC in a transient stage decreases simultaneously with increasing strain for each *Gr.IIIa* of P92/MJP, T92/MJT (Tamura & Abe, 2021b), and Grade 122 (Figures 4 and A8) similar to T91/MGC (Tamura & Abe, 2021b). Furthermore, determinants for creep rate in a strain range just before each mcr point of P92/MJP, T92/MJT (Tamura & Abe, 2021b), and Grade 122 (Table 4 and Section 4.3.4) are $\Delta[V]_s$ and ΔC_s according to each $[QVC]_s$ analysis. Therefore, heterogeneous recovery starts near the coarsened Laves phase particles; therefore, HRHD must start in the transient creep of *Gr.IIIa* of Grade 122 steels.

5.2 Estimation of the Initial State of Finely Dispersed VN Particles

5.2.1 Initial Dispersion State of MX Particles

The creep behavior in *Gr.I* of high-strength martensitic steel is strongly affected by the initial microstructures because the *Gr.I* of each steel is a data group tested sufficiently at low temperatures and within a short duration of time. The dispersion state of MX particles inside the subgrains can be estimated to a certain extent from the variations of Q corresponding to each *Gr.I* of the martensitic steels investigated, because Q means a parameter to represent the magnitude of the resistance to moving dislocations as explained in Section 2.2.2.

The short-term time parameters, t_ε and t_r , can be calculated under specific test conditions of temperature and stress using Equation 1 and the QVC s for each *Gr.I* of the martensitic steels investigated. Figure 11 shows the relationship between the Q s and the time parameters calculated of all steels investigated. In the figure, the results for each *Gr.I* of the plain steels 9Cr-1W and 9Cr-4W are also plotted. The conditions of 560 °C and 240 MPa were selected as the specific test conditions for the calculations, which are the rounded numbers of the grand averages of each average temperature and average stress for each *Gr.I* of all the steels investigated.

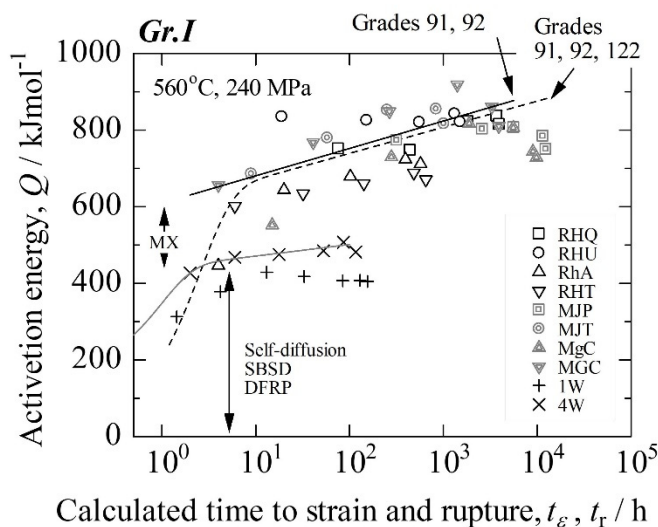


Figure 11. Relationship between the calculated time to strain or rupture and the activation energy for *Gr.I* of the steels is shown in the figure. Regression curves for 4W and Grades 91, 92, and 122 are drawn using solid and dashed lines, respectively. A linear regression line for Grades 91 and 92 was also drawn using a solid line

Recovery begins and thus Q decreases with progressing creep even under the test conditions for *Gr.I* of each steel in a later stage of creep as shown in Figures 4 and A4. Therefore, all data up to each Q_{\max} for each *Gr.I* of the steels of Grades 91, 92, and 122 are fitted to an equation of a type of $y = a \tanh(bx) + c \log x + d$ and the regression line is drawn using a dashed line. The proposed regression equation was imaged according to the dispersion state of all data analyzed. A similar analysis was performed on 9Cr-4W, and the results were drawn

using a solid line. A regression line for 9Cr-1W is not obtained because the number of data up to Q_{\max} was insufficient. However, the Q for 1W behaves similarly as those for 4W because the Q s for 1W are slightly below the regression line for 4W. A linear regression line was also added only for Grades 91 and 92 using a solid line.

The activation energy for all steels shown in Figure 11 increases rapidly from the beginning of creep and then the increasing rate ($\Delta Q/\Delta \log t$) suddenly slows down after 2–3 h and then increases steadily up to each Q_{\max} . From the previous works (Tamura & Abe, 2021a; 2021b; Tamura, 2022), the initial rapid increase in Q is caused by the SBSB reactions where a large number of excess dislocations inside the subgrains are rapidly annihilated with a help of several short circuit diffusion processes with small values of Q and/or swept out to the boundaries between the lath martensite, block, packet, and prior austenite grain and consequently, the accumulated dislocations increase the resistance to moving dislocations and thus the Q increases for a while. The accumulated dislocations begin to annihilate themselves and then the boundaries mentioned above begin to be redistributed and, on that occasion, $M_{23}C_6$ particles precipitated on the boundaries are also redistributed (DFRP), which results in gradual increase in Q with increasing creep time as shown in Figure 11 (Tamura & Abe, 2021a).

Based on these considerations self-diffusion, SBSB, and DFRP are responsible for the value of $Q \sim 400 \text{ kJmol}^{-1}$ for 9Cr-4W at $t \sim 2 \text{ h}$. The hardening reactions caused by the SBSB and DFRP should also occur in high-strength martensitic steel of Grades 91, 92, and 122. However, the Q values for these steels in spite of a large scattering around the regression line (a dashed line) are far larger than those for 1W and 4W steels. The spacing between the two regression curves is roughly constant regardless of the creep time and must be caused by the resistance to the moving dislocations; in other words, the existence of MX particles in Grades 91, 92, and 122 is schematically illustrated using “MX” in Figure 11. Therefore, it can be said that the Q values shown in Figure 11 are strongly affected by the dispersion state of MX particles for an individual steel, though Q is also affected by the dislocation density, subgrain size, and initial hardness as discussed in Section 2.2.2.

In Figure 11 all the Q values up to Q_{\max} for MJT (double circles), MGC (double inverse triangles), and RHU (circles) are on the upper side of the dashed regression curve. These data were obtained from the tubular products. MJP (double squares) and RHQ (squares) are pipe products and the corresponding Q values are near the dashed regression curve. On the other hand, MgC (double triangles) and RhA (triangles) are both steel plates, respectively, and RHT (inverse triangles) is a tubular product, but contains 5% of δ -ferrite. The Q values for MgC, RhA, and RHT are rather small. These facts suggest that the Q values for *Gr.I*s of high-strength steels are strongly related to the initial microstructure, or a product form itself. Certainly, tubular products are rather hard in general, and steel plates of the same Grade as tubular products are generally soft. Dislocation density of hard material may be high, and thus SBSB can easily occur in tubular products compared to the other soft materials, which results in high values of Q for *Gr.I* of the tubular products as seen in Figure 11.

The dashed regression curve in Figure 11 for all high-strength steel is slightly below the linear and solid regression lines for Grades 91 and 92. This means that the average Q value for four steels of Grade 122 for a given creep time duration for *Gr.I* is smaller than those for Grades 91 and 92. Furthermore, it is reminded from Table 1 and the data sheet of Grades 91 and 92 (NIMS, 2014; 2018, respectively) that martensite structure of Grade 122 is harder in HRC than Grades 91 and 92, which should increase in Q for Grade 122 and thus, the difference in Q in Figure 11 between Grade 122 and Grades 91 and 92 must be widened further when Grades 91, 92, and 122 steels have similar hardness. Therefore, the amount of finely dispersed MX particles inside the subgrains or the ρ_{MX} in the high-strength steel is primarily responsible for the difference in the values of Q for 4W and the high-strength steels as indicated in Figure 11 at least although the differences in the initial hardness of each steel should also be taken into consideration as mentioned above. Here, the ρ_{MXi} is highly correlated to the amount of MX inside the subgrains when the size of MX is small and roughly constant. Therefore, these two parameters are treated similarly, hereinafter ($\rho_{MXi} \sim \rho_{MX}$).

From the above discussions it can be said that the initial ρ_{MXi} s of the four steels of Grade 122 are in general smaller than those for Grades 91 and 92 and furthermore, among the eight steels investigated the initial ρ_{MXi} s for pl-91/MgC, pl-122/RhA, and DTB122/RHT are considered to be fairly small.

5.2.2 The Reasons for a Scattering of Q in Figure 11

The amount of MX particles or the ρ_{MXi} should be verified in more detail for individual steel, because there is a large scattering of Q in Figure 11.

First, regarding pl-122/RhA the Q s ($\leq Q_{\max}$) is positioned approximately 65 kJmol^{-1} smaller than and parallel to the linear regression line, excepting for the Q for $t \sim 3 \text{ h}$. An explanation for this exception is presented at the end of this section. The prior austenite grain size (PAGS) of RhA is fine because of the formation of Nb(C,N) during normalizing, as the nitrogen content of RhA is the highest among the four steels of Grade 122 investigated

(Table 1). Consequently, the number of precipitation sites during subsequent tempering of the fine PAGS material, RhA, increased, because the PAGBs act as precipitation sites for $M_{23}C_6$ and MX. Therefore, the number of MX particles that nucleated on the boundaries increases, and the precipitated MX particles on the boundaries are easily coarsened during tempering. Furthermore, Sawada, Taneike, Kimura, and Abe (2004) pointed out that VN particles precipitated easily grow when N content is high. Therefore, consequently, the amount of newly precipitated fine MX particles inside the subgrains becomes small for RhA, which relates to the low values of Q for $Gr.I$ of pl-122/RhA as shown in Figure 11 and maybe relates to the lowest hardness among the four steels of Grade 122 (See Table 1).

Regarding pl-91/MgC (plate), the Q for $t \sim 15$ h of MgC is low as shown in Figure 11, but after that the Q increases with an increase in creep time and then the Q_{max} ($t \sim 1800$ h) approaches to the Q values for the other steels. The low value of Q for $t \sim 15$ h may be caused by two reasons; stress relieving treatment was performed before the creep tests and $Gr.I$ of MgC contains low temperature data tested at 450 °C. A rapid increase in Q of MgC is caused by the precipitation of Laves phase, Fe_2Mo , because a nose temperature of the TTP curve for Fe_2Mo is approximately 550 °C (Tamura et al., 1988; Tamura, 2022) and this temperature is nearly equal to the calculating temperature for Figure 11. The precipitation of the Laves phase also occurs in $Gr.I$ of T91/MGC, and thus as shown in Figure 11 the increasing rate in Q ($\Delta Q/\Delta \log t$) for T91/MGC is larger than that for T92/MJT whose Laves phase is Fe_2W not Fe_2Mo . A nose temperature for Fe_2W is approximately 650 °C (Tamura et al, 1988) and thus Fe_2W scarcely form at a calculation temperature of Figure 11 (560 °C).

The PAGS of T122/RHT is easy to become fine from two reasons: the N content is rather high and thus Nb(C,N) is easily formed during normalizing and further RHT contains 5% of δ -ferrite. Consequently, RHT is the hardest among the four Grade 122 steels (Table 1). Furthermore, the amount of newly precipitated fine VN particles inside the subgrains during tempering becomes small for the same reason as that for pl-122/RhA. In this case, the amount of fine MX particles inside the subgrains for RHT is smaller than that for RhA because of the finer PAGS for RHT and the smaller amount of N content in RHT as compared to those for RhA (Table 1). Thus, the Q values for RHT may be smaller than those for RhA. However, the higher hardness of RHT than RhA should increase in Q through an increase in back stress. Therefore, both phenomena mentioned above are balancing and thus the Q s for each $Gr.I$ of RHT and RhA are comparable as seen in Figure 11.

The Q value for $t \sim 20$ h of T122/RHU is extremely high. The N content of MGC, MJT, and RHU are 0.044, 0.0462, and 0.057, respectively and the values of Q ($< Q_{max}$) for these steels are located on an upper side of the linear regression line in Figure 11. The PAGS of the RHU is coarser than that of the MGC and MJT (Table 1; Tamura, Abe, 2021b). Therefore, the amount of fine MX particles precipitated inside the subgrains is larger than those of MGC and MJT and, in addition to this estimation, the high hardness of RHU (Table 1) raises the Q value through the increase in the back stress in Q for $Gr.I$ of RHU, if we consider similarly to the cases of RhA and RHT mentioned above. However, there is little difference in Q between RHU and MJT for approximately 1000 h. The finely dispersed MX particles are generally stable and do not easily coarsen upon heating for approximately 1000 h at a temperature for the $Gr.Is$ (Kabadwal, Tamura, Shinozuka, & Esaka; 2010). Therefore, the large value of Q for $t \sim 20$ h for T122/RHU shown in Figure 11 is caused by high density of induced excess dislocations. The excess dislocation density is possibly reduced to some extent even under the creep conditions of $Gr.I$ referring to previous work (Kadoya & Shimizu, 2000; Ennis & Czyska-Filemonowicz, 2003; Bazazi, 2009).

The value of the initial Q (~ 3 h) for RhA is in the opposite side of the Q for RHU in Figure 11. The low value of Q and the low number of HRC (Table 1) for RhA suggest that the initial dislocation density of RhA may be low. However, the Q approaches to a considerably high value for up to approximately 20 h and therefore, the low value of initial Q for RhA is not caused by the low dislocation density, but rather is in a transient stage (a rapid increasing stage in $\Delta Q/\Delta \log t$) of the dashed regression curve shown in Figure 11.

5.2.3 A New Role of MX Particles

Figure 12 shows the relationship between the V s and the time parameters, t_e and t_r , for $Gr.Is$ of the high-strength martensitic steels and the 9Cr-W steels. The indication method in Figure 12 is the same as that in Figure 11, but the regression line for 9Cr-4W is linear. The graphical features of Figure 12 are quite similar to those shown in Figure 11. Figure 12 shows that the V s for high-strength martensitic steels are clearly larger than those for a plain steel of 9Cr-4W and, therefore, the existence of finely dispersed MX particles inside the subgrains is primarily responsible for these differences. MX particles inside the subgrains disturb the glide motion of dislocations and therefore, the existence of MX must reduce V , because V is an indicator to the average movable area for a dislocation (Tamura & Abe, 2021a). However, Figure 12 shows unexpected and opposing evidence.

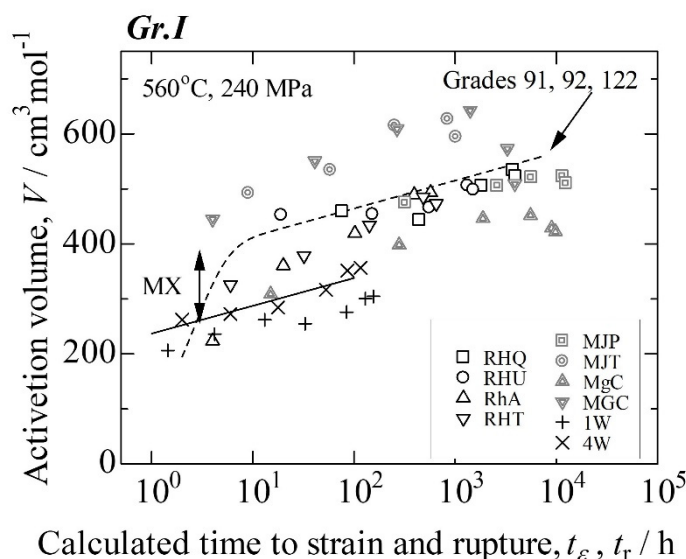


Figure 12. Relationship between the calculated time to strain or rupture and the activation volume for *Gr.I* of the steels shown in the figure. Regression lines for 4W and Grades 91, 92, and 122 are drawn using a solid line and a dashed line, respectively

It is reminded that HRHD occurs when the V is small (Tamura & Abe, 2021a). Namely, Figure 12 surely indicates that in the first place 9Cr-4W of plain martensitic steel deforms heterogeneously and, therefore, finely dispersed MX particles make the deformation of the high-strength martensitic steel less-heterogeneous and, thus, the V increases. This interpretation of Figure 12 seems to be incompatible with the results shown in Figure 11. That is not the case. Rather, finely dispersed MX inside the subgrains in martensitic steel not only increases the creep strength but also suppresses the occurrence of HRHD, which should mitigate the unexpected drops in the long-term rupture strength of high-strength martensitic steel if the MX particles are stable for a long duration. In other words, the long-term rupture strength of high-strength martensitic steel is lowered when the finely dispersed MX particles are disappeared. Namely, a new role of finely dispersed particles of MX in martensitic steel is highlighted.

Morooka, Tomota, Adachi, Morito, and Kamiyama (2008a) and Morooka, Tomota, and Kamiyama (2008b) employed both an electron back-scattered diffraction method and a neutron diffraction method to clarify that martensite deforms heterogeneously inside the sub-block of martensitic structure. Moreover, Mitsuhashi (2022) reported that Al alloy of a precipitation hardening type, A2017, deforms more uniformly as compared to Al-4.5% Mg alloy with coarse grains of a solid-solution hardening type. Therefore, the interpretation of Figure 12 is reasonable.

Most interpretations for creep phenomena, except for the welded joint, notched structure, and necking behavior have been made based on the assumption of uniform deformation. The creep of martensitic steel should be also no exception to this assumption. Therefore, the simultaneous increases in QVC of martensitic steel in an initial stage of creep are interpreted as results of the SBS, the DFRP mechanism to $M_{23}C_6$, and the precipitation hardening of the Laves phase (Tamura & Abe, 2021a; 2021b). However, the reaction rates of these metallurgical responses become shortly slow down and then the QVC begin to decrease even in transient creep. This is the start of non-uniform deformation (HRHD). In an HRHD zone, the decomposition of the microstructure is severely promoted, which triggers unexpected drops in the long-term rupture strength. In *Gr.I*s for each steel shown in Figures 11 and 12, the HRHD seems to begin from approximately 1000 h, when QVC peak. However, there is no doubt that the existence of finely dispersed MX particles inside the subgrains should suppress the occurrence of the HRHD if MX particles are stable for a long period of time.

5.2.4 Index Representing the Amount or Number Density of MX Particles Inside the Subgrains

Figure 11 was interpreted on average as the difference in Q for *Gr.I* between high-strength steel and 9Cr-4W is caused by the existence of MX particles. However, it is also reminded that Q is affected by many kinds of factors

such as precipitation of the Laves phase, initial dislocation density, hardness or stiffness of martensite structure, which causes the scattering of Q as discussed in Section 5.2.2. Therefore, it is hard to say that the difference in Q for *Gr.I* between a specific high-strength steel and 9Cr-4W is an adequate index for the total amount of MX particles, much less the amount of MX inside subgrains.

On that point the difference in V for *Gr.I* between specific high-strength steel and 9Cr-4W steel shown in Figure 12 rather than Q can be an index representing ρ_{MXi} on average, because V is a parameter representing the movable area of dislocations inside subgrains as explained in Section 2.2.5. V is affected by the existence of dislocations inside the subgrains, but as explained in Section 5.2.1 the effect is mitigated during creep for approximately 1000 h at 560 °C. However, the above-mentioned assumption that the difference in V is an index for ρ_{MXi} must be examined.

Sawada et al (2014) showed employing scanning TEM-energy dispersive spectroscopy that the ρ_{MX} of MgC is approximately 60% of that of MGC before the creep test. This difference in ρ_{MX} should introduce the difference in the resistance to moving dislocations inside the subgrains. Therefore, the difference in V between MgC and MGC should be correlated with ρ_{MXi} inside the subgrains not ρ_{MX} in total. However, in an early stage of creep we can assume $\rho_{MXi} \sim \rho_{MX}$. Therefore, when we think this way, the difference in V between two steels of MGC and MgC can be correlated with the difference in ρ_{MX} (i.e., 100-60=40%). Certainly, Figure 12 shows that the V s for *Gr.I* of MgC are clearly smaller than those of MGC, respectively, before the V peaks. This qualitatively coincides with the Sawada's observations. Therefore, the difference in V between two steels or the different stages of the same steel ought to be possibly used as a qualitative index of the difference in the amount or the ρ_{MXi} neglecting the difference in basic martensitic structure between the two steels.

When the ρ_{MXi} of MgC at an early stage of creep is smaller than that of MGC, the deformation mode of MgC become close to that of 4W, i.e., heterogeneous deformation. If the lower value of ρ_{MXi} continues for a long duration of time, the HRHD occurs more easily in MgC than MGC. In this case it is estimated that the rupture strength of MgC is lower in *Gr.IIIa* more severely than that of MGC, because the Z-phase is easily formed, consuming finely dispersed MX particles owing to the severe decomposition of the microstructure in the HRHD zone. However, contrary to this estimation the opposite results are obtained: The consumption of MX particles in MgC is smaller than that of MGC and the ρ_{MX} of MgC is larger than that of MGC after rupture for approximately 8E4 h. As a matter of course, rupture strength of MgC for approximately 8E4 h is higher than that of MGC (Sawada et al., 2014). Sawada et al. (2014) explained these phenomena as the Ni content of MgC (0.04%) being smaller than that of MGC (0.28%). Like this, the initial ρ_{MX} is not the only determinant factor for the long-term rupture strength of high-strength martensitic steel. In addition, there may be other important factors that control long-term rupture strength. However, it is reasonable to increase the initial Q and V calculated from the tests performed at low temperature and high stresses, because finely dispersed MX particles promote homogeneous deformation and increase creep strength. Therefore, the initial Q and V obtained at low temperatures and under high stresses are considered to be appropriate indexes of alloy design for high-strength martensitic heat-resistant steel.

Sawada et al. (2006) also reported the elemental color maps crept for approximately 3E4 h at 600 °C in grip and gauge portions of DTB122/RHT and T91/MGC, respectively. The ρ_{MXs} in the both portions for DTB122/RHT seem to be smaller than those for T91/MGC in each color map. There are many differences between these two steels such as W and Mo content, amount of δ -ferrite, and initial hardness, but Ni concentrations, one of the important indexes for recovery rate of martensitic structure, in each steel are at similar level, 0.33% and 0.28% for RHT and MGC, respectively. Therefore, if we can assume the consuming rate of finely dispersed MX particles for RHT and MGC is similar with each other, we can estimate the ρ_{MXi} for RHT is smaller than the ρ_{MXi} for MGC before the creep test.

In this discussion, the effect of Laves phase precipitated in MGC on the differences in Q and V is neglected. The reasons for this are as follows: Concerning V , enough differences are confirmed in Figure 12 between the V s of MGC and RHT and moreover, the Laves phase does not essentially have an impact on the moving area of dislocations inside the subgrains because the Laves phase precipitates on the boundaries.

Furthermore, this doctrine that V is an adequate index for the ρ_{MXi} maybe also be applied for a long duration of time, because the V values for RHT and MGC for 3E4 h at 600 °C are 185 (Figures A3 and A8) and 286 (Tamura & Abe, 2021b) $\text{cm}^3\text{mol}^{-1}$, respectively, and thus, a positive correlation between the V values mentioned here and the ρ_{MXs} shown in the color maps reported by Sawada et al. (2006) for RHT and MGC is confirmed.

5.2.5 Introduction of N_{av}

Total and maximum amount of MX particles formed during tempering can be estimated using a new parameter, the available nitrogen concentration, N_{av} , defined by the next equation.

$$N_{av} = N - Al - Ti - Nb - B \text{ (at\%)}. \quad (9)$$

This parameter was originally introduced by Abe, Tanaka, and Murata (2007b) to explain a large heat-to-heat variation in the long-term rupture strengths of 12Cr-1Mo-1W-0.3V steel and stainless steels of Types 304HTB and 316HTB. In Equation 9, it is assumed that TiN is formed during solidification, BN with a hexagonal structure and Nb-rich (Nb,V)(C,N) with a cubic structure of type MX are formed during normalizing, the solubility product for AlN in ferrite is smaller than that for VN, Cr₂N is not formed, and the effect of Cr on the precipitation reactions can be ignored. Therefore, only V-rich MX, i.e., VN, is a major nitride formed during tempering and, thus, the maximum amount of VN precipitated during tempering is the atomic concentration of vanadium times N_{av} . All the steels investigated contain sufficient V to form the VN compound. In the case of RHT, V may be concentrated in δ -ferrite. Even if the V concentration in δ -ferrite is assumed to be twice of the martensite matrix of RHT, the matrix still contains enough V to form VN.

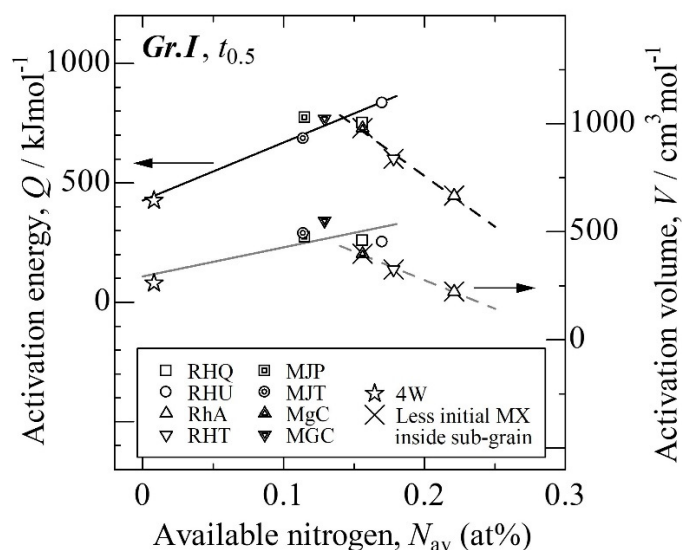


Figure 13. Activation energy and activation volume for $t_{0.5}$ of *Gr.I* as functions of N_{av}

Figure 13 shows the Q and V as functions of N_{av} for *Gr.I* and $t_{0.5}$ of high-strength martensitic steels investigated. Data points for 4W (Tamura & Abe, 2021a; $N_{av} = 0.008$ at%) are also plotted in Figure 13. Dashed regression lines are for MgC, RhA, and RHT marked by crosses in Figure 13 with less ρ_{MX} , which is a main conclusion deduced from Figure 11 (cross marks are used for similar diagrams, hereinafter), and solid regression lines are for the others including 4W. The Q in Figure 13 is naturally expected to increase along a solid line with increase in N_{av} as a parameter for fine VN particles precipitated during tempering. However, a dashed line for the Q s of MgC, RhA, and RHT with less amount of MX particles inside the subgrains indicates that the Q decreases with increasing N_{av} when the N_{av} is larger than approximately 0.15 at%. Usually, a certain amount of VN particles precipitate on the boundaries of the subgrains including prior austenite grains and easily coarsened. Even in these cases, Q should increase with an increase in N_{av} . However, the Q s in Figure 13 behave inversely when $N_{av} > 0.15$ at%. Namely, the larger the N_{av} concentration is, the more the number is or the larger the VN particles precipitated on the boundaries is when $N_{av} > 0.15$ at%. The later estimation of the coarse particles of VN is supported by the experimental observation that precipitated VN particles easily grow when the N content is high (Sawada et al., 2004). In both cases the Q decreases with an increase in N_{av} , because the amount of finely dispersed MX particles precipitated inside subgrains during tempering decreases with an increase in N_{av} concentration when $N_{av} > 0.15$ at%.

Figure 13 also shows that the V behaves similarly as the Q does. The average $t_{0.5}$ for *Gr.I* of RhA can be estimated from the QVC of RhA as approximately 4 h. The values of Q and V for *Gr.I* and $t_{0.5}$ (~4 h) of RhA are low and comparable to those of 4W, as shown in Figures 11 and 12. This means naturally that RhA with less ρ_{MX} deforms heterogeneously in an early state of transient creep similarly as 4W does which does not contain V and thus any of MX particles.

5.3 Determinant Factors in HRC at Ambient Temperature

Tensile strength (TS), HRC, and PAGSn are typical inspection parameters for shipping of martensitic steel. Figure 14 shows the correlations between PAGSn and the hardness of the eight steels of Grades 91, 92, and 122 (Table 1; NIMS, 2014; 2018). The HV and PAGS for 9Cr-4W are 211 and 50 μm , respectively (Abe, Araki, & Noda, 1991; Tamura & Abe, 2021a). These data were converted to HRC and PAGSn and are plotted in Figure 14. The plotted data, including 4W, can be stratified into two areas; Grade 122 (open marks) and Grades 91, 92, and 4W (double marks). Guide lines shown in Figure 14 are not regression lines for each data group, but virtual lines considering the decreasing effects of the ρ_{MX} (MgC, RhA, and RHT), stress relieving (MgC), and δ -ferrite (RHT) and also increasing effects of the relatively low temperature tempering (EHQ, RHU, RhA, MgC, and MGC) and induced excess dislocations (RHU, MJT, RHT, and MGC of tubular products) on hardness based on the state of MJP.

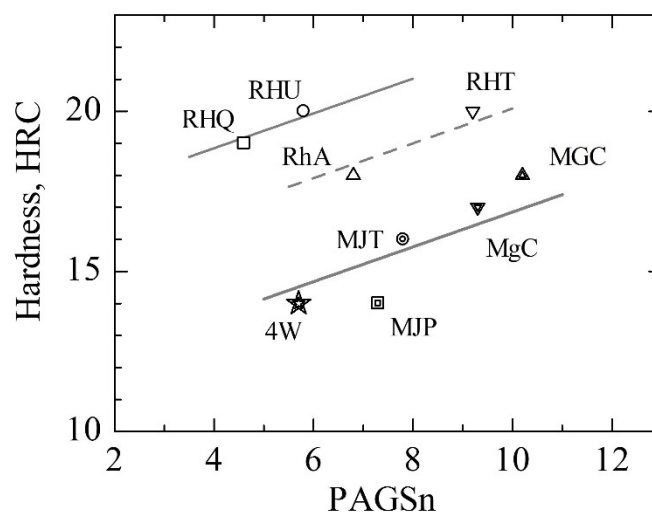


Figure 14. Relationship between PAGS number and hardness. Guide lines shown are not the regression lines, but virtual lines explained in Section 5.3

The two stratified data groups are intuitively considered to be characterized by Cr, C, and N contents because both C and N concentrations for Grade 122 (0.12% and 0.062% on average, respectively) are higher than those for Grades 91 and 92 (0.10% and 0.049% on average, respectively). However, hardness should be formulated using metallurgical parameters such as tempering parameter (TP) and PAGS number (PAGSn) when the following metallurgical reactions are assumed: During normalizing, only NbN is formed by consuming Nb and the PAGS is determined. During tempering, dislocation density largely decreases with increasing TP, subgrains begin to form, and Cr_{23}C_6 and VN are formed consuming C and N, respectively and therefore, it is natural to consider that there is little soluble C, N, and Nb, but free V (V_{free} , hereinafter) is still remained in the matrix before the tests. Of course, it is assumed there is neither δ -ferrite nor Laves phase. Hardness data of 15 heats of Grades 91, 92, and 122 (NIMS, 2014; 2018; 2020; 2021) excepting RHT with δ -ferrite and MgA, MgB, and MgC with a stress relieving treatment (SR) are analyzed according to the model mentioned above and the next regression equation was obtained.

$$\begin{aligned} \text{HRC} = & 93.33 - 2.70TP/1000 + 0.87\text{PAGSn} + 3.04\text{Si} - 13.44\text{Mn} - 8.59\text{Ni} + 11.62\text{Cu} \\ & + 5.55(\text{Mo} + \text{W}) + 12.55V_{\text{free}} - 13.74\langle\text{VN}\rangle + 2.42\text{Cr}_{23}\text{C}_6 - 44.63\text{NbN}. \end{aligned} \quad (10)$$

All elements are given by at%, and the variables in Equation 10 are defined by the following equations:

$$TP = T(30 + \log t), \quad (11)$$

where T is a tempering temperature in K and t is tempering time in h.

$$V_{\text{free}} = V - N_{\text{av}}, \quad (12)$$

$$\text{Cr}_{23}\text{C}_6 = 29/6 \cdot C, \quad (13)$$

$$\text{NbN} = 2\text{Nb}, \quad (14)$$

and

$$\langle VN \rangle = 2|N_{av} - 0.15|. \quad (15)$$

All variables in Equations 12–15 are calculated in at%. Figure 15 shows that the precipitation hardening caused by VN particles finely dispersed inside the subgrains is maximized when $N_{av} = 0.15$ at% and thus the amount of this hardening, ΔH_{VN} , should be proportional to

$$\Delta H_{VN} \propto \text{constant} - \langle VN \rangle \quad (16)$$

or ΔH_{VN} becomes maximum when $N_{av} = 0.15$ at%. Therefore, the regression coefficient for $\langle VN \rangle$ in Equation 10 is negative. The constant in Equation 16 cannot be determined because it is included in the interceptional term of Equation 10, but there is no problem.

Figure 15 shows the correlation between the observed and calculated HRC using Equation 10. In the figure data of T122/RHT, Type 91 of MgA, MgB, MgC, and 9Cr-4W, which are excluded from the regression analysis because of containing δ -ferrite or SR treatment, are also plotted. A high correlation was confirmed between the observed and calculated HRC from Equation 10. It is quite natural that the observed HRCs with SR treatment (MgA, MgB, and MgC) and with δ -ferrite (4W) are smaller than those for the calculated, but the observed HRC of RHT with δ -ferrite is comparable with the calculated HRC and thus, RHT must be strengthened by some other mechanisms such as fine subgrain size.

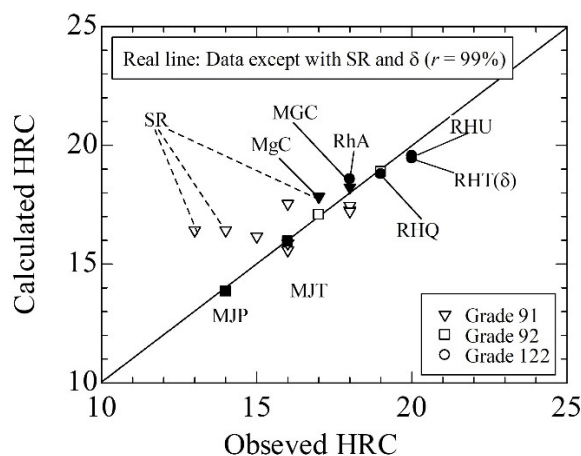


Figure 15. Correlation between observed and calculated hardness, HRC. The regression line is given for the steel without δ -ferrite or SR treatment. The solid marks indicate the steels investigated in detail in this study

As shown in Figure A11, HRC shows a high correlation with the TS at ambient temperature. Therefore, to support the reasonability of the regression analysis for HRC, the TS data at ambient temperature of Grades 91, 92, and 122 were analyzed using the same method as that of HRC and the next regression equation was obtained.

$$TS(\text{MPa}) = 2410 - 58.4TP/1000 + 8.59PAGSn + 84.14Si - 84.6Mn - 59.7Ni + 144.1Cu + 173.2(Mo + W) + 275.3V_{\text{free}} - 364.7\langle VN \rangle + 16.9Cr_{23}C_6 - 827NbN. \quad (17)$$

All the elements are given by at% and the variables in Equation 17 are the same as those in Equation 10. Figure 16 shows the correlation between the observed and calculated TS values using Equation 17. A high correlation coefficient was confirmed, similar to that in Figure 15. The signs of the independent variables and intercept term of Equations 10 and 17 are perfectly same with each other. Therefore, the regression analysis for HRC indicated by Equation 10 is considered reasonable.

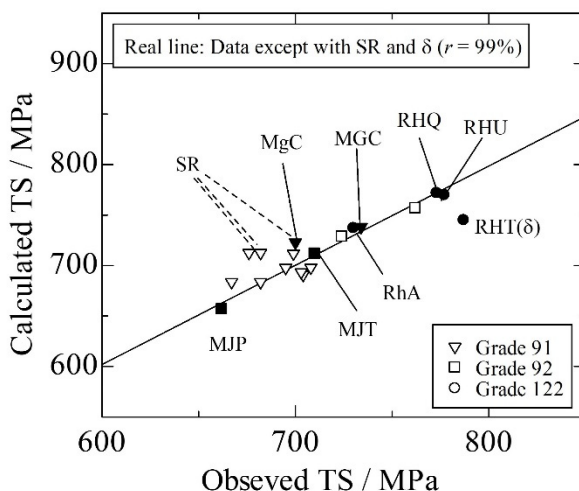


Figure 16. Correlation between observed and calculated TS at ambient temperature. The notation methods are similar to those in Figure 15

To compare the proportions of each variable, including the intercept term of Equations 10 and 17, Figure 17 shows the component proportion ratios of each variable for HRC and TS, where each regression coefficient multiplied by the average of the variables in Equations 10 and 17 is divided by the average HRC and TS. It is clear from Figure 17 that the HRC and TS at ambient temperature of the tempered martensitic structure are roughly determined by the first and second terms of Equations 10 and 17, which correspond to the hard martensite structure induced by normalizing being largely softened by decreasing dislocation density and related metallurgical reactions during tempering. However, Figure 17 also indicates that the remaining variables cannot be neglected.

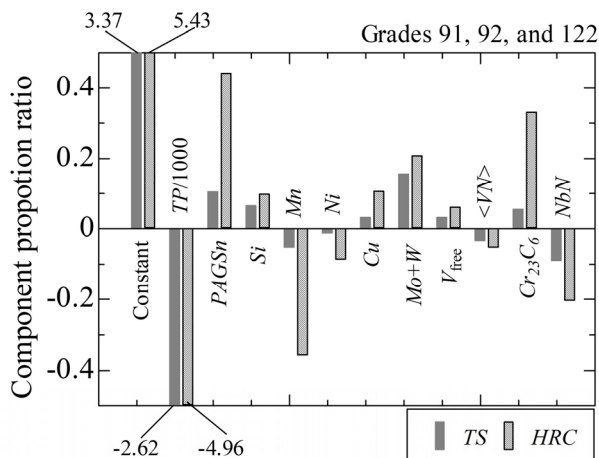


Figure 17. Component proportion ratio for the average values of each variable in Equations 10 (*HRC*) and 17 (*TS*), where each regression coefficient multiplied by the average of the variables in Equations 10 and 17 is divided by the average *HRC* and *TS*

To understand deeply the meaning of the difference between two stratified data groups shown in Figure 14 which shows the correlation between PAGSn and HRC for Grades 91 and 92 and Grade 122, Figure 18 indicates the partial contributions of basic strength, $PAGSn$, $Cr_{23}C_6$, $\langle VN \rangle$, NbN , and V_{free} in the calculated HRC for each heat of Grade 122 and moreover, the averages for the Grades 91 and 92 are also shown in the figure by using horizontal bars, where the basic strength means the summation of the terms for intercept, $TP/1000$, Si , Mn , Ni , Cu , $Mo + W$. The partial contribution of the basic strength must correspond to the fundamental strength and stiffness of the tempered martensite, excluding the contribution from precipitates such as $M_{23}C_6$ and VN. The partial contributions of the basic strength for Grade 122 were clearly larger than the average for Grades 91 and 92. Similar results for the TS at ambient temperature (Figure 18) are shown in Figure A12.

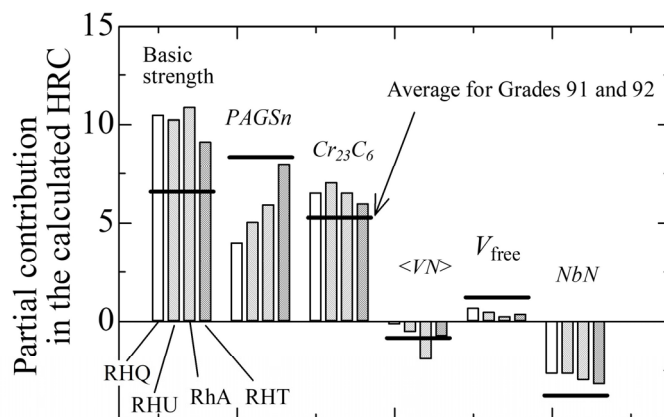


Figure 18. Partial contributions to the calculated HRC for Grades 91, 92, and 122. The meanings of basic strength, $\langle VN \rangle$, and V_{free} are explained in Section 5.3

Positive contributions of $M_{23}C_6$ and V_{free} on HRC are metallurgically reasonable. Although the contribution of $\langle VN \rangle$ is negative feels strange, there is no problem because the effective hardening by finely dispersed VN particles, ΔH_{VN} , is defined by Equation 16. However, the negative effect of NbN is surprisingly large and comparable to the differences in basic strength between Grade 122 and the average of Grades 91 and 92. The t -value for the regression coefficient for NbN, $t = -0.67$, is rather low and the variable of NbN probably should be deleted, but this should be solved in future.

Figure 19 shows correlation between PAGSn and HRC for all heats of Grades 91, 92, and 122 reported in NIMS data sheets (2014; 2018; 2020; 2021). A guideline is a regression line for all heats of Grades 91 and 92 using a regression coefficient of $PAGSn$ on Equation 10, i.e., 0.87. In Figure 19 data for 4W is plotted and seems to be along the guideline, but the HRC for 4W without δ -ferrite should probably be positioned at higher. The three Grade 91 heats subjected to SR treatment are plotted in Figure 19. HRCs for these heats might be higher before each SR treatment, and thus the two of three, at the bottom of the line, may approach the guideline. In this case, HRC of MgC might be higher, but the ρ_{Mxi} of MgC is small as explained in Section 5.2.1, Figures 11 and 13 or the contribution of $\langle VN \rangle$, effective VN particles, in Equation 10 is small and thus HRC of MgC remains near the guideline owing to balancing SR and $\langle VN \rangle$ effects.

Figure 19 shows that the HRC values for Grade 122 are clearly higher than the PAGSn vs. HRC correlation for Grades 91 and 92. The primary reason for this is that the basic strength of the tempered martensite of Grade 122 is higher than the average basic strength of Grades 91 and 92 although the PAGSn of Grade 122 are coarser than the average for Grades 91 and 92. However, the effect of $M_{23}C_6$ cannot be neglected leaving aside a problem on NbN with a low t -value.

The size of $M_{23}C_6$ carbide particles in Type P92 steel tempered at 720–775 °C before the creep tests is ranging 90–120 nm or 103 nm in average (Hättestrand, & Andren, 2001; Ennis & Czyrska-Filemonowicz, 2003; Dudko, et al., 2013; Jiang, Zhu, & Wang, 2013) and that in T91/MGC tempered at 765 °C is 105 nm (Suzuki et al., 2000). On the other hand, Straub et al. (1993) reported the size of $M_{23}C_6$ carbide particles as 65 nm in X20CrMoV12-1 which is normalized at 1050 °C followed by tempering at 760 °C for 1 h. These facts can be interpreted as the size

of the $M_{23}C_6$ particles in tempered martensitic steel with high carbon and high chromium content may be fine and numerous, although the size of $M_{23}C_6$ is affected by many metallurgical factors such as heat treatment conditions. Therefore, it is estimated that the size and total amount of $M_{23}C_6$ in Grade 122 with larger contents of Cr and C are finer and much greater than those of Grades 91 and 92 steel, and finer $M_{23}C_6$ carbide particles are formed along the packet, block, and lath boundaries as compared to Grades 91 and 92. Therefore, the martensite structures of Grade 122 before the creep tests are finer and stiffer than those of Grades 91 and 92, or that finer and more $M_{23}C_6$ carbide particles in Grade 122 directly raise the HRC and indirectly raise the basic strength of the tempered martensite as compared to Grades 91 and 92 as shown in Figure 18.

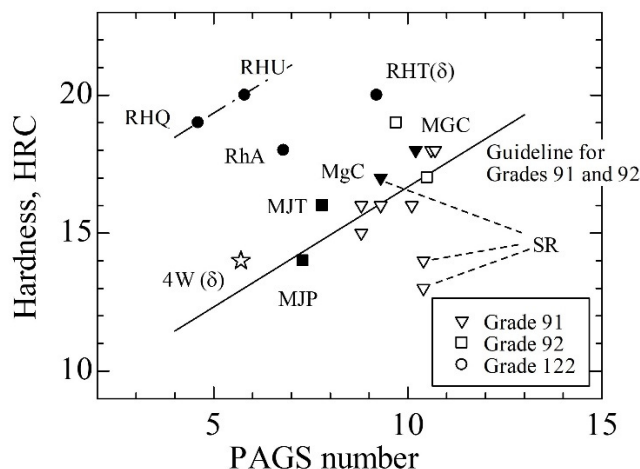


Figure 19. Correlation between PAGSn and HRC for all heats of Grades 91, 92, and 122 reported in NIMS Data Sheets (2014; 2018; 2020; 2021) and 4W. The solid marks indicate the steels investigated in detail in this study

The HRC for RhA was smaller than that for RHQ and RHU, as shown in Figure 19. This is because the ρ_{MXi} estimated from Figure 11 for RhA is low as explained in Section 5.2.1. Consequently, the partial contribution in HRC of $\langle VN \rangle$ for RhA is negatively larger than other Grade 122 steels as shown in Figure 18. The HRC for the RHT was also smaller than those for RHQ and RHU as shown in Figure 19. This is because RHT contains δ -ferrite in addition to the same reason for the RhA mentioned above.

5.4 Relationship Between Creep Strength and Initial State of Microstructure

It is well-known that the long-term rupture strength of high-strength martensitic steel with Nb, V, and N drops unexpectedly, consuming finely dispersed MX particles inside the subgrains (Kushima et al., 1999; Suzuki et al., 2003; Sawada, Kushima, & Kimura, 2006; Danielsen, 2007; Hald, 2008; Kimura et al., 2013). However, the relationships between the initial microstructural parameters and the short- and long-term creep strengths have not been thoroughly clarified. First, Figure 20 shows the hardness at ambient temperature and creep strength at 600 °C for $Gr.I$, 0.5% strain and 3 h, $\sigma_{0.5}$, of all steels investigated including 4W as functions of N_{av} which is a parameter representing the amount of MX. The $\sigma_{0.5}$ s can be calculated under a given temperature and time for a specific strain using Equation 1 and the related QVC s (Table 4; Tamura & Abe, 2021b; Tamura, 2022) for each $Gr.I$ of the martensitic steels investigated.

The dashed regression lines in Figure 20 are for all the steels investigated, including 4W. Solid regression lines are for all steels excluding the steels with less ρ_{MXi} , i.e., MgC, RhA, and RHT. Figure 20 indicates that the N_{av} and HRC have a rather high positive correlation regardless of the presence of the steels with less ρ_{MXi} , which corresponds to the results shown in Figure 18 that the predominant determinants in the calculated HRC are the basic strength of tempered martensitic structure, PAGSn, and $M_{23}C_6$ and that the partial contribution of $\langle VN \rangle$ in the calculated HRC is considerably small.

However, completely different phenomena occur in the condition of short-term creep of $Gr.I$ at 600 °C; all of the $\sigma_{0.5}$ s at 600 °C seem to be independent of N_{av} as a whole, because the $\sigma_{0.5}$ s for MgC and RhA are considerably small. In contrast, finely dispersed MX particles inside the subgrains effectively raise the $\sigma_{0.5}$ during creep of $Gr.I$, because a high value of correlation coefficient ($r = 78\%$) is obtained for all steels excluding the steels with less ρ_{MXi} and the $\sigma_{0.5}$ s for the steels with less ρ_{MXi} are low compared to the others, and especially the $\sigma_{0.5}$ s for MgC

and RhA are lower than that for simple steel of 4W without MX. Namely, coarse MX particles formed on the boundaries of MgC and RhA cause a negative impact on creep strength of $\sigma_{0.5}$ for *Gr.I* at 600 °C.

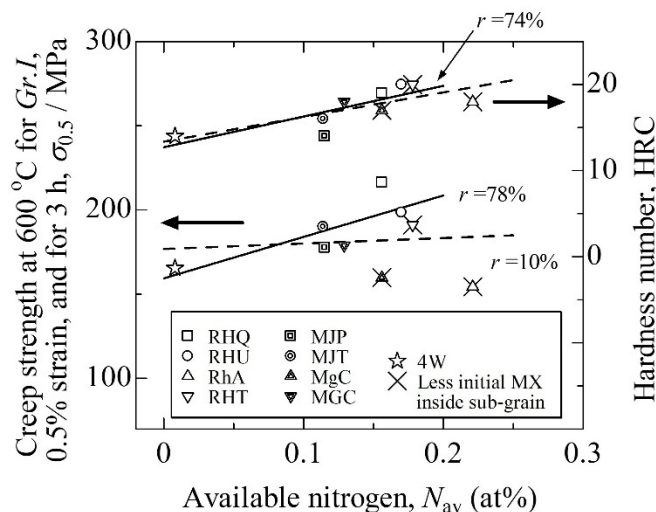


Figure 20. Creep strength for *Gr.I* at 600 °C and 0.5% strain and for 3 h, $\sigma_{0.5}$, and hardness at ambient temperature as functions of available nitrogen concentration, N_{av} , of martensitic steel including 4W. Dashed regression lines are for all data, and solid lines are for all data without data of less initial MX inside the subgrains

Figure 21 shows the proof strength PSs, the $\sigma_{0.5}$ s of *Gr.I* for 3 h, and the rupture strengths (σ_{tr}) of *Gr.IIIa* for 1E5 h at 600 °C as functions of N_{av} for Grades 91, 92, and 122, but without 4W. The σ_{tr} s can be calculated in the same method as $\sigma_{0.5}$ mentioned above. The solid regression lines are for all steels excluding MgC, RHT, and RhA with less ρ_{MXi} marked by crosses and the dashed regression lines are for all steels investigated.

It is first found from Figure 21 comparing solid and dashed regression lines for the PSs and the $\sigma_{0.5}$ s that the harmful impact of the coarse MX particles precipitated on the boundaries become significant during creep ($\sigma_{0.5}$ for *Gr.I*) as compared to short time tensile deformation (PS). This is first because MgC, RHT, and RhA with less ρ_{MXi} should contain a greater number of coarse MX particles on the boundaries and secondary because the $\sigma_{0.5}$ s for MgC and RhA are smaller than those for MJP, MJT, and MGC although the PSs for these steels are just comparable.

This negative impact of coarse MX particles seems to be disappeared during long-term creep (σ_{tr} of *Gr.IIIa*) and the σ_{tr} for 1E5 h in each *Gr.IIIa* seem to decrease with increasing N_{av} . However, such negative impact of N_{av} on the strength for *Gr.IIIa* is open to misunderstanding. Rather, it is reasonable to understand that a considerable amount of finely dispersed MX particles inside the subgrains are still left to some extent in Grade 92, MJP and MJT, and the finely dispersed MX particles in MGC and RHQ are mostly consumed and converted to the Z-phase under the conditions of *Gr.IIIa*, and the amount of fine MX particles in MgC, RhA, and RHT are less from the beginning. Therefore, high value of N_{av} is not recommended to improve the long-term creep strength of 9–12 Cr heat-resistant steel.

Figure 22 shows the correlations of PSs, the $\sigma_{0.5}$ s for 3 h in *Gr.I*, and the rupture strengths (σ_{tr}) for 1E5 h in *Gr.IIIa* at 600 °C with hardness number, HRC, for Grades 91, 92, and 122. The presentation method of Figure 22 is the same as that of Figure 21, except for the horizontal axis. It is reconfirmed that the harmful effect of less initial ρ_{MXi} on the PSs and $\sigma_{0.5}$ s at 600 °C is clear in Figure 22. A negative correlation is clear between initial hardness and σ_{tr} for 1E5 h in *Gr.IIIa*. However, the initial hardness can never continue to be affected for such a long duration of time of 1E5 h at 600 °C. Therefore, this is an apparent phenomenon in which high basic strength of martensite as shown in Figure 18, which increases the hardness, promotes the precipitation of the Laves phase and subsequent coarsening of the Laves phase, which triggers HRHD and decreases long-term rupture in *Gr.IIIa* (Tamura and Abe, 2021b). However, it is desirable to lower the initial hardness.

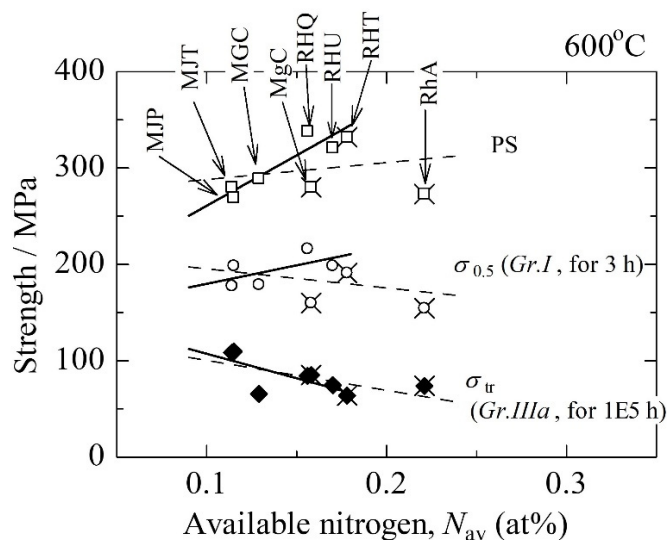


Figure 21. PS, $\sigma_{0.5}$ of *Gr.I* for 3 h, and $\sigma_{0.5}$ of *Gr.IIIa* for 1E5 h at 600 °C as functions of N_{av} for all steels investigated. Cross marks indicate steels with less ρ_{MXi} . Dashed regression lines are for all data, and solid lines are for all data without less initial MX inside the subgrains data

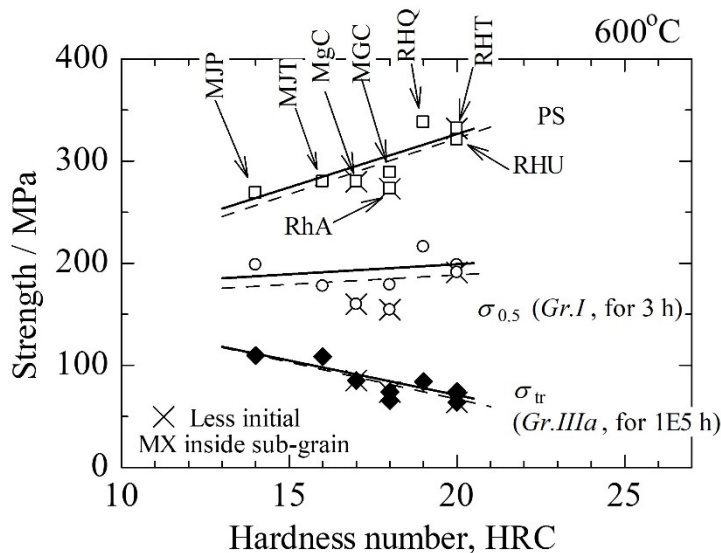


Figure 22. PS, $\sigma_{0.5}$ for 3 h in *Gr.I*, and σ_{tr} for 1E5 h in *Gr.IIIa* at 600 °C as functions of hardness number in HRC for all steels investigated. Dashed regression lines are for all data, and solid lines are for all data without data of less initial MX inside subgrains

Figure 23 shows the correlations of PSs, $\sigma_{0.5}$ s of *Gr.I* for 3 h and $\epsilon = 0.5\%$, σ_{1s} of *Gr.II* for 1000 h and $\epsilon = 1\%$, and σ_{tr} s of *Gr.IIIa* for 1E5 h at 600 °C with PAGSn for Grades 91, 92, and 122. Dashed regression lines are for all data, and solid lines are for all data without less initial MX inside the subgrains data. The *Gr.II*s for all the steels indicated are regions where Laves-phase hardening occurs. The harmful effects of the less initial ρ_{MXi} on PS, $\sigma_{0.5}$, σ_1 , and σ_{tr} seem to be masked in Figure 23 as compared to Figure 22 and moreover, the slope of the regression lines become small for long-term creep conditions, namely the effect of PAGSn on creep strength seems to be diminished for σ_{tr} s of *Gr.IIIa* for 1E5 h at 600 °C. However, when we talk about Grade 122, clear initial PAGSn

dependence on the σ_{tr} of *Gr.IIIa* is confirmed in Figure 23 (long dashed and short dashed regression line). The initial PAGBs may not move easily, excluding in a largely deformed portion with necking. Therefore, it is not so strange that the initial PAGSn shows an impact on the σ_{tr} s of *Gr.IIIa* for a long duration of time of 1E5 h at 600 °C. Therefore, coarse austenite grains are desirable to improve the long-term rupture strength as long as basic properties such as toughness are not impaired.

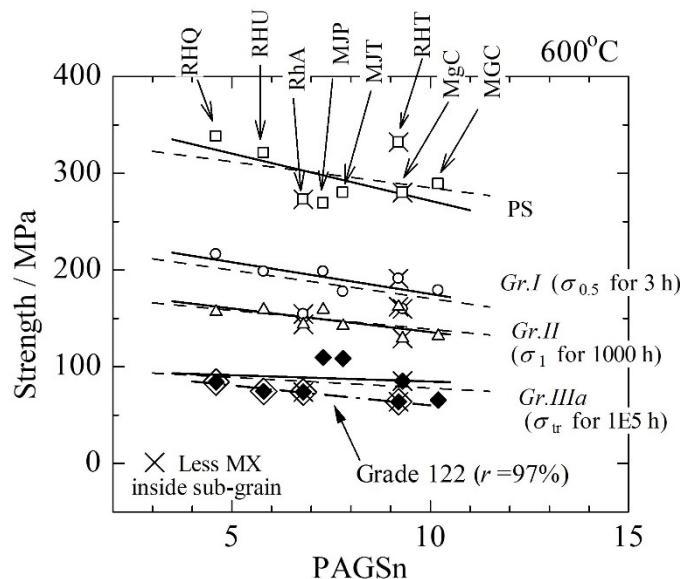


Figure 23. PS, $\sigma_{0.5}$ of *Gr.I* for 3 h and $\varepsilon = 0.5\%$, σ_1 of *Gr.II* for 1000 h and $\varepsilon = 1\%$, and σ_{tr} of *Gr.IIIa* for 1E5 h at 600 °C as functions of PAGSn. Dashed regression lines are for all data and solid lines are for all data without data of less initial MX inside the subgrains. A long dashed and short dashed line at the bottom is a regression line for only Grade 122

5.5 Degradation in Rupture Strength for *Gr.IIIa* of Grade 122 Steel

The degradation in the rupture strength for *Gr.IIIa* of T122/RHU was most noticeable at 600 °C as shown in Figure 1. This degradation behavior is compared with those of T91/MGC and T92/MJT, and the results are shown in Figure 24. The results for the 9Cr-1W and 9Cr-4W steels (Tamura & Abe, 2021a) are also shown in Figure 24. Regression lines for *Gr.I*, *II*, *III*, *IIIa*, and *IIIb* of the high-strength steels are shown in Figure 24; however, for 1W and 4W, the neighboring data points are connected by a straight line. The rupture strength of the high-strength steels degrades at 600 °C according to the following steps; initial microstructures dependency (*Gr.I*), Laves phase strengthening (*Gr.II*), coarsening of the Laves phase particles and recovery (*Gr.III*), and consumption of MX particles owing to the formation of Z-phase (*Gr.IIIa*), and as a final step, mitigation of the degrading rate in strength (*Gr.IIIb*) the details of which will be explained in Section 5.8.

It is well accepted by many researchers (Sawada et al., 2006; Danielsen, 2007; Yan, Wang, Shan, & Yang, 2013; Di-Gianfrancesco, Vipraio, & Venditti, 2013; Sawada & Kimura, 2019) that the unexpected drop in rupture strength of high-strength martensitic steel is caused by the formation of a Z-phase, which consumes a potent strengthening factor of MX particles. This fact can be also confirmed by comparing the rupture strengths of 1W, T91/MGC, and T122/RHU in Figure 24. Namely, the long-term rupture strengths of MGC and RHU (e.g., for 1E5 h) approach the extrapolated value for the same duration of 1W steel, which is martensitic steel without MX particles, although the differences in Mo and/or W content and martensite structure itself are discussed precisely to explain the difference in strength between high-strength steel and 1W steel.

The short-term rupture strength of the 4W steel is the same as that of the MGC. It is difficult to discuss this occasional coincidence because the amounts of MX particles and the Laves phase in the two steels are essentially different.

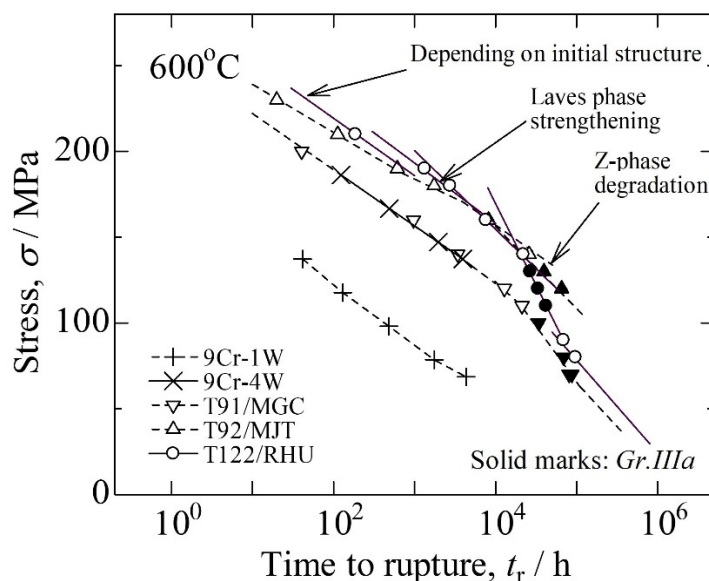


Figure 24. Comparison among the $\sigma - t_r$ relationships at 600 °C of T122/RHU, T92/MJT, T91/MGC, 9Cr-1W, and 9Cr-4W

Figure 24 clearly shows that the rupture strength of T122/RHU is slightly higher than that of T92/MJT under the test conditions for the initial microstructure dependency and Laves phase hardening (*Gr.I* and *II*), but the strength of T122/RHU drastically decreased in *Gr.IIIa* and finally approached that of T91/MGC. It is also found in Figure 24 that under the lower stresses (*Gr.IIIb*) than those for *Gr.IIIa* the degradation rate in rupture strength is mitigated and the similar phenomena are also confirmed at 600 °C in Figures A1–A3 for the other steels of Grade 122. However, Grade 92 data corresponding to *Gr.IIIb* have not yet been reported at 600 °C because the longest rupture life of T92/MJT belongs to *Gr.IIIa*. However, at temperatures higher than 600 °C, there are other data groups (*Gr.IV*) for P92/MJP and T92/MJT, where the degradation rate ($\Delta\sigma/\Delta\log t_r$) is slower than that for each *Gr.IIIa* (Tamura & Abe, 2021b). Therefore, the degradation rate in strength at 600 °C may decrease at lower stresses than that for *Gr.IIIa*, although the degradation rate itself in *Gr.IIIa* is not large.

The decrease in rupture strength was clear for *Gr.IIIa* of T122/RHU, as shown in Figure 24. Therefore, first to investigate the relationship between this fact and metallurgical reactions, t_ϵ and t_r for *Gr.III* and *IIIa* under the conditions of the average temperature and stress of *Gr.IIIa* were calculated (these variables are symbolized as t_{III} and t_{IIIa} , respectively), $[Q]$, $[V]$, and C were calculated according to Equation 2, and the differences between the obtained values of $[Q]$, $[V]$, and C for *Gr.III* and *IIIa* ($\Delta[Q]$, $\Delta[V]$, and ΔC) were also calculated. The results for each strain are listed in Table 6. In the table, the differences between logarithmic t_{IIIa} and t_{III} , i.e., $\log(t_{IIIa}/t_{III})$ are also shown. In Table 6, the values of $-\Delta[V]$ and $-\Delta C$ are listed so that the summation of each column becomes $\log(t_{IIIa}/t_{III})$ and moreover, the determinant terms for $\log(t_{IIIa}/t_{III})$ are bold-italicized (This method is named as the $\Delta[QVC]$ analysis, hereinafter).

It is found from Table 6 that the key factor lowering the rupture strength in *Gr.IIIa* is the decrease in $\Delta[Q]$. The V for *Gr.IIIa* is smaller than that for *Gr.III* (Figure 4) and thus the HRHD occurs severely in *Gr.IIIa* as compared to *Gr.III*, but the decrease in $[V]$ is not the determinant term for $\log(t_{IIIa}/t_{III}) < 0$, rather the significant occurrence of HRHD causes the severe decomposition of microstructure, which leads to the decrease in $\Delta[Q]$ in *Gr.IIIa*. Therefore, the decrease in $\Delta[Q]$ at rupture becomes the determinant term for $\log(t_{IIIa}/t_{III}) < 0$.

Table 6. Differences between *QVC* terms for *Gr.III* and *IIIa* at an indicated strain of T122/RHU steel and the calculated t_{III} and t_{IIIa} at the average temperature (600 °C) and stress (126 MPa) for *Gr.IIIa*. Determining term(s) for $\log(t_{IIIa}/t_{III})$ is (are) shown in bold-italics

| Strain (%) | 0.5 | 1 | 2 | 5 | t_r |
|--------------------------|-------------|--------------|---------------|---------------|---------------|
| $\Delta[Q]$ | -8.60 | -18.35 | -22.67 | -13.89 | -13.50 |
| $-\Delta[V]$ | -0.41 | 1.01 | 2.49 | 1.47 | 1.42 |
| $-\Delta C$ | 9.14 | 17.47 | 19.88 | 12.24 | 11.91 |
| $\log(t_{IIIa}/t_{III})$ | 0.13 | 0.12 | -0.30 | -0.18 | -0.16 |

Table 6 also shows that this situation at rupture started from a 2% strain in the accelerating creep stage. On the contrarily, Table 6 shows that in transient creep, $\varepsilon = 0.5 - 1\%$, the strength for *Gr.IIIa* is larger than that for *Gr.III*, $\log(t_{IIIa}/t_{III}) > 0$. This is because the HRHD and thus recovery surely begins to start from $\varepsilon = 0.5\%$ according to the decrease in V with increasing strain as shown in Figure 4 and at that time, though the Q for *Gr.IIIa* decreases more largely than that for *Gr.III* ($\Delta[Q] < 0$), the decrease in ΔC is still larger than the decrease in $\Delta[Q]$ for $\varepsilon = 0.5 - 1\%$. The large decrease in ΔC for $\varepsilon = 0.5 - 1\%$ means that the decrease in the entropy term in C (Equation 7) according to the proceeding of recovery for $\varepsilon = 0.5 - 1\%$ is still large as compared to the decrease in Q .

Figure 24 shows that the rupture strength for *Gr.IIIa* of T122/RHU seems to decrease abruptly compared to that of T92/MJT. To investigate the cause of this phenomenon the $\Delta[QVC]$ analysis similar to the results shown in Table 6 was performed on the rupture data for each *Gr.IIIa* of T122/RHU and T92/MJT. The results are presented in Table 7. The calculations were performed made under the conditions of average temperature and stress for *Gr.IIIa* of T122/RHU. There is little difference in time parameters, t_{T122} and t_{T92} , at $\varepsilon = 0.5\%$, but the t_{T122} s are approximately 63% of t_{T92} s from 1% strain to rupture, though the determinant terms for $t_{T122} < t_{T92}$ are not the same from 1% strain to rupture. First, the HRHD is easily occur in T122/RHU as compared to T91/MJT because $[V]_{T122} < [V]_{T92}$ throughout the entire strain range. At 1% strain, significant hardening should occur in RHU, i.e., $[Q]_{T122} > [Q]_{T92}$, but the entropy term in Equation 7 relating to this hardening perhaps further increases and thus $t_{T122} < t_{T92}$. On the other hand, in accelerating creep ($\varepsilon \geq 2\%$) recovery in an HRHD zone of T122/RHU, especially at 5% strain, is the determinant term for the degradation in strength. Therefore, HRHD easily occurs in T122/RHU, and the related recovery in an HRHD zone is accelerated severely, which is the reason for the marked decrease in rupture strength for *Gr.IIIa* of T122/RHU as compared to that of T92/MJT, as shown in Figure 24.

Table 7. Differences between *QVC* terms for each *Gr.IIIa* of T122/RHU and T92/MJT at an indicated strain at the average temperature (600 °C) and stress (126 MPa) for *Gr.IIIa* of T122/RHU. Determining term(s) for $\log(t_{T122}/t_{T92})$ is (are) shown in bold-italics

| Strain (%) | 0.5 | 1 | 2 | 5 | t_r |
|--------------------------|--------------|--------------|--------------|--------------|--------------|
| $\Delta[Q]$ | -3.10 | 3.09 | -0.06 | -5.64 | -0.88 |
| $-\Delta[V]$ | 1.51 | 0.08 | 1.31 | 1.49 | 1.31 |
| $-\Delta C$ | 1.57 | -3.38 | -1.41 | 3.91 | -0.60 |
| $\log(t_{T122}/t_{T92})$ | -0.031 | -0.20 | -0.16 | -0.24 | -0.18 |

5.6 Degradation in Creep Strength on the Way to Rupture for *Gr.IIIa* of T122/RHU

5.6.1 Variations of *QVC* in *Gr.IIIa*

Degradation in rupture strength at 600 °C of T122/RHU was most severe in *Gr.IIIa* as compared to T91/MGC and T92/MJT (Figure 24). A control factor for this is a large decrease in Q at a strain range of 1–2% as shown in Figure 4 and Table 6. To make this much clear, Figure 25 shows the Q s for *Gr.IIIa* of MGC, MJT, and RHU as functions of strain. In the figure, the Q s for the most long-term data group, *Gr.III*, of 1W and 4W are also plotted. A gradual increase in Q of 1W is caused by the operation of the SBS and DFRP of $M_{23}C_6$ (Tamura & Abe, 2021a). In the case of 4W, the Laves phase hardening is added to the SBS and DFRP, which causes a rapid

increase in Q , but after the Q peaks, the Q decreases rapidly to a level of those of 1W owing to the coarsening of the Laves phase. These phenomena are easily accepted in the metallurgical common sense.

The Q s for the high-strength steels shown in Figure 25 are large from the beginning of creep due to the SBS, DFRP, and Laves phase hardening, but the Q s decrease with an increase in strain owing to the coarsening of the Laves phase. Furthermore, the formation of the Z-phase for $\varepsilon \geq 0.5\%$ accelerates the decrease in Q . However, it is difficult to interpret that the Q s for the high-strength steels shown in Figure 25 are smaller in a wide strain range than those for 1W, where both the Laves phase and Z-phase are not formed. This clearly indicates that destructive microstructural changes that cannot occur during the creep of plain 9Cr-1W steel occur in the high-strength martensitic steels investigated.

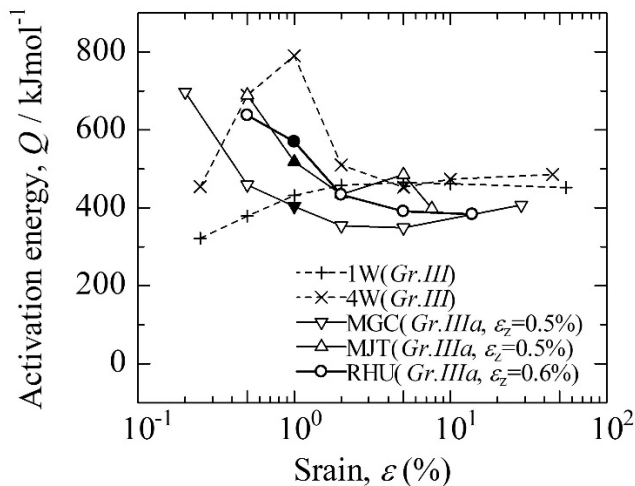


Figure 25. Activation energy, Q , as functions of strain for *Gr.s.IIIa* of MGC, MJT, and RHU and for *Gr.s.III* of 1W and 4W. ε_z is a start strain for the Z-phase formation

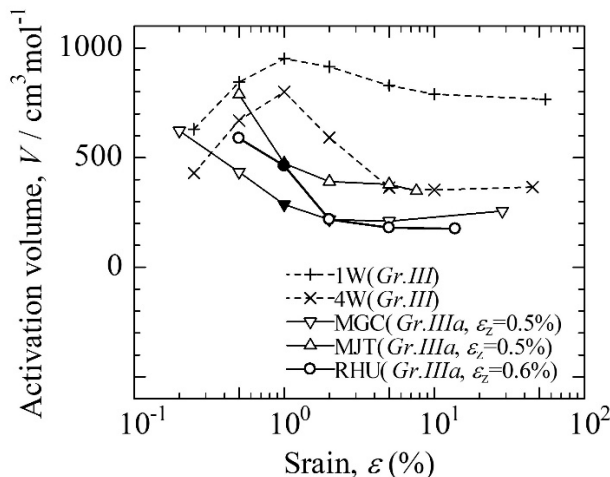


Figure 26. Activation volume, V , as functions of strain for *Gr.s.IIIa* of MGC, MJT, and RHU and for *Gr.s.III* of 1W and 4W. ε_z is a start strain for the Z-phase formation

Figure 26 shows the V s for *Gr.s.IIIa* of MGC, MJT, and RHU and *Gr.s.III* of 1W and 4W as functions of strain. It is noticed that a decrease in V of RHU is extremely large between $\varepsilon = 1 - 2\%$ and the values of V show minimum among the steels investigated during $\varepsilon \geq 2\%$. The HRHD must start in RHU for $\varepsilon = 1 - 2\%$ more significantly or frequently than that of MJT. In an HRHD zone, deformation is concentrated owing to stress concentration, which leads to severe decomposition of the microstructure. During this strain range C is also

decreases as shown in Figure A13 which is caused by the decrease in the entropy term of Equation 7 due to the severe recovery occurred in an HRHD zone. This situation of RHU continues until rupture, and thus, the rupture strength for *Gr.IIIa* of RHU is significantly lower than that of the MJT. HRHD is an essential deformation mode of martensitic steel (Tamura & Abe, 2021a; 2021b). That the values of V in accelerating creep are minimum indicates that the microstructure of RHU has characteristics which cause easily or frequently occurring of HRHD among the steels shown in Figures 25 and 26.

5.6.2 Beginning of the Degradation in Strength of RHU

Significant degradation in the rupture strength of RHU occurred in *Gr.IIIa* as shown in Figures 1 and 24. At 600 °C this degradation begins from $\varepsilon=1\%$ for approximately 1.1E4 h as shown in Figure 3. Figure 27 shows the relationships between t_1 and σ for T91/MGC, T92/MJT, and T122/RHU at 600 °C. The data points of MGC and MJT are connected by dashed and solid lines, respectively, in Figure 27; however, the regression lines for each data group are drawn for RHU (Figure 3). Data points for each *Gr.IIIa*, where the slope $\Delta\sigma/\Delta\log t$ is most steep, are distinguished by solid marks in the figure. It is confirmed from Figure 27 that the σ_1 s for *Gr.IIIa* of RHU are clearly lower than those of MJT and the σ_1 s for *Gr.III* of RHU are comparable to those of MJT, though the σ_1 s for *Gr.I* and *Gr.II* of RHU are higher than those of MJT. Therefore, the degradation in σ_1 for *Gr.IIIa* of RHU seems to already begin from the test conditions of *Gr.III*, an earlier time region than *Gr.IIIa*.

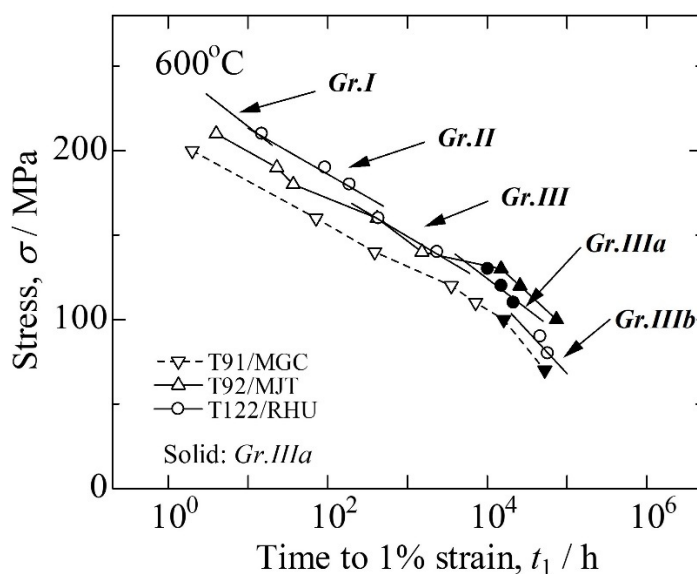


Figure 27. Comparison between the $\sigma - t_1$ relationships at 600 °C of T91/MGC, T92/MJT, and T122/RHU

Therefore, first the $\Delta[QVC]$ analyses on the time parameter t_ε and t_r were made for *Gr.III* to *IIIa* of T122/RHU and the results are shown in Table 8. These factorial analyses were conducted near the cross point of the regression lines for *Gr.III* and *IIIa* shown in Figure 27 of T122/RHU (600 °C, 105 MPa). The analysis method is the same as that in Table 5, but the calculation was performed at a lower stress than that in Table 5; thus, different results were obtained. Table 8 shows that the determinant factor for decreasing the time parameter $\log(t_{IIIa}/t_{III})$ is $\Delta[Q] < 0$ for $\varepsilon \geq 1\%$. However, it is also pointed out that the $\Delta[V]$ term changes from $V_{IIIa} > V_{III}$ to $V_{IIIa} < V_{III}$ between $\varepsilon = 0.5 - 1\%$ in transient creep. This indicates that HRHD begins to occur more significantly in *Gr.IIIa* between $\varepsilon = 0.5 - 1\%$ in transient creep as compared to *Gr.III*. In an HRHD zone ρ_{MXI} decreases owing to the formation of the Z-phase assisted by strain concentration, which leads to decreases in Q for *Gr.IIIa* or $\Delta[Q] < 0$ for $\varepsilon \geq 1\%$.

Table 8. Differences in QVC for t_ε and t_r of *Gr.III* and *IIIa* at an indicated strain of T122/RHU steel and the calculated t_{III} and t_{IIIa} at 600 °C and 105 MPa. Determining term(s) for $\log(t_{IIIa}/t_{III})$ is (are) shown in bold-italics. The MCR point is at approximately 1% strain

| Strain (%) | 0.5 | 1 | 2 | 5 | t_r |
|--------------------------|-------------|---------------|---------------|---------------|---------------|
| $\Delta[Q]$ | -8.60 | -18.35 | -22.67 | -13.89 | -13.50 |
| $-\Delta[V]$ | -0.34 | 0.84 | 2.08 | 1.22 | 1.18 |
| $-\Delta C$ | 9.14 | 17.47 | 19.88 | 12.24 | 11.91 |
| $\log(t_{IIIa}/t_{III})$ | 0.42 | -0.04 | -0.72 | -0.43 | -0.40 |

5.6.3 Origin of the Degradation in Strength for *Gr.IIIa* of RHU

In the previous section, it is clarified that a sign of the unexpected drop in long-term rupture strength observed in *Gr.IIIa* of RHU (Figure 24) is already revealed at $\varepsilon = 1\%$ (Figure 27) and that this degradation in σ_1 for *Gr.IIIa* is related to the degradation in σ_1 for *Gr.III* (Table 8). However, when Figure 27 is compared carefully with Figure 24, it is noticed anew that the creep strength for *Gr.III* of RHU decreases largely at $\varepsilon = 1\%$ compared with that for *Gr.II*, where the Laves phase hardening certainly takes place. Therefore, the $\Delta[QVC]$ analyses were made for t_ε and t_r of *Gr.II* and *III* of RHU near the cross point of the regression lines for *Gr.II* and *III* shown in Figure 27 of T122/ RHU (600 °C, 170 MPa) and the results are shown in Table 9. It is found from Table 9 that the determinant of $t_{III} < t_{II}$ for $\varepsilon \geq 1\%$ is $Q_{III} < Q_{II}$ or $0 < \Delta[Q]$ and with that, $V_{III} < V_{II}$ for $\varepsilon \geq 1\%$. Namely, the decrease in V for $\varepsilon \geq 1\%$ of *Gr.III* corresponds to the frequent occurrence of HRHD which promotes the decomposition of microstructure inside an HRHD zone and thus $t_{III} < t_{II}$. Table 9 also shows that the difference in Q for $\varepsilon \geq 2\%$ between *Gr.II* and *III* decreases with increasing strain and finally $t_{II} \sim t_{III}$ as seen in Figure 1. This indicates that the Laves phase hardening is weakened in accelerating creep of *Gr.II* owing to the coarsening of the Laves phase particles because a strengthening factor does not operate in *Gr.III*.

Table 9. Differences in QVC for t_ε and t_r of *Gr.II* and *III* at an indicated strain of T122/RHU steel and the calculated t_{II} and t_{III} at 600 °C and 170 MPa. Determining term(s) for $\log(t_{III}/t_{II})$ is (are) shown in bold-italics. The MCR point is at approximately 2% strain

| Strain (%) | 0.5 | 1 | 2 | 5 | t_r |
|------------------------|-------------|--------------|--------------|--------------|-------|
| $\Delta[Q]$ | 1.48 | -1.39 | -8.66 | -7.88 | -5.77 |
| $-\Delta[V]$ | -0.43 | 0.19 | 1.22 | 1.34 | 1.13 |
| $-\Delta C$ | -0.46 | 0.86 | 7.24 | 6.54 | 4.64 |
| $\log(t_{III}/t_{II})$ | 0.59 | -0.34 | -0.13 | -0.01 | 0.00 |

Therefore, in order to compare the creep behavior of T122/RHU with that of T92/MJT in which the Laves phase hardening is continued until rupture (Tamura & Abe, 2021b), the differences in the Q s for RHU and MJT, $Q_{RHU} - Q_{MJT}$, are plotted as functions of strain in Figure 28. Similarly, the differences in V s for RHU and MJT, $V_{RHU} - V_{MJT}$, are shown as functions of strain in Figure 29. It is found from Figures 28 and 29 that $Q_{RHU} \sim Q_{MJT}$, but $V_{RHU} < V_{MJT}$ for all data groups except for *Gr.II* throughout the entire strain range and in addition that Q and V are especially small for *Gr.II* throughout the entire strain range except for $\varepsilon \sim \varepsilon_{MCR} = 2\%$. These results indicate that RHU is easy to deform heterogeneously as compared to MJT regardless of creep strain and data groups or test conditions, i.e., test temperature and stress because $V_{RHU} < V_{MJT}$ (see also Figure 12). Therefore, the smaller values of Q and V for *Gr.II* of RHU shown in Figures 28 and 29 must be responsible for the large drops in rupture strength in *Gr.IIIa* of RHU shown in Figure 24.

Laves-phase hardening occurred in *Gr.II* of Grade 92 (Tamura & Abe, 2021b). Laves-phase hardening was also confirmed in *Gr.II* of RHU as shown in Figure 3; however, the above results deduced from Figures 28 and 29 indicate that the precipitation and coarsening behavior of the Laves phase in the RHU are largely different from those of the MJT. Therefore, the $\Delta[QVC]$ analyses on the t_ε and t_r for *Gr.I* and *II* of MJT and RHU were made, and the results are shown in Tables 10 and 11, respectively. The calculation stresses shown in Tables 10 and 11 for MJT and RHU, respectively, are selected near the cross point of the regression lines at 600 °C for *Gr.I* and *II* shown in $\sigma - t_r$ diagrams for each (see Figure 3 & the related figure in Tamura & Abe, 2021b for MJT).

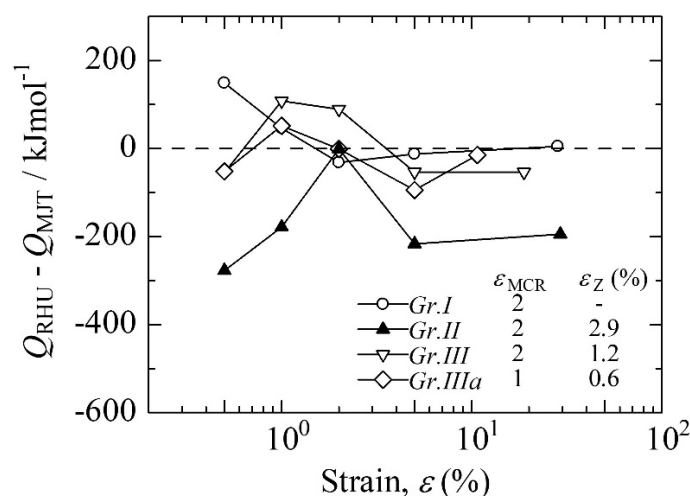


Figure 28. Difference in Q for MJT and RHU as functions of strain. ε_{MCR} and ε_Z are a strain for an MCR point and a start strain for the Z-phase formation, respectively.

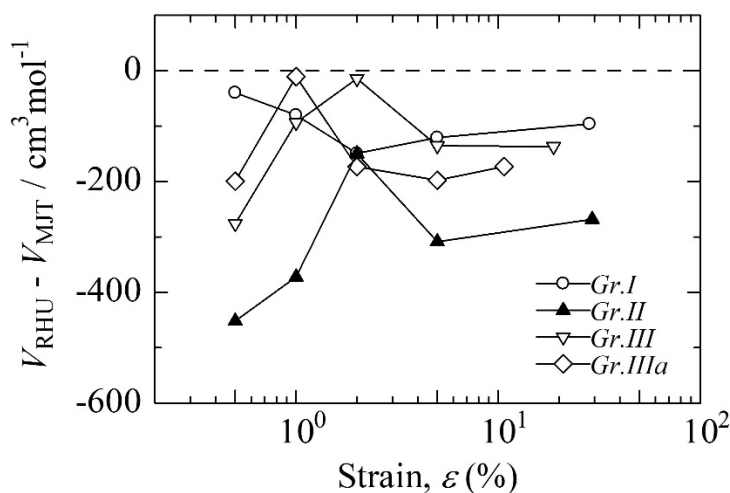


Figure 29. Difference in V for MJT and RHU as functions of strain

Concerning *Gr.II* of MJT, the previous work (Tamura & Abe, 2022b) reported that hardening owing to the SBSD, DFRP of $M_{23}C_6$, and the precipitation of the Laves phase occurs when $\varepsilon \leq 1\%$ and that although HRHD and recovery owing to the coarsening of the Laves phase occur when $\varepsilon > 1\%$, the Q maintains still a high level. Therefore, the determinant term for $\log(t_{II}/t_I) > 0$ is $\Delta[Q]$ in $\varepsilon > 1\%$ as shown in Table 10 and the Laves phase strengthening at 600 °C is confirmed up to rupture in *Gr.II* of MJT (Tamura & Abe, 2021b). Whereas, in *Gr.II* of RHU the Laves phase hardening at 600 °C becomes unclear at rupture as seen in Figure 1, though the Q for *Gr.II* increases up to $\varepsilon = 2\%$ as seen in Figure 4 and consequently the Laves-phase strengthening at 600 °C is clearly confirmed in 1% strain as seen in Figure 3.

Table 10. Differences in QVC for t_ε and t_r of $Gr.I$ and II at an indicated strain of T92/MJT steel and the calculated t_I and t_{II} at 600 °C and 170 MPa. Determining term(s) for $\log(t_{II}/t_I)$ is (are) shown in bold-italics. The MCR point is at approximately 2% strain

| Strain (%) | 0.5 | 1 | 2 | 5 | t_r |
|--------------------|---------------|--------------|-------------|-------------|-------------|
| $\Delta[Q]$ | 20.85 | 17.89 | 6.25 | 6.97 | 5.00 |
| $-\Delta[V]$ | -4.59 | -4.62 | -2.06 | -1.91 | -1.51 |
| $-\Delta C$ | -16.30 | -13.07 | -4.06 | -4.88 | -3.33 |
| $\log(t_{II}/t_I)$ | -0.04 | 0.20 | 0.13 | 0.17 | 0.16 |

In response to this, Table 11 indicates that when $\varepsilon = 1 - 2\%$, $\Delta[Q]$ is the determinant term for $\log(t_{II}/t_I) > 0$, but the determinant term for $\log(t_{II}/t_I) > 0$ changes to a decrease in ΔC or $\Delta[V] + \Delta C$ in a higher strain range $\varepsilon > 5\%$ because of $Q_{II} < Q_I$ as seen in Figure 4. This indicates that HRHD becomes noticeable when $\varepsilon > 5\%$ because the coarsening of the Laves phase particles causes the generation of a HRHD zone, and the subsequent decomposition of microstructure is promoted. The initiation conditions of the formation of the Z-phase in $Gr.II$ of RHU are $\varepsilon_Z = 2.9\%$ and $t_Z = 880$ h at 600 °C (Table 2). The formation of the Z-phase in $Gr.II$ is possibly and additionally responsible for the decrease in $\Delta[Q]$ in $\varepsilon > 5\%$. However, it is exactly a problem in Tables 10 and 11 that the $\Delta[Q]$ s for RHU are generally smaller than those for MJT which means that the laves phase hardening is insufficient in $Gr.II$ of RHU as compared to MJT.

Table 11. Differences in QVC for t_ε and t_r of $Gr.I$ and II at an indicated strain of T122/RHU steel and the calculated t_I and t_{II} at 600 °C and 200 MPa. Determining term(s) for $\log(t_{II}/t_I)$ is (are) shown in bold-italics. The MCR point is at approximately 2% strain.

| Strain (%) | 0.5 | 1 | 2 | 5 | t_r |
|--------------------|--------------|-------------|-------------|-------------|-------------|
| $\Delta[Q]$ | -4.69 | 4.43 | 8.10 | -5.27 | -6.97 |
| $-\Delta[V]$ | -0.46 | -1.93 | -2.42 | 0.00 | 0.29 |
| $-\Delta C$ | 4.54 | -2.40 | -5.58 | 5.52 | 6.90 |
| $\log(t_{II}/t_I)$ | -0.61 | 0.10 | 0.11 | 0.26 | 0.22 |

In $Gr.IIIa$ of RHU, Laves phase hardening is not confirmed at rupture (Figures 1 and 4); rather, the Z-phase is contrarily observed from the beginning of creep (Table 2). Therefore, martensitic steel with 11–12% Cr like RHU has been interpreted as easy degrading in strength, because the MX particles are easily consumed by the faster formation of the Z-phase as compared to 9Cr steel like MJT (Sawada et al., 2007). However, it is clear from the above discussion that the ease in the occurrence of HRHD caused by the easy coarsening of the Laves phase particles in RHU as compared to MJT triggers early degradation in $Gr.IIIa$ of RHU.

5.7 Root Cause of the Degradation in Creep Strength of High-Cr Martensitic Steel

5.7.1 Virtual Creep Curve for $Gr.IIIa$

Creep behaviors are usually observed measuring strain as a function of time at a constant temperature and load. And the relationships between t and $\varepsilon(\dot{\varepsilon})$ at a constant T and σ or between $t(\dot{\varepsilon})$ and σ at a constant T and ε or at rupture have been accumulated and studied to investigate the creep behavior of material. However, the relationships between σ and ε at a constant T and for a specific t_ε (t_r) have not been studied. This is because the creep strength cannot be expressed analytically as a function of temperature and a specific time duration so long as a double logarithmic relationship between σ and t_ε (t_r) is conventionally used. However, if Equation 1 is used, the $\sigma - \varepsilon$ relationship like a result of a tensile test can be obtained at a specific T and for a specific t_ε and t_r .

To investigate the root cause of the degradation in the long-term rupture strength of 11–12% Cr, the virtual creep curves for $Gr.IIIa$ of Grades 91, 92, and 122 at 600 °C for 1E5 h are calculated and the results are shown in Figure 30. The average strength, σ_ε , can be calculated at 600 °C for 1E5 h using the QVC s calculated from t_ε and t_r using Equation 1 for each specific steel and strain shown in Figures 4 and A1–A3 for Grade 122 and in the previous work (Tamura & Abe, 2021b; Tamura, 2022) without using any adjustable parameters. Concerning

Gr.IIIa of MgC, the *QVC* are obtained only at rupture or a sufficient number of data for *Gr.IIIa* is not shown in the data sheet (NIMS, 2014).

Figure 31 schematically illustrates the symbolic creep curves for each steel grade. The working states of the strengthening mechanisms at rupture are indicated on the right-hand margin in the figure, and the related metallurgical reactions during creep are indicated at the bottom. The MCR points for all steels investigated are at approximately $\epsilon = 1\%$. Although the MCR for *Gr.IIIa* of RhA occurs at $\epsilon = 2\%$ as shown in Figure A8, the value of MRC at $\epsilon = 1\%$ is almost same as that for $\epsilon = 2\%$.

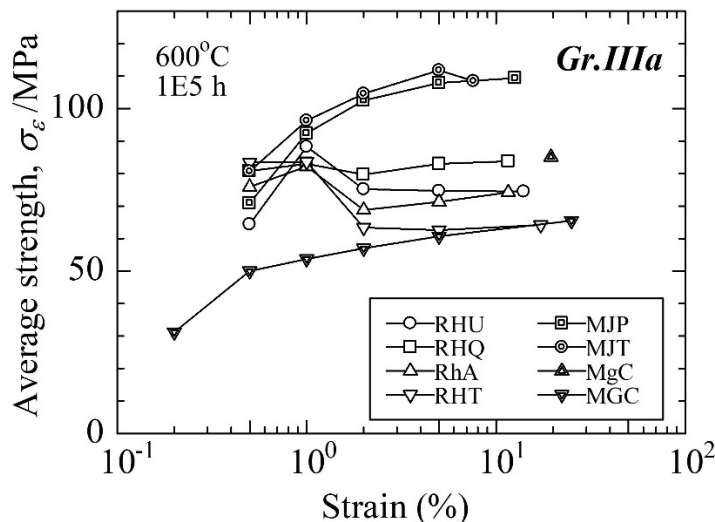


Figure 30. Virtual creep curves for *Gr. IIIa* of Grades 91,92, and 122. Average creep strengths are calculated at 600 °C for 1E5 h using *QVC*s for each strain and steel listed

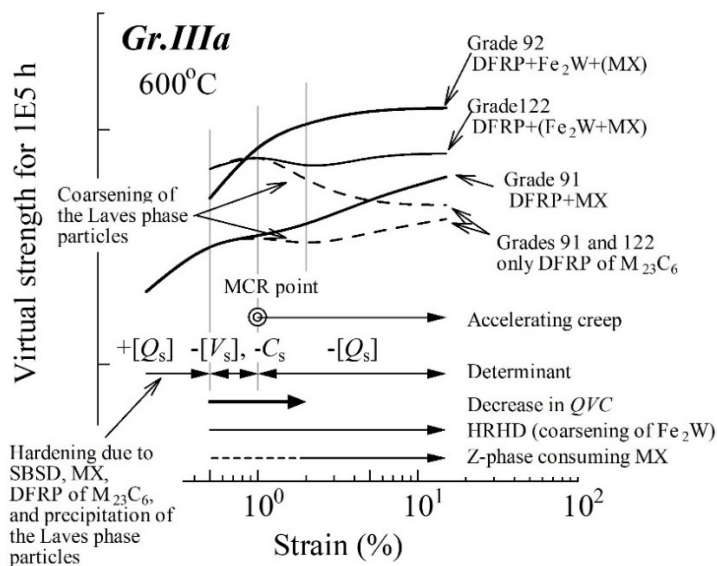


Figure 31. Schematic creep curves for 1E5 h of typical steel types with different strengthening mechanism(s) and related metallurgical information. HRHD is caused by coarsening of the Laves phase

Rapid decreases in *QVC* for *Gr.IIIa* of all steels investigated are confirmed in a strain range of 0.5 – 2% as shown in Figure 32. Therefore, HRHD should occur for all steels investigated at approximately $\epsilon > 0.5\%$ taking into account of the low values of *V*. Z-phase begins to form at approximately $\epsilon = 0.5\%$ referring to Table 2 and

the previous work (Sawada et al., 2007; Tamura & Abe, 2021b; Tamura, 2022). These situations are shown at the bottom of Figure 31.

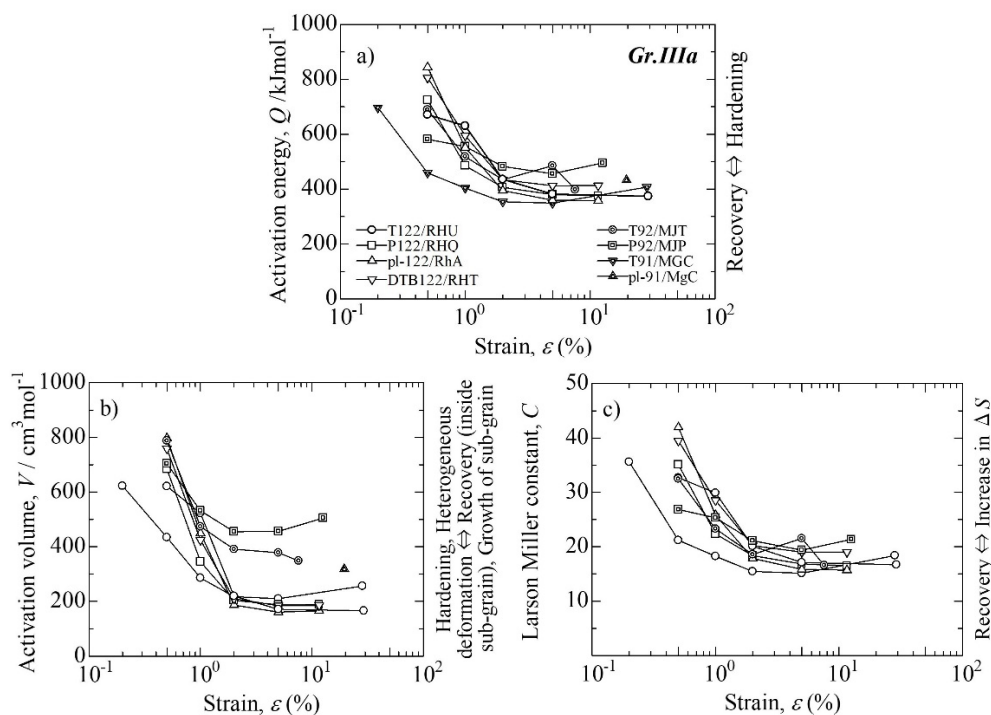


Figure 32. QVCs for *Gr.IIIa* as functions of strain for Grades 91, 92, and 122

5.7.2 Interpretation of Virtual Creep Curves for Grade 91

The calculated temperature for Figure 30 at 600 °C is higher than the nose temperature of the TTP curve for the Laves phase of Fe_2Mo , which is approximately 575 °C (Tamura et al., 1988). Therefore, the Laves phase particles in MGC are estimated to be easily coarsened to approximately 2 μm at 600 °C for 1E5 h (Tamura et al., 2021b) and thus, the precipitation hardening by the Fe_2Mo becomes negligibly small at rupture in *Gr.IIIa* of Grade 91. An important strengthening factor of MX is also disappeared at rupture in *Gr.IIIa* of MGC, because the ρ_{MX} at rupture of MGC tested at 600 °C and 70 MPa (*Gr.IIIa*, $t_r = 80\,736.8$ h) decreases down to 5.3% of the initial value and consequently the most of the finely dispersed MX particles inside subgrains are converted to the coarse Z-phase particles formed near the boundaries (Sawada et al., 2011). The remaining strengthening mechanism for *Gr.IIIa* of T91/MGC is tempered martensitic structure or recovered subgrain structure reinforced by the DFRP mechanism of M_{23}C_6 carbide particles. These situations coincide with the results of the TEM observations explained in Section 5.1.1 and Figure 6 (Kushima et al., 1999; Kushima et al., 2002; Kimura et al., 2004). The corresponding creep curve for T91/MGC is schematically drawn using a dashed curve at the bottom, as shown in Figure 31. Of course, solid-solution hardening always occurs at all stages of the steels investigated. Furthermore, the dragging mechanism for the solute atoms by moving dislocations and the dynamic strain aging mechanism are also active even for *Gr.IIIa* (Tamura & Abe, 2021b; Tamura, 2022), but these hardening mechanisms are omitted in Figure 31 for simplicity, because these mechanisms are common for all steels shown in Figure 30.

The σ_{tr} of pl-91/MgC at rupture and 600 °C for 1E5 h in *Gr.IIIa*, 85.1 MPa, is approximately 20 MPa higher than that for T91/MGC, 65.5 MPa, as shown in Figure 30, while these two steels are classified into the same steel grade in ASME standard, Grade 91. Sawada et al. (2014) observed that 56.2% of the initial ρ_{MX} is still remained even after rupture of MgC tested at 600 °C and 70 MPa (*Gr.IIIa*, $t_r = 78\,236.5$ h) and therefore, they conclude that the rupture strength of MgC at 600 °C for approximately 1E5 h is higher than that for MGC and that reducing Ni content is responsible for the increase in the stability of finely dispersed MX particles and consequently the increase in the long-term rupture strength at 600 °C of ASME Grade 91 steel (Ni concentration: 0.04% for MgC and 0.28% for MGC).

Panait et al. (2010) observed the microstructure of a ruptured specimen at 600 °C and 80 MPa ($t_r = 113\,431$ h) of ASME P91 steel (P91/Panait, hereinafter) employing TEM. The rupture data of P91/Panait are on an extrapolated regression line at 600 °C for *Gr.IIIa* of pl-91/MgC (Tamura, 2022). Fine and rectangular particles of MX are found inside the subgrains in the micrographs, and the equivalent circle diameter of MX in a gauge portion of a ruptured specimen is reported as approximately 30 nm (Panait et al., 2010). The ρ_{MX} is not yet investigated, but the ρ_{MX} is estimated to be approximately $1.7E12\text{ m}^{-2}$ from their micrographs. This value of ρ_{MX} for P91/Panait is between those for MgC ($\rho_{MX} = 2.4E12\text{ m}^{-2}$) and MGC ($\rho_{MX} = 4.1E11\text{ m}^{-2}$) (Sawada et al., 2014). The Ni concentrations in pl-91/MgC, P91/Panait, and T91/MGC were 0.04%, 0.11%, and 0.28%, respectively. Therefore, it is reconfirmed that reducing the Ni content in high-strength martensitic steel mitigates the consumption of finely dispersed MX particles and consequently reduces the unexpected drops in the long-term rupture strength of high-strength martensitic steel. Therefore, a schematic and virtual creep curve for Grade 91 which is strengthened by the DFRP and MX is drawn using a solid line in the third at $\varepsilon = 15\%$ from the top in Figure 31, where the creep curve of T91/MGC is traced up to 1% strain and then a solid curve is virtually estimated connecting to the rupture point for *Gr.IIIa* of pl-91/MgC.

5.7.3 Interpretation of Virtual Creep Curves for Grade 92

The creep strength for Grade 92 *Gr.IIIa* increases from the beginning of creep owing to the strengthening of sub-boundaries by the SBS, DFRP of $M_{23}C_6$, and precipitation of the Laves phase (Tamura & Abe, 2021b). Although the SBS effect is weakened with an increase in creep strain owing to the annihilation of boundary dislocations, the precipitation hardening of the Laves phase in Grade 92 holds for a long duration of time during creep of *Gr.IIIa*, because the coarsening rate of the Laves phase formed during creep at 600 °C in Grade 92 is not that large and the size of the Laves phase is estimated to be approximately 300 nm at 600 °C for 1E5 h, which is much smaller than that for Grade 91, 2 μm , (Jiang et al., 2013; Tamura & Abe, 2021b). Furthermore, the slow coarsening rate of the Laves phase at 600 °C in Grade 92 is supported by the TTP consideration; a temperature of 600 °C is far lower than a nose temperature of 650 °C in the TTP curves of the Laves phase formed in 8Cr-2W steel (Tamura et al., 1988) and 9Cr-4W steel (Abe, et al., 1991), if we can neglect the effect of Mo containing in Grade 92 on the nose temperature, though the composition of the Laves phase formed in P92 is 59.6Fe, 21.64W, 6.94Mo, and 10.38Cr in at%, respectively (Nie et al., 2014). Therefore, hardening by the Laves phase in addition to the DFRP of $M_{23}C_6$, and MX was considered to hold until rupture at 600 °C for 1E5 h in Grade 92.

The Ni concentrations in the MJP and MJT of Grade 92 were 0.17% and 0.13%, respectively. These values are comparable to that of P91/Panait and are rather low. Therefore, considerable amount of finely dispersed MX particles is expected to be remained escaping from the conversion to the Z-phase until rupture at 600 °C in Grade 92.

Therefore, high levels of creep strength are maintained until rupture at 600 °C for 1E5 h in Grade 92 even in the conditions of *Gr.IIIa* as shown in Figure 30 and thus a virtual and schematic creep curve for Grade 92 are drawn in the top of Figure 31. If the basic rupture strength at 600 °C for 1E5 h of the tempered martensitic structure or recovered subgrain structure reinforced by the DFRP of $M_{23}C_6$ carbide particles is assumed to be 60 MPa as a rounded number referring to the rupture strength of T91/MGC shown in Figure 30, and in addition, an increase in rupture strength by the retained MX particles can be assumed to be 20 MPa referring to the difference in rupture strengths between MgC and MGC shown in Figure 30, the contribution to the σ_{1E5} by the Laves phase particles on the boundaries is estimated to be approximately 20 MPa referring to the rupture strengths of Grade 92 shown in Figure 30 if we can assume that a similar level of fine MX particles to that of MgC is retained in Grade 92 at rupture. However, the size and number density of $M_{23}C_6$, the Laves phase, the Z-phase, and MX particles and TEM micrographs using the long-term rupture specimens at around 600 °C of Grade 92 are the minimum necessary to further discussion.

5.7.4 Interpretation of Virtual Creep Curves for Grade 122

The most σ_{ε} s for Grade 122 are positioned between the creep curves of T91/MGC and Grade 92 (MJT and MJP) in Figure 30. Although the σ_{ε} s at $\varepsilon = 0.5\%$ of Grade 122 are slightly larger than those of Grade 92, at $\varepsilon = 1\%$ the σ_{ε} s of Grade 122 are smaller than those of Grade 92 and furthermore, the σ_{ε} s of Grade 122 decrease largely between $\varepsilon = 1 - 2\%$ except for RHQ and then gradually increase (RHQ and RhA) or remain flat (RHU and RHT) for $\varepsilon > 2\%$ until rupture.

A gradual increase in strength in accelerating creep or $\Delta\sigma/\Delta\log t > 0$ is a general phenomenon occurred during creep of martensitic steel as seen in the cases for Grade 92 and T91/MGC (Figure 30) and even for simple steel of 9C-1W (Tamura & Abe, 2022b). This is because the DFRP mechanism for $M_{23}C_6$ is operating on the movement of sub-boundaries during recovery. Rather, it is a problem that the hardening by the DFRP is small for RHU and

RHT. However, this does not really matter as compared with that the unexpected drop in rupture strength for *Gr.IIIa* of Grade 122 is considerably larger than that for Grade 92 as seen in Figures 19 and 30.

That the σ_{ϵ} s for *Gr.IIIa* of Grade 122 are larger than those for Grade 92 at $\epsilon = 0.5\%$ in average is caused by the Laves phase hardening and the hard basic strength as explained in Section 5.3 using Figure 18. This is because the Laves phase hardening is promoted by not only straining as explained in Section 4.2.2, but also the initial high hardness of Grade 122 as compared to Grade 92 as shown in Figures 14, 18, and 19. When the initial hardness is high, more dislocations are swept out from the subgrains and thus the Laves phase particles easily nucleate on the boundaries (Yan et al., 2013), which leads to hardening. A similar phenomenon is confirmed in Figure 27, that is, the σ_1 s of T122/RHU at 600 °C are clearly larger than those of T91/MJT in *Gr.II* where the Laves phase hardening is dominant.

When $\epsilon \geq 1\%$ or during accelerating creep, the σ_{ϵ} s of Grade 122 are considerably smaller than those of Grade 92. These decreases in σ_{ϵ} are caused by both the consumption of fine MX particles owing to the formation of the Z-phase and the decrement in the Laves-phase hardening owing to the coarsening of the Laves phase. Figure 30 shows that the σ_2 s of Grade 122 are roughly the same as σ_{tr} s. This may indicate that the microstructures which have an impact on the moving dislocations are approximately the same for 2% strain and at rupture. Therefore, to solve the root causes for the rapid drops in σ_{ϵ} between $\epsilon = 1 - 2\%$ shown in Figure 30 is important to mitigate the unexpected degradation in long-term rupture strength of Grade 122 at approximately 600 °C. However, it is difficult to distinguish the coarsening of the Laves phase, the consumption of fine MX particles, or the both as the dominant cause for the rapid drops in the σ_{ϵ} s because of the lack of metallurgical information such as TEM micrographs showing the subgrain structure and the distribution of the Laves phase, MX, and $M_{23}C_6$ particles.

However, it is natural to consider that the coarsening of the Laves phase particles at an early stage of creep ($\epsilon \sim 1\%$) promotes the generation of an HRHD zone and the concentrated straining in an HRHD zone promotes the formation of Z-phase consuming MX particles and further coarsening of the Laves phase particles, because the QVC begin to decrease from $\epsilon = 0.5\%$ and thus the HRHD already begins. Figure 32 shows that V values of Grade 122 at $\epsilon = 2\%$ are less than half of those of Grade 92 or are comparable to that of T91/MGC. Therefore, the Laves phase particles of an Fe_2W type in Grade 122 crept to $\epsilon = 2\%$ at 600 °C under the *Gr.IIIa* conditions are considered to be coarsened to a level of the Laves phase particles of Fe_2Mo type in a similarly crept specimen of T91/MGC and thus, HRHD occurs near the coarse Laves particles in Grade 122 more severely and/or frequently as compared to that of Grade 92. Consequently, the values of Q of Grade 122 may be lowered to a level of MGC as shown in Figure 32a). In this case, the σ_{ϵ} at 600 °C for *Gr.IIIa* of Grade 122 approaches to the σ_{tr} for T91/MGC, which corresponds to the case of RHT shown in Figure 30 and a virtual and schematic creep curve for RHT are drawn using a dashed line in the second at $\epsilon = 15\%$ from the bottom in Figure 31. Therefore, it seems to be reasonable to consider that the vicious cycle of HRHD, the coarsening of the Laves phase, and the formation of the Z-phase by consuming MX particles occurs, even from a small nominal strain, which leads to serious degradation in strength for the *Gr.IIIa* of Grade 122, especially for RHT, at 600 °C compared to the P92/MJP.

In the case of a less decrease in σ_{ϵ} between $\epsilon = 1 - 2\%$, the σ_{1E5} s at rupture for *Gr.IIIa* of Grade 122 can hold to a certain level by both the retained fine particles of MX inside subgrains and the retaining Laves phase (Fe_2W) particles on the boundaries to be rather small. The relating virtual creep curve to this case is drawn using a solid line in the second from the top in Figure 31. This curve is drawn imaging the creep curve of RHQ shown in Figure 30. That the relatively high level of σ_{1E5} at rupture of RHQ among Grade 122 as seen in Figure 30 should be caused by the initial state of microstructure itself. Therefore, the σ_{1E5} s at rupture of other heats of Grade 122 than RHQ should be approximated to that of RHQ by controlling the initial microstructure adequately.

Furthermore, if we can suppress the coarsening of the Laves phase particles in Grade 122 more perfectly, we can not only mitigate the occurrence of the HRHD, and thus the consumption of the fine MX particles can be minimized but also expect the Laves phase hardening in Grade 122 for 1E5 h at 600 °C, which should lead to an increase in the rupture strength for *Gr.IIIa* of ASME Grade 122 to a level of Grade 92. We can expect to suppress the coarsening of the Laves phase in ASME Grade 122 much more for example by adding Re (Hashizume et al., 2009; Tamura & Abe, 2022b).

5.8 Creep Behavior in *Gr.IIIb* of T122/RHU

5.8.1 Creep Deformation

When the creep data of RHU are plotted in a double logarithmic diagram, we cannot distinguish data groups of *Gr.IIIa* and *IIIb* as shown in Figure 1 and the stress exponent of $n = 3.7$ are obtained for a data group of *Gr.IIIa* and *IIIb*. However, a data group of *Gr.IIIb* can be distinguished from a different data group of *Gr.IIIa* by employing

a semi-logarithmic plot as shown in Figure 1. Therefore, the deformation mechanism of *Gr.IIIb* should be different from that of *Gr.IIIa*.

When Grade 122 is applied to the power plants, the applied maximum tensile stresses are not as high as those for *Gr.IIIa*, but are near the stresses for *Gr.IIIb*. The existence of *Gr.IIIb* for RHU is clearly confirmed by 1E5 h, as shown in Figure 1, because the degradation in *Gr.IIIa* is completed within a shorter duration than 1E5 h. This situation is clearly different from that for Grades 91 and 92 (Tamura & Abe, 2022b).

It is confirmed from Figure 4 that $Q_{IIIb} < Q_{IIIa}$ and $C_{IIIb} < C_{IIIa}$ throughout the entire strain range of RHU and $V_{IIIb} < V_{IIIa}$ in an accelerating creep stage and thus microstructure at rupture in *Gr.IIIb* is much recovered as compared to those of *Gr.IIIa*. However, the t_{rs} for *Gr.IIIb* are clearly longer than the estimated t_{rs} for *Gr.IIIa* as seen in Figure 1. Therefore, this problem, why $t_{IIIb} > t_{IIIa}$ at rupture, must be solved.

First, the results of the $\Delta[QVC]$ analyses through the changes from *Gr.IIIa* to *Gr.IIIb* are shown in Table 12. Table 12 indicates that determinants for the prolonged t_ϵ or t_r in *Gr.IIIb* are mainly caused by decreases in C . The values of C in an accelerating creep stage including rupture are $C \sim 10$ as shown in Figure 4 and these values are significantly smaller than $C \sim 20$ for most of heat-resistant steel (Tamura et al., 2013). Rather, these low values of $C \sim 10$ are just comparable to those for creep of a single crystal and ploy-crystals of pure iron (Karashima et al., 1971; Karashima et al., 1972; Tamura & Abe, 2022b).

Table 12. Differences between QVC for *Gr.IIIa* and *IIIb* at an indicated strain of T122/RHU steel and the calculated t_{IIIa} and t_{IIIb} at the average temperature and stress for *Gr.IIIb*. Determinant term(s) for $\log(t_{IIIb}/t_{IIIa})$ is (are) shown in bold-italics.

| Strain (%) | 0.5 | 1 | 2 | 5 | t_r |
|---------------------------|--------------|---------------|--------------|-------------|-------------|
| $\Delta[Q]$ | -14.67 | -15.65 | -10.10 | -8.27 | -7.45 |
| $-\Delta[V]$ | 0.66 | 0.54 | -0.32 | -0.46 | -0.53 |
| $-\Delta C$ | 14.28 | 14.99 | 10.73 | 9.08 | 8.33 |
| $\log(t_{IIIb}/t_{IIIa})$ | 0.27 | -0.13 | 0.30 | 0.34 | 0.35 |

Certain recovery should occur under the conditions of rupture for *Gr.IIIb* as seen in the above mentioned facts. However, the value of V is at most $V_{IIIb} \sim 300 \text{ cm}^3 \text{ mol}^{-1}$ and is far smaller than that for *Gr.IIIa*, $V_{IIIa} \sim 1000 \text{ cm}^3 \text{ mol}^{-1}$, where the dynamical recover occurs continuously throughout the whole of a specimen. Therefore, HRHD must occur in *Gr.IIIb* of the RHU, but the degree of HRHD is not as significant as that of *Gr.IIIa*.

Therefore, it is supposed, for example, that some subgrains locally nucleate and subsequently grow, and thus the deformation of the newly created subgrains becomes a rate controlling process of the deformation of the entire specimen. The stress concentration and thus the strain concentration in the newly created subgrains should be smaller than that in the HRHD zone for *Gr.IIIa*; consequently, the strain rate in the said area is mitigated, which leads to the rupture lives in *Gr.IIIb* being prolonged compared with those for the extrapolated values from *Gr.IIIa*, as confirmed in Figure 1. This assumption does not conflict with the results of not only Table 12, but also the TEM observations explained in Section 5.1.1.

5.8.2 Relaxation of Stress Concentration

To verify the validity of the assumption mentioned above concerning the relaxation of the stress concentration in a subgrain, the trial calculations mentioned in the previous work (Tamura & Abe, 2022a) were performed. First, estimated time to rupture, t_{b0} , under the conditions (T_b, σ_b) for individual data of *Gr.IIIb* using Equation 1 applying QVC of *Gr.IIIa*. Namely, t_{b0} is reference time to rupture where a high stress concentration for *Gr.IIIa* is continued under a stress for *Gr.IIIb*, σ_b . Figure 33 shows the relationship between these variables. Stress concentration is relaxed under the conditions of *Gr.IIIb*, and thus, the frequency and/or extent of HRHD becomes small, but the value of the stress concentration is unknown. Therefore, in the calculations an imaginary stress, σ_{bi} , is introduced, where $\sigma_{bi}/\sigma_b < 1$. Consequently, time to rupture is prolonged from t_{b0} to t_{bi} . These data group of (σ_{bi}, t_{bi}) construct *Gr.IIIb*.

It is only natural that to estimate t_{bi} s for *Gr.IIIb* is impossible so long as the σ_{bi}/σ_b is unknown. However, if imaginal t_{bi} s are assumed, an imaginary set of $(QVC)_i$ can be calculated under the imaginary conditions for T_{bi} and σ_{bi}/σ_b and the $(QVC)_i$ calculated should be possible to be close to the QVC experimentally obtained for *Gr.IIIb*. Figure 34 shows the relationships between $\sigma_{biav}/\sigma_{bav}$ and QVC assuming $t_{biav}/t_{b0av} = 2.84$ and

$T_{bi} = T_b$, where a term of “av” in the subscripts means an average of each variable for *Gr.IIIb*. The relationship between $\sigma_{biav}/\sigma_{bav}$ and V corresponds to that σV is constant when Q and C are constant according to Equation 1. In Figure 34, solid marks indicate the *QVC* for *Gr.IIIb* experimentally obtained. The stress ratio is confirmed to be $\sigma_{biav}/\sigma_{bav} \sim 0.88$ which corresponds to the experimentally obtained $V_{IIIb} = 309.3 \text{ cm}^3 \text{ mol}^{-1}$ for RHU. The result of this trial calculation suggests that the stress concentration is reduced by $(1 - 0.88) \times 100 = 12\%$. In this calculation, individual imaginary time to rupture for *Gr.IIIb*, t_{bi} , is assumed as $t_{biav}/t_{b0av} = 2.84$. However, there are numberless combinations of t_{bi} for *Gr.IIIb*, and therefore, other results than $\sigma_{biav}/\sigma_{bav} \sim 0.88$ even for the same time ratio of $t_{biav}/t_{b0av} = 2.84$ may be quite possible. Really, the average of the experimentally obtained time to rupture of *Gr.IIIb* for RHU is approximately 2.56 times larger than the estimated time to rupture calculated at the average temperature and average stress of *Gr.IIIb* using *QVC* of *Gr.IIIa*. Namely, there is a difference between 2.84 and 2.56. However, this difference is not questionable. That the stress concentration for *Gr.IIIb* of T122/RHU is possibly relaxed as compared with that for *Gr.IIIa* is verified through Figure 34; this is the important meaning of Figure 34.

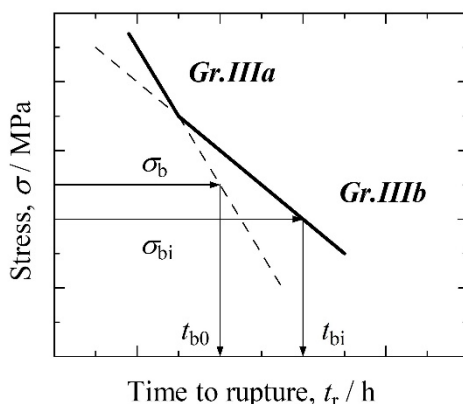


Figure 33. Schematic illustration of the variables used in the calculations shown in Figure 34

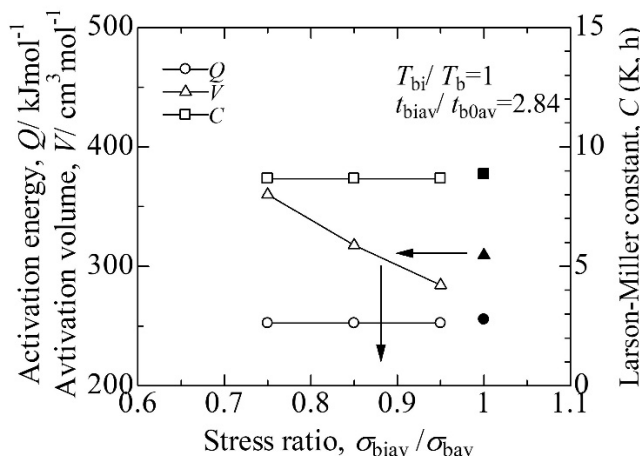


Figure 34. Calculated *QVC* as functions of the stress ratio, $\sigma_{biav}/\sigma_{bav}$. Solid marks indicate *QVC* for *Gr.IIIb* of T122/RHU, respectively

5.8.3 Strengthening Mechanism in *Gr.IIIb*

The lowering rate of the rupture strength with time in a $\sigma - \log t_r$ diagram ($\Delta\sigma/\Delta\log t_r$) for *Gr.IIIb* is mitigated as compared to that for *Gr.IIIa* as seen in Figure 1. The Laves phase and Z-phase are formed in RHU within a smaller strain ($\epsilon < 0.5\%$) as shown in Table 2. The *QVC* of RHU decrease up to an MCR point ($\epsilon \sim 1\%$) and

then remain flat in accelerating creep as shown in Figure 4. The values of Q and C for *Gr.IIIb* are minimum among the data groups of RHU. The values of V in accelerating creep for *Gr.IIIb* are larger than those for *Gr.IIIa* and thus, the degradation based on the occurrence of HRHD is mitigated. To investigate the deformation processes during creep the $[QVC]_s$ analyses are made on *Gr.IIIb* and the results are shown in Table 13. During transient creep ($\varepsilon \leq 1\%$) of *Gr.IIIb* the $[Q_s]$ decreases with increasing strain similar to the case for *Gr.IIIa* as shown in Table 4, but the determinant terms for the change in creep rate are the decreases in $[V_s]$ and C_s . This indicates that the beginning and continuous occurrence of HRHD is necessary to retain an apparent transient creep stage.

Table 13. Changes in Q_s , V_s , and C , and $\log(\dot{\varepsilon})$ between two adjacent strains for *Gr.IIIb* of T122/RHU

| Strain range | [0.5-1%] | [1-2%] | [2-5%] | [5%- t_r] |
|--|--------------|-------------|-------------|--------------|
| $-\Delta[Q_s]$ | 8.30 | 4.25 | -1.80 | -2.91 |
| $\Delta[V_s]$ | -0.56 | -0.12 | 0.18 | 0.19 |
| ΔC_s | -7.81 | -3.73 | 2.23 | 3.74 |
| $\Delta \log(\dot{\varepsilon}, \%h^{-1})$ | -0.07 | 0.40 | 0.61 | 1.02 |

On the other hand, during accelerating creep of $\varepsilon = 1 - 2\%$ the determinant to the creep rate is a decrease in $[Q_s]$ with increasing strain, which is similar to the case of *Gr.IIIa*. However, in an accelerating creep stage of $\varepsilon \geq 2\%$ in *Gr.IIIb*, increases in both $[V_s]$ and C_s are the determinants for the increasing creep rate again, whereas the determinant for *Gr.IIIa* is a decrease in $[Q_s]$ as shown in Table 4. HRHD should occur in *Gr.IIIb* of RHU continuously during the entire strain range, because the values of the V of *Gr.IIIb* are small even though the V of *Gr.IIIb* increases as compared to those of *Gr.IIIa*.

Furthermore, it is clearly noticed from Table 13 that the $[Q_s]$ of *Gr.IIIb* turns into an increase from a decrease for $\varepsilon \geq 2\%$ though a small increase in Q during accelerating creep of *Gr.IIIb* is also barely confirmed in Figure 4. This point for *Gr.IIIb* is clearly different from that of *Gr.IIIa*. Such phenomena as $[Q_s]$ or Q increases during accelerating creep are already confirmed in an accelerating creep stage of 1W, 4W, Grades 91 and 92 tested at higher temperatures for example *Gr.IIa*, *IIIa*, *IIIb*, and *IV* (Tamura & Abe, 2021a; 2021b; Tamura, 2022). The creep strength during the accelerating creep stage of *Gr.IIIb* increases owing to the relaxation of the stress concentration, which is caused by the nucleation and growth of subgrains as explained in Section 5.8.2. In addition, the DFRP mechanism operates on $M_{23}C_6$ carbide particles during the restructuring of the subgrains, which stabilizes the sub-boundaries and thus increases or retains the long-term creep strength of tempered martensitic steel at high temperatures after important strengthening factors such as martensitic structure and MX particles are exhausted.

Grade 92 exhibited high creep strength at high temperatures even after 1E5 h. These high-strength levels after a long duration are retained by the stabilized subgrains with the help of $M_{23}C_6$ and finely dispersed MX particles as discussed in Section 5.7 (Figure 31). However, the fine MX particles even in Grade 92, are consumed at any rate after longer a duration of 1E5 h, and the DFRP mechanism for $M_{23}C_6$ becomes important.

5.9 Rupture Strength for 1E5 h at 600 °C of Grade 122

5.9.1 Comparison of σ_{1E5} of Grade 122 With Those of Grades 91 and 92

Figure 35 shows the correlation between initial hardness and σ_{1E5} at 600 °C of all high-strength martensitic steels investigated in this study. The σ_{1E5} for Grades 91 and 92 are calculated using QVC for each *Gr.IIIa* (Tamura & Abe, 2021b; Tamura, 2022) and the σ_{1E5} for Grade 122 are calculated using QVC for *Gr.IIIb*. A solid regression line ($r = 82\%$) is obtained for *Gr.IIIb* of Grade 122 and for *Gr.IIIa* of Grades 91 and 92. In Figure 35 the σ_{1E5} calculated for *Gr.IIIa* of Grade 122 are also plotted using daggers. A dashed regression line ($r = 84\%$) is also given for all rupture strengths based on *Gr.IIIa*.

Rupture strengths based on *Gr.IIIb* for Grade 122 are lightly higher than those for *Gr.IIIa*. The reasons for this are discussed in Section 5.8. Figure 35 indicates a negative correlation between hardness and σ_{1E5} . However, this is not a causal relationship, because the effect of initial hardness should not directly hold for a long duration of time. The reasons for this are discussed in Sections 5.4 and 5.5 and a main reason is that high hardness promotes the occurrence of HRHD through coarsening of the Laves phase particles. Anyway, reducing the initial hardness is desirable to improve σ_{1E5} .

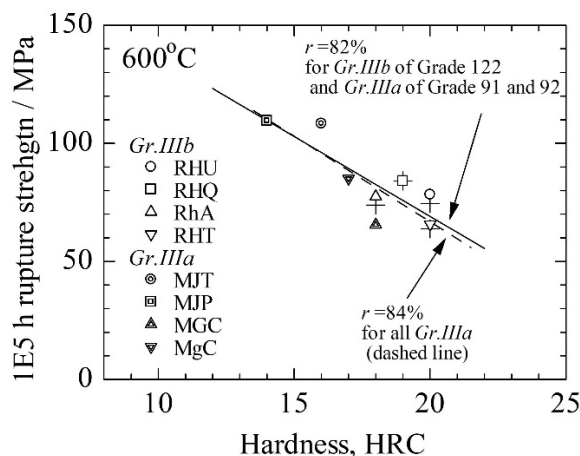


Figure 35. Correlation between initial hardness and σ_{1E5} at 600 °C for Grades 91, 92, and 122. Daggers denote 1E5 h rupture strength of Grade 122 calculated for *Gr.IIIa*

5.9.2 Correlation Between σ_{1E5} and Parameters Obtained from Initial- or Short-Term Characteristics

Here, several kinds of parameters, which are calculated using initial characteristics or relatively short-term creep data, are newly introduced in addition to PAGESn and the correlations between these parameters and σ_{1E5} are discussed to improve σ_{1E5} at 600 °C of Grade 122.

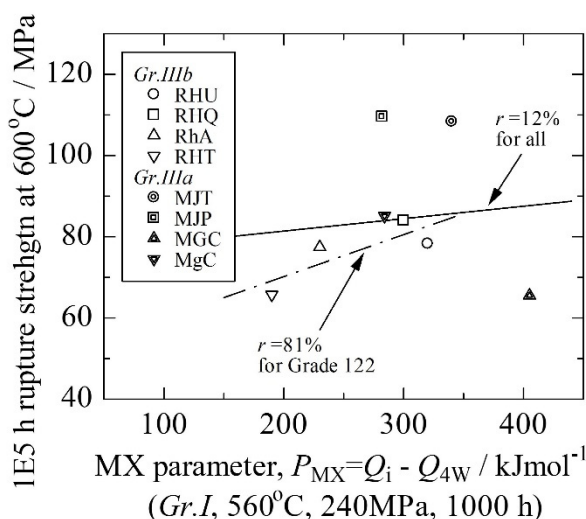


Figure 36. Correlation between MX parameter, P_{MX} , and σ_{1E5} at 600 °C for Grades 92 and 122

First, Figure 36 shows the correlation between the initial MX parameter and σ_{1E5} at 600 °C of Grades 91, 92 and 122; the MX parameter is defined as $P_{MX} = Q_i - Q_{4W}$, where Q_i and Q_{4W} are the activation energy for 1000 h of *Gr.I* for individual martensitic steel shown in the Figure 11. P_{MX} is a parameter representing the initial amount of finely dispersed MX particles inside subgrains, ρ_{MXi} . Regression lines in Figure 36 are calculated for all data ($r = 12\%$) and for Grade 122 ($r = 81\%$). Figure 36 indicates that the σ_{1E5} at 600 °C of Grade 122 has a better correlation with P_{MX} than HRC (Figure 35), though σ_{1E5} for all steels investigated has little correlation with P_{MX} . This means the following; initial P_{MX} should affect even on the long-term rupture strength of σ_{1E5} under the limited conditions like the case of Grade 122, but ρ_{MXi} easily decreases during long-term services and thus it is necessary to elaborate an idea on delaying the formation of Z-phase.

Figure 37 shows the correlation between the Laves phase coarsening parameter for *Gr.II*, P_{LavesC} , and σ_{1E5} at 600 °C of Grades 91, 92, and 122; the Laves phase coarsening parameter is defined as $P_{LavesC} = Q_{max}/Q_{tr}$, where Q_{max} and Q_{tr} are the activation energies for the maximum value during creep of *Gr.II* and at rupture, respectively. The value of Q for *Gr.II* peaks near the MCR point and then decreases with increasing creep strain until rupture owing to the coarsening of the Laves phase particles as shown in Figure 4. Therefore, P_{LavesC} becomes large when the Laves phase hardening is disappeared owing to the coarsening of the Laves phase particles. *Gr.II* is selected for the calculation of P_{LavesC} , because the Laves phase hardening is most significant and the softening owing to the coarsening of the Laves phase particles is also observed during creep of *Gr.II*. Regression lines in Figure 37 are calculated for all data ($r = 57\%$) and for Grade 122 ($r = 87\%$). Figure 37 indicates that σ_{1E5} is small for a large P_{LavesC} , that is, the σ_{1E5} decreases when the Laves phase particles are coarsened. Concerning Grade 122, $r = 87\%$ for P_{LavesC} in Figure 37 is sufficiently improved as compared with the cases for HRC and P_{MX} (Figures 35 and 36). This does not mean that the Laves phase hardening is more effective on σ_{1E5} at 600 °C as compared with the hardening owing to the finely dispersed MX particles. Rather, the MX hardening is still effective on σ_{1E5} at 600 °C as compared to the Laves phase hardening, but finely dispersed MX particles in RHU may be abnormally consumed due to the severe occurrence of HRHD, thus the σ_{1E5} of RHU is lowered, and consequently the correlation coefficient becomes apparently lowered in Figure 36, $r = 81\%$ for Grade 122.

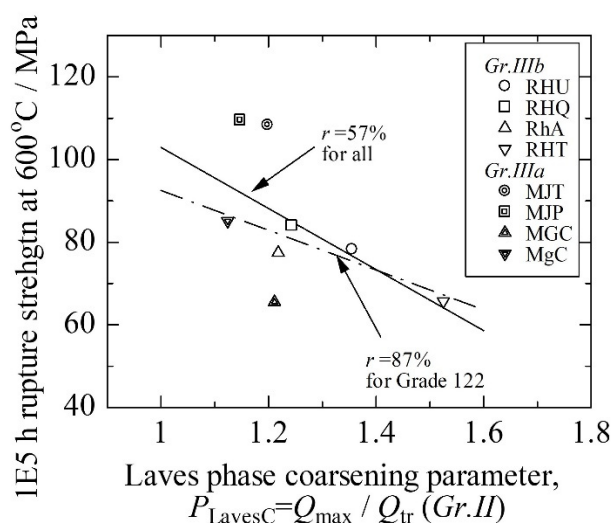


Figure 37. Correlation between Laves phase coarsening parameter for *Gr.II*, P_{LavesC} , and σ_{1E5} at 600 °C for Grades 91, 92, and 122

In Figure 37, the regression coefficient for all is 57% and is rather low and furthermore, the regression coefficient of Grade 122 is rather high $r = 87\%$, but is not sufficiently high. The result for RhA is possibly interpreted that the σ_{1E5} or P_{LavesC} for RhA may be too low, though the details are unknown.

As shown in Table 2, Z-phase is formed in a later stage of *Gr.II* of RHU, and is also formed to a greater or lesser extent in some steels up till rupture (Sawada et al., 2007). In these cases, Q_{tr} in P_{LavesC} becomes smaller or P_{LavesC} becomes larger than the cases that the Z-phase is not formed, because the Z-phase reduces Q_{tr} owing to the decrease in ρ_{MXi} .

However, the effect of the Z-phase formation on P_{LavesC} is not that large because of the following reasons; the Laves phase hardening in *Gr.II* are certainly confirmed in each $t_r - \sigma$ relation of MJP, MJT, MgC, RhA, and RHT and concerning MGC, RHU, and RHQ the Laves phase hardening in *Gr.II* is not so clearly confirmed, but the softening owing to the formation of Z-phase like the case of *Gr.III* is not confirmed (Tamura & Abe, 2021b; Tamura, 2022; Figures 1; A2; A3).

Anyway, Figure 37 indicates the important matter that the Laves phase hardening is possibly evidenced even after the long-term duration of time of 1E5 h and, furthermore, the coarsening of the Laves phase particles triggers the occurrence of HRHD and thus the σ_{1E5} is degraded largely due to the drastic consumption of the finely dispersed MX particles through the formation of the Z-phase as explained in Section 5.7. Therefore, it is desired to stabilize

the Laves phase particles during the long-term duration of time or, furthermore, to keep P_{LavesC} at rupture in *Gr.II* as low as possible.

Figure 38 shows the correlation between the HRHD parameter for *Gr.II*, P_{HRHD} , and σ_{1E5} at 600 °C of Grades 91, 92 and 122; the HRHD parameter is defined as $P_{HRHD} = V_{max}/V_{tr}$, where V_{max} and V_{tr} are the activation volumes for the maximum value during creep of *Gr.II* and at rupture, respectively. *Gr.II* is selected for the calculation of P_{HRHD} , because decreasing V during creep is observed within the short duration of time.

The value of V for *Gr.II* peaks near the MCR point and then decreases with increasing creep strain until rupture owing to the occurrence of HRHD as shown in Figure 4. Regression lines in Figure 38 are calculated for all data ($r = 63\%$) and for Grade 122 ($r = 95\%$). Figure 38 indicates that σ_{1E5} is small for large P_{HRHD} , that is, σ_{1E5} decreases when the HRHD occurs severely. Concerning Grade 122, $r = 95\%$ for P_{HRHD} in Figure 38 is sufficiently high as compared with the cases of HRC, P_{MX} , and P_{LavesC} (Figures 35, 36, and 37).

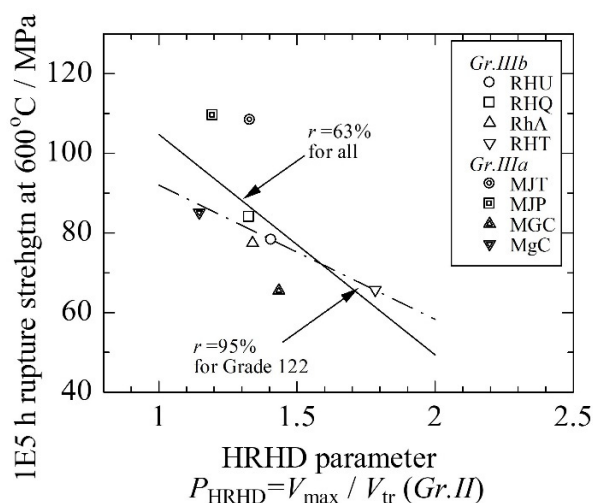


Figure 38. Correlation between HRHD parameter for *Gr.II*, P_{HRHD} , and σ_{1E5} at 600 °C for Grades 91, 92, and 122

HRHD begins to occur near the occasionally coarsened particles formed on the boundaries. The Laves phase particles are a major component of the coarsened particles and furthermore, the Z-phase formed during creep of *Gr.II* must impact on P_{HRHD} . However, it is found comparing P_{LavesC} with P_{HRHD} of Grade 122 shown in Figures 37 and 38, respectively, that the effect of the Z-phase on P_{HRHD} is small or the Z-phase particles formed until rupture in *Gr.II* are smaller than those of the Laves phase. The reasons are as the following; first, the Laves phase and the Z-phase particles are approximately 600 and 50 nm, respectively for specimens of T91/MGC ruptured at 600 °C for 1000 h, a duration of which corresponds to the average time to rupture for *Gr.II* of RHU shown in Table 2 (Suzuki et al., 2000). Secondly, as a reference of RhA, P_{LavesC} s of RHU and RHQ are larger than that of RhA (Figure 37), though P_{HRHD} s of RHU, RHQ, and RhA are comparable (Figure 38). Namely, only the effect of the coarsened Laves phase particles on σ_{1E5} at 600 °C is deduced in Figure 38, though in Figure 37 the minor effect of the decrease in ρ_{MXi} on σ_{1E5} is overlapped on the effect of the coarsened Laves phase particles. Consequently, the regression coefficients for all and for Grade 122 in Figure 38 are improved as compared with those of Figure 37. This supports the conclusion claimed in Section 5.7 that the ease of the occurrence of HRHD owing to the occasionally coarsened Laves particles, which leads to the drastic consumption of finely dispersed MX particles in an HRHD zone, is the root cause of the unexpected degradation in σ_{1E5} of high-strength martensitic steel.

Anyway, Figures 36, 37, and 38 indicates the important matter that the Laves phase hardening is possibly evidenced especially in MJT and MJP even after the long-term duration of time of 1E5 h and furthermore, the coarsening of the Laves phase particles triggers the occurrence of HRHD and thus the σ_{1E5} is degraded largely due to the drastic consumption of the finely dispersed MX particles through the formation of the Z-phase as explained in Section 5.7 therefore, it is desired to stabilize the Laves phase particles during the long-term duration of time or in addition to keep P_{LavesC} at rupture in *Gr.II* as low as possible.

Figure 39 shows the correlation between the PAGSn and σ_{1E5} at 600 °C of Grades 91, 92 and 122. The regression coefficient of $r=98.5\%$ for Grade 122 is extremely high as expected from the correlation between the PAGS number and the rupture strength for 1E5 h of *Gr. IIIa* (Figure 23). A dashed line for Grade 92 is given as a regression line with the same slope as that for Grade 122. The difference in intercepts of two regression lines shown in Figure 39 is 36.2 MPa, which is comparable to the difference in rupture strength between P92/MJP and pl-122/RhA as shown in Figure 30.

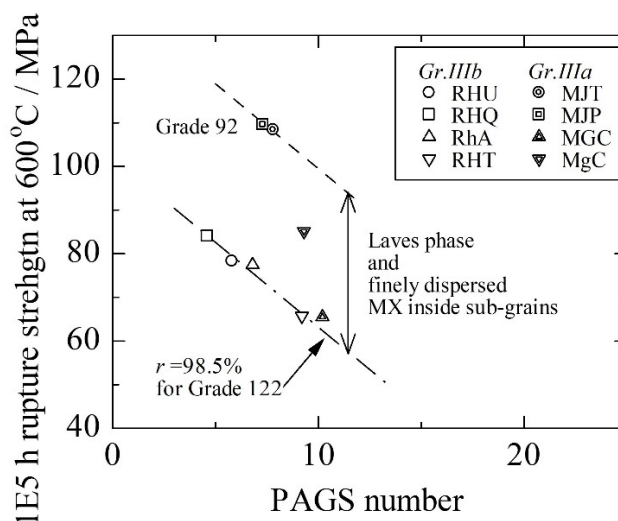


Figure 39. Correlation between PAGSn and σ_{1E5} at 600 °C for Grades 91, 92, and 122

According to the discussion in Section 5.7, this difference is caused by the retained amount of Laves phase and the retained and finely dispersed MX particles inside subgrains. Laves phase hardening is not expected at 600 °C in Grade 91, because the Laves phase of Fe_2Mo formed in Grade 91 is easily coarsened at 600 °C (Tamura & Abe, 2022b). Finely dispersed MX particles inside subgrains is almost disappeared in T91/MGC at rupture for 80 736.8 h (Sawada et al., 2011). Therefore, σ_{1E5} at 600 °C of MGC is the lowest in Figure 39 (see also Figure 30). On the other hand, σ_{1E5} of MgC is between two regression lines. This is because a considerable amount of MX particles is retained at rupture of MgC for 78 236.5 h (Sawada et al., 2014), though the Laves phase hardening is not expected. Nevertheless, PAGS number is an essential factor in controlling the long-term rupture strength at 600 °C and therefore, low number of PAGS is desirable.

Rupture strength for 1E5 h at 600 °C of Grade 122 is discussed referring to the σ_{1E5} s of Grades 91 and 92 through Figures 35–39. First, to improve σ_{1E5} of Grade 122 reducing PAGS number is recommended from Figure 39. This is interpreted as recovery of the matrix is promoted because the total boundary surface area of prior austenite grain increases and furthermore, PAGBs are not considered to migrate largely throughout the whole duration of rupture life of 1E5 h. Four parameters of HRC, P_{MX} , P_{LavesC} , and P_{HRHD} have correlations with σ_{1E5} as shown in Figures 35–38, but these parameters simultaneously correlate with PAGS number respectively. Therefore, it is meaningless to discuss in detail the differences in σ_{1E5} between for each heat in Grade 122. However, the difference in σ_{1E5} between for Grade 92 and Grade 122 shown in Figure 39 should be explained in terms of the stability of the Laves phase and finely dispersed MX particles inside subgrains as explained in the paragraphs regarding Figure 39.

From this point of view to improve the σ_{1E5} at 600 °C, the HRC of Grade 122 (av. HRC~19.3) is desired to be lowered to the levels of Grade 92 (av. HRC~15) referring to Figure 35; this is interpreted as the following. When the HRC number is high, the basic strength of martensite structure which is a major component of the HRC as shown in Figure 18 becomes large; partial contributions of the calculated HRC of Grades 122 and 92 are 10.2 and 6.4 for average, respectively as shown in Figure 18. When the basic strength at ambient temperature of high-strength martensitic steel is high, the recovery rate of the martensite structure at creep temperature is high, because the basic strength of the martensite structure may be caused by high dislocation density and fine lath martensite structure. When recovery rate is high, the precipitation of the Laves phase is promoted and subsequently the

coarsening of the Laves phase is also promoted. Therefore, the formation of the coarsened particles triggers the occurrence of HRHD and then, in an HRHD zone the decomposition of the microstructure, i.e., the consumption of the finely dispersed MX particles and the resultant formation of the Z-phase is promoted due to the stress and strain concentration in an HRHD zone. This metallurgical reaction chain is evidenced through Figures 35–39.

Concluding this section, it is important to improve the σ_{1E5} at 600 °C of Grade 122, not only to reduce PAGSn and HRC, but also to stabilize the Laves phase. The σ_{1E5} of Grade 122 at 600 °C is determined by the creep of *Gr.IIIb* and therefore, stabilizing $M_{23}C_6$ is also important to improve the σ_{1E5} at 600 °C of Grade 122 as discussed in Section 5.8.

5.10 Improvement of Rupture Strength of Grade 122

Long-term rupture strength at 600 °C of Grade 122 is determined in conditions similar to *Gr.IIIb* as described in Section 5.8. It is important to improve rupture strength of Grade 122 for *Gr.IIIb*. To achieve this, it is effective to stabilize $M_{23}C_6$ carbide particles as explained in Section 5.8. For this purpose, the additions of W (Yoshizawa, Igarashi, & Nishizawa, 2005) and B (Abe, 2006; Danielsen, 2007) are effective.

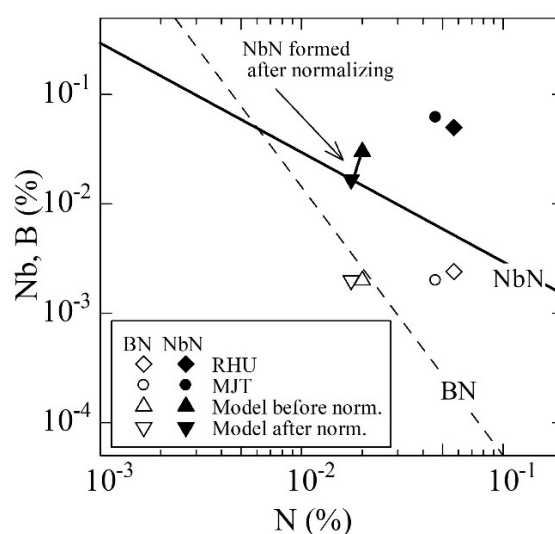


Figure 40. Relationships between solubility limit in austenite for BN (dashed line); NbN (solid line); N, B, and Nb content of RHU, MJT, and a model steel. A solubility limit for BN is obtained for 9Cr-3W-3Co-0.2V-0.05NbB steels solution treated at 1050–1150 °C (Abe, 2007a) and a solubility limit for NbN at 1070 °C is calculated using Narita's data (1975)

As pointed out by Abe et al. (2007a) B and N content of Grade 122 listed in Table 1 are excessive and 0.02% of N content may be sufficient for 0.002% B in Grade 122. Many additions of B and N are detrimental and massive BN particles formed cause a decrease in rupture ductility (Gu et al., 2014; Abe et al., 2018). The amount of 0.03% addition of Nb may be enough for adequately controlling PAGS during normalizing. The relationships between N, B, and Nb content of RHU, MJT, and a model steel with 0.02%N-0.002%B-0.03%Nb before normalizing are shown in Figure 40. In addition to these, the solubility limits for BN (Narita, 1975) and NbN (Abe et al., 2007a) in austenite are shown in Figure 40. The N, B, and Nb contents in the matrix of the model steel after normalizing are also plotted in this figure. According to Figure 40, BN is not formed in the model steel, and the amount of NbN formed after normalizing is estimated to be approximately 0.02%. In comparison, Figure 40 indicates that a great deal of coarse BN and NbN particles are formed in Grades 92 and 122 during normalizing. The reliability of the solubility limits of BN and NbN shown in Figure 40 must be validated for 12Cr steel and, furthermore, it must be also validated whether 0.02% of estimated value of NbN is sufficient to control the PAGS number.

The value of N_{av} is calculated as 0.037 at% for the model steel with 0.02%N, 0.03%Nb, and 0.002%B. $N_{av} = 0.037$ at% is smaller than those for Grade 92, $N_{av} = 0.11$ and 0.12 at% for MJT and MJP, respectively. However, a certain level of MX hardening owing to VN which forms during tempering is expected when referring to Figure 13. If the ρ_{MXi} is insufficient to maintain uniform deformation as explained in Section 5.2.3, an N content in the model steel should be raised to approximately 0.03%. Careful experimentation is required to

optimize the N content. In the case of $N = 0.02\%$, $V_{\text{free}} = 0.18 \text{ at}\%$ is obtained for $V = 0.2\%$ for a model steel. Figure 41 shows the correlation between the V_{free} and σ_{1E5} at $600 \text{ }^\circ\text{C}$ for Grades 91, 92, and 122. Here, σ_{1E5} has a positive correlation with V_{free} for Grades 92 and 122 with $\text{Mo} + \text{W} \sim 0.76 \text{ at}\%$, although the correlation coefficient is not as high, $r = 84\%$. It is surprising that σ_{1E5} is raised at a rate of $\Delta\sigma_{1E5}/\Delta V_{\text{free}} \sim 57 \text{ MPa}/0.1 \text{ at}\%$. Most of the differences in σ_{1E5} between Grades 92 and 122 are caused by the Laves phase particles on the boundaries and finely dispersed MX inside subgrains, which are still active for hardening after 1E5 h of creep as discussed in Section 5.7.

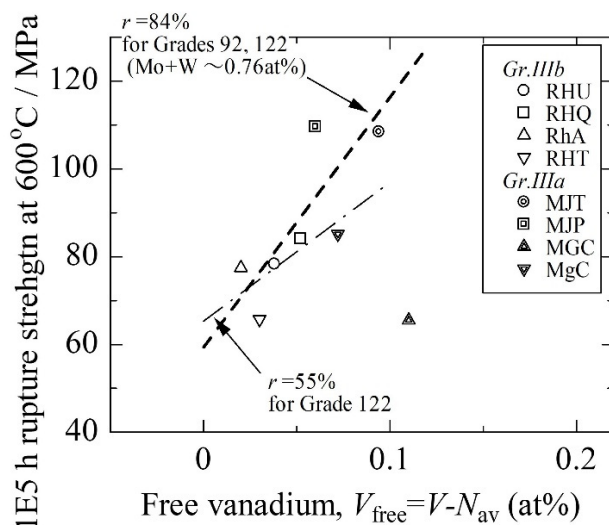


Figure 41. Correlation between free vanadium and σ_{1E5} at $600 \text{ }^\circ\text{C}$ for Grades 91, 92, and 122

V is hardly dissolved in Laves phase and M_{23}C_6 (Suzuki et al., 2000). Free vanadium atoms in the matrix are reasonably paired with nitrogen atoms dissolved in the matrix and the pairs have an interaction with moving dislocations dynamically, which results in dynamic strain aging hardening (Tamura & Abe, 2021b; Tamura, 2022). This hardening is reasonably expected regardless of the degradation of the microstructure and is evidenced by an increase in HRC as shown in Figure 18. Most of V dissolved in the matrix in Grade 122 is still relevant for the long-term rupture strength and therefore, V is not necessary to reduce from Grade 122, provided that V does not promote the formation of δ -ferrite.

Mo has been used in most of heat-resistant steel and is a constituent element of Laves phase, which hardens a short-term rupture strength at $600 \text{ }^\circ\text{C}$ of high-strength martensitic steel. However, coarsened particles of Fe_2Mo possibly trigger the occurrence of HRHD which leads to an unexpected drop in long-term rupture strength, which promotes the consumption of finely dispersed MX particles. Furthermore, a portion of Mo dissolves in M_{23}C_6 and increases the risk of coarsening M_{23}C_6 particles, which promotes the growth of subgrains. Currently, there is no report that Mo suppresses the growth rate of M_{23}C_6 , although W suppresses the growth rate of M_{23}C_6 (Yoshizawa et al., 2005; Abe, 2006; Danielsen, 2007) and the diffusion constant in α -Fe at $\sim 600 \text{ }^\circ\text{C}$ increases in the order of $D_{\text{Mo}} > D_{\text{Cr}} > D_{\text{Fe}} > D_{\text{W}}$, where the suffixes denote each constituent element of M_{23}C_6 (Oikawa, 1982). Here, a temperature of $600 \text{ }^\circ\text{C}$ is higher than the nose temperature of Fe_2Mo as discussed in the previous work (Tamura & Abe, 2021b). Therefore, it is desired to exclude Mo from ASME Grade 122.

Preferably, the growth rate of MX particles or the formation of the Z-phase should be suppressed by the addition of minor elements. However, this might not be sufficient. It is reported that the addition of Re is effective to increase rupture lives of high-strength martensitic steel (Hashizume et al., 2009; Fedoseeva, Nikitin, Dudova, & Kaibyshev, 2019). The mechanism for this is as that the growth rate of the Laves phase is suppressed by the addition of Re (Hashizume et al., 2009; Tamura & Abe, 2021b), which delays the occurrence of the HRHD and suppresses the consumption of finely dispersed MX particles. Therefore, the addition of Re is desirable to improve the long-term rupture strength of ASME Grade 122.

5.10.2 Controlling the Microstructure

According to Figures 22, 23, 35, and 39, reducing both HRC and PAGS numbers is desired to improve the σ_{1E5} at 600 °C of Grade 122. The PAGS numbers of Grade 122 shown in Figure 23 are sufficiently low. Although the HRC numbers are significantly high and are possibly lowered to some extent, it is not expected because high values are caused by the high alloying content and higher amount of $M_{23}C_6$ of Grade 122 as compared to Grades 91 and 92 as shown in Figure 18. Reducing carbon may be impossible in terms of phase balance. Figure 17 suggests that reducing a Si content is one of the feasible choices to reduce hardness. The hardness of tubular goods are generally high. This may be caused by a straightening treatment for shipping. In these cases, an increase in hardness number should preferably be suppressed as low as possible.

Grade 122 with a high-Cr content similar to RHT easily forms small amount of δ -ferrite. However, the δ -ferrite lowers toughness and creep strength under the influence of hoop stresses in tubes and pipes. The precipitation of the Laves phase in δ -ferrite increases the short-term creep strength; however, excluding δ -ferrite is desirable.

In a model steel, reducing the N, B, Nb, and Mo is highly recommended as compared to the chemical composition of a standard ASME Grade 122 steel. When we consider the phase balance of the model steel with reduced N content, reducing Nb and Mo may be insufficient. In this case, the addition of Co is inevitable and reducing the W is probably needed.

After the detailed design of a combination of the chemical composition and heat treatment is performed, some trial heats are used to melt the steel in a laboratory scale and the characteristics should be investigated.

5.10.3 Monitoring Creep Strength

Besides the conventional investigations shown in Table 1 and a creep datasheet (NIMS, 2020; 2021), the amount, size, and distribution of $M_{23}C_6$, BN, and MX particles, and the dislocation density and subgrain size are necessary to be examined employing scanning electron microscopy and TEM. Moreover, after confirming no existence of δ -ferrite using an optical microscope, short term creep tests for *Gr.I* and *II* conditions up to a maximum duration of 3000 h, respectively, should be performed. Thereafter, *QVC* analyses are conducted and the *Qs* and *Vs* of *Gr.I* are plotted as functions of the calculated t_e and $t_{r,s}$ referring to Figures 11 and 12. Thereafter, the existence of an adequate amount of ρ_{MXi} and the extent of homogeneous deformation are judged from the data obtained.

Furthermore, the Laves phase coarsening parameter for *Gr.II*, P_{LavesC} , and the HRHD parameter for *Gr.II*, P_{HRHD} , are calculated referring to Figures 37 and 38. Subsequently, the extent of the drop in σ_{1E5} at 600 °C in *Gr.IIIa* or *IIIb* can be roughly estimated referring to Figures 37 and 38.

Next, a set of long-term creep tests under the conditions of *Gr.IIIa* is recommended and the consumption rate of finely dispersed MX particles during creep can be estimated without interrupting the creep tests: The creep test conditions for *Gr.IIIa* or *IIIb* can be selected referring to Figures 1 and A1-A3 and the *QVC* analyses are feasible by monitoring the creep curves.

Sawada et al. (2011; 2014) shows that the long-term rupture strength of Grade 91 strongly depends on the consumption rate of the ρ_{MX} . Figure 38 shows that the long-term rupture strengths of Grades 91, 92, and 122 are lowered with an increase in the HRHD parameter, $P_{HRHD} = V_{max}/V_{tr}$. This suggests that the σ_{1E5} is lowered when the finely dispersed MX particles are heavily consumed owing to the strain concentration occurred in the HRHD zone. Therefore, Figure 42 shows the activation volume for *Gr.IIIa* of Grades 91, 92, and 122 and the specific ρ_{MX} , ρ_{MX}/ρ_0 , for MGC and MgC as functions of creep strain, where ρ_0 denotes an initial number density of MX. The variations of V and ρ_{MX}/ρ_0 during creep are similar. Therefore, Figure 43 shows the relationship between V/V_0 and ρ_{MX}/ρ_0 during creep for *Gr.IIIa*, where V_0 is the V for *Gr.IIIa* at $\varepsilon = 0.5\%$. Concerning Grade 91, a linear relationship is confirmed between V/V_0 and ρ_{MX}/ρ_0 , although the test conditions are limited. When further research on the other conditions for *Gr.IIIa* are continued and a proper data band is established, the reduction rate of ρ_{MX}/ρ_0 and the extent of the drop in σ_{1E5} at 600 °C can be estimated from the changes in V/V_0 during creep without interrupting the creep tests. This is because V can be calculated from the creep curves which can be monitored online.

After the considerations in Section 5.7, considerable amounts of finely dispersed MX particles are estimated to be retained at rupture of Grade 92. The ρ_{MX}/ρ_0 s for MJP and MJT can be roughly estimated using the regression line for MGC using the observed values of V/V_0 for MJP and MJT, and the estimated procedures are indicated by arrows in Figure 43.

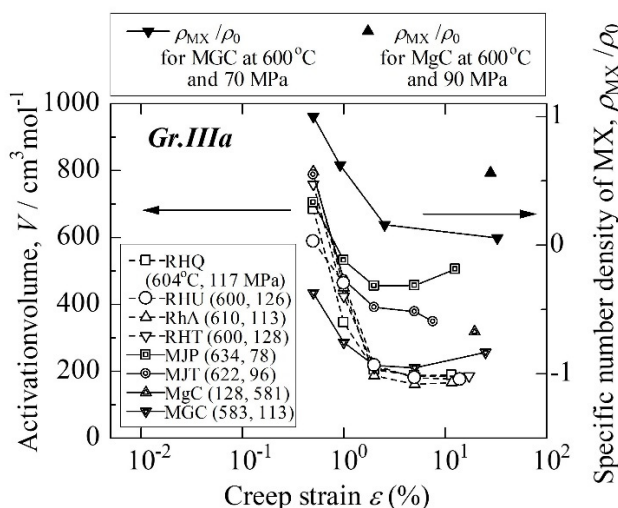


Figure 42. Activation volume and specific number density of MX of Grades 91, 92, and 122 as functions of creep strain tested under the conditions of *Gr.IIIa*

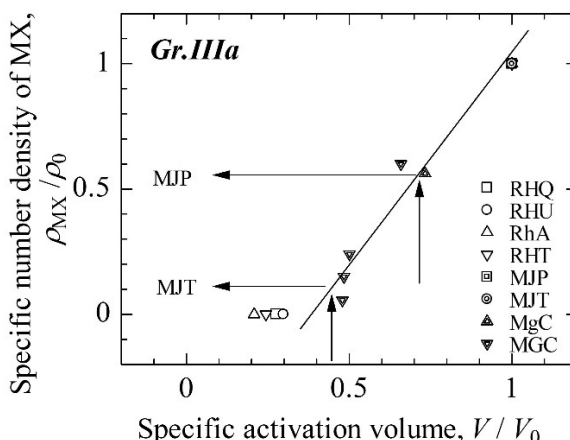


Figure 43. Relationship between V/V_0 and ρ_{MX}/ρ_0 for *Gr.IIIa* of high-strength martensitic steel. The regression line is calculated for MGC. The ρ_{MX}/ρ_0 s for MJP and MJT are not yet obtained, but the estimation procedure for ρ_{MX}/ρ_0 is indicated using arrows and the details are explained in Section 5.10.3

The data for ρ_{MX}/ρ_0 are plotted at $\rho_{MX}/\rho_0 = 0$ for Grade 122, because these data have not been obtained yet. Nevertheless, the data for Grade 122 are at a distance from the regression line for Grade 91. Therefore, the data band for estimation must be determined for each steel grade. We can estimate the consumption ratio of the finely dispersed MX particles and thus the extent of the drop in σ_{1E5} at 600 °C of the high-strength martensitic steel if the accuracy of the regression line in Figure 43 can be raised in future.

6. Conclusions

The long-term creep curves of Grade 122 steel pipe, plate, and tow tubular product forms were analyzed by applying an exponential law to the test temperature (T), stress (σ), time to rupture (t_r), and time to a specific strain (t_ϵ) and comparing the results of Grades 91 and 92 steel. The observed creep variables, T , σ , and t_r or t_ϵ , were converted to activation energy (Q), activation volume (V), and Larson–Miller constant (C) without using any adjustable parameters. The variations in Q , V , and C as functions of creep strain are discussed metallurgically, and the following conclusions are drawn:

- 1) The hardness numbers for four heats of Grade 122 steel are higher than the average hardness of Grades 91 and 92. This is because the intrinsic martensitic structure of tempered Grade 122 is harder than those of Grades

- 91 and 92, and the amount and/or number density of $M_{23}C_6$ in Grade 122 is larger than those of Grades 91 and 92.
- 2) The initial number density of finely dispersed MX particles inside subgrains of Grade 122 is estimated to be smaller than those of Grades 91 and 92.
 - 3) The rupture strength of Grade 122 steel at 600 °C decreases unexpectedly after several tens of thousands of hours (for the conditions of a data group *Gr.IIIa*) similar to Grades 91 and 92. However, *Gr.IIIa* of Grade 122 steel starts earlier than Grades 91 and 92, and the decreasing rates ($\Delta\sigma/\Delta\log t$) of Grade 122 are larger than those of Grades 91 and 92. Under *Gr.IIIb* conditions of Grade 122 steel at 600 °C for lower stresses than those of *Gr.IIIa*, the degradation rate ($\Delta\sigma/\Delta\log t$) is mitigated.
 - 4) The rupture strengths of Grade 122 steel after 1E5 h at 600 °C are lower than those of Grade 92 steel and comparable to those of Grade 91 steel.
 - 5) The creep and rupture strengths of Grade 122 steel subjected to high stresses for short durations are higher than those of Grade 92 steel owing to the initial elevated hardness and Laves phase hardening. However, the Laves phase particles in Grade 122 steel are estimated to be easily coarsened; the long-term rupture strength of Grade 122 steel decreases rapidly.
 - 6) A principal cause of the rapid degradation of the long-term rupture strength of Grade 122 steel is the sequential decomposition of the microstructure triggered by large particles. As some particles of the Laves phase are occasionally coarsened at boundaries, such as prior austenitic grain boundaries, heterogeneous recovery occurs around the coarsened Laves phase particles. Subsequently, heterogeneous deformation occurs inside a heterogeneously recovered zone, and the decomposition of the microstructure is promoted inside the heterogeneously recovered and heterogeneously deformed (HRHD) zone (subgrain). This is achieved by straining at the formation of the Z-phase, which consumes finely dispersed MX particles, and coarsening of the particles near the boundaries of a subgrain. Thereafter, because of the local strain inside the subgrains, stress- and strain concentrations are generated around a subgrain, and the recovered subgrains spread from one to another throughout the entire specimen. Thus, the rupture strength unexpectedly and rapidly decreases in *Gr.IIIa*.
 - 7) The finely dispersed MX particles in high-strength martensitic steel not only increase the creep strength, but also promote homogeneous deformation compared to simple martensitic steel. Therefore, the consumption of finely dispersed MX particles promotes heterogeneous deformation, and the long-term creep strength of high-strength martensitic steel decreases at the onset of finely dispersed MX particle consumption in *Gr.IIIa*.
 - 8) The degradation rate of $\Delta\sigma/\Delta\log t$ in *Gr.IIIb* is mitigated compared to that of *Gr.IIIa* because the stress- and strain concentrations in a subgrain are mitigated owing to recovery, as well as the nucleation and growth of subgrains. Furthermore, the hardening is added due to the redistribution of $M_{23}C_6$ particles according to the movement of sub-boundaries and/or the generation of new subgrain boundaries.
 - 9) To improve the long-term rupture strength of ASME Grade 122, lowering the initial hardness and stabilizing not only the $M_{23}C_6$ carbide, but also the Laves phase is recommended. To achieve this, it is necessary to reduce the N, B, Nb, and Mo contents as much as possible under the appropriate heat-treatments.

List of Symbols and Abbreviations

| | |
|---------------------|---|
| ε | Strain |
| $\dot{\varepsilon}$ | Creep rate or strain rate |
| ε_i | Strain of i^{th} in Equation 3 |
| ε_{MCR} | Strain for an MCR point |
| ε_Z | Start strain for the Z-phase formation |
| λ | Maximum distance that a dislocation can move from a start point to the next stable position |
| ν | thermal frequency |
| ν_{eff} | Effective attempt frequency per unit time to overcome the obstacles |
| ρ | Dislocation density |
| ρ_{MX} | Total number density of MX |

| | |
|----------------------|---|
| ρ_{MXi} | Number density of MX inside a subgrain or an HRHD zone |
| ρ_0 | Initial number density of MX inside a subgrain |
| ρ_Z | Number density of Z-phase |
| σ | Applied stress |
| σ_ε | Strength for a specific strain ε (%) |
| σ_{1E5} | Rupture strength for 1E5 h |
| σ_{tr} | Rupture strength |
| σ_b | Applied stress for individual test in <i>Gr.IIIb</i> , see Figure 33 |
| σ_{bi} | Imaginary stress corresponding to σ_b when stress concentration is released due to recovery |
| σ_{bav} | Average of σ_b , see Figure 34 |
| σ_{biav} | Average of σ_{bi} , see Figure 34 |
| σ_{xx} | See XX |
| a | Interplanar spacing |
| b | Length of the Burgers vector |
| d | Subgrain size |
| max | Maximum |
| mcr | Minimum creep rate for individual creep curve |
| r | Correlation coefficient |
| t | Creep time or tempering time |
| t -value | Reliability index in a regression analysis |
| t_{IIIa} | Average of t_ε or t_r for <i>Gr.IIIa</i> |
| t_ε | Time to strain, ε (%) |
| t_{b0} | Imaginary time to rupture corresponding to for <i>Gr.IIIb</i> when stress concentration for <i>Gr.IIIa</i> is maintained, see Figure 33 |
| t_{bi} | Time to rupture corresponding to σ_{bi} , see Figure 33 |
| t_{b0av} | Average of t_{b0} |
| t_{biav} | Average of t_{bi} |
| t_i | Time to strain corresponding to ε_i |
| t_r | Time to rupture |
| t_{RHU} | Average of t_ε or t_r for RHU etc. |
| t_{T122} | Average of t_ε or t_r for Grade T122 etc. |
| t_{xx} | See XX |
| t_Z | Start time for Z-phase formation |
| ASME | The American Society of Mechanical Engineering |
| C | Larson–Miller constant |
| C_s | Larson–Miller constant calculated based on strain rate |
| C_{MG} | Monkman-Grant constant |
| C_{xx} | See XX |
| DFRP | Dissolving and finely re-precipitation |
| DIN | Deutsches Institut für Normung |
| EL | Rupture elongation |
| <i>Gr.IIIa</i> | Data group in which severe degradation is confirmed |

| | |
|-------------------------------|--|
| HRC | Rockwell hardness C scale |
| HRHD | Heterogeneous recovery and heterogeneous deformation |
| HV | Vickers hardness |
| LMP | Larson–Miller parameter |
| $M_{23}C_6$ | (Cr,Fe,Mo,W) ₂₃ C ₆ carbide |
| MCR | Minimum creep rate for each data group |
| MX | Carbonitride of (Cr,Nb,V)(C,N) with a cubic structure |
| N_{av} | Available nitrogen concentration (at%) |
| NCR | Normalized creep rate, $\dot{\epsilon}/MCR$ |
| NIMS | National Institutes for Materials Science in Tsukuba, Japan |
| P | Time-Temperature parameter or Lrson-Miller parameter, $P = T(\log t + C)$ |
| $P_{HRHD} = V_{max}/V_{tr}$ | HRHD parameter, ratio of average V_{tr} and average V_{max} for <i>Gr.II</i> |
| $P_{LavesC} = Q_{max}/Q_{tr}$ | Laves phase parameter, ratio of Q_{tr} and Q_{max} |
| $P_{MX} = Q_i - Q_{4W}$ | MX parameter, difference between individual Q and the corresponding Q for 4W |
| PAGB | Prior austenitic grain boundary |
| PAGS | Prior austenite grain size |
| PAGSn | Prior austenite grain size number |
| PS | Proof stress |
| Q | Activation energy |
| $[Q]$ | First term of right side of Equation 2 |
| Q_{IIIa} | Q for <i>Gr.IIIa</i> |
| Q_{ϵ} | Q for ϵ (%) |
| Q_{max} | Maximum value for Q |
| Q_{RHU} | Q for heat RHU |
| Q_D | Activation energy for diffusion |
| Q_s | Activation energy calculated based on strain rate |
| $[Q_s]$ | First term of right side of Equation 5, $Q_s/2.3RT$ |
| Q_{xx} | See XX |
| QVC | Q , V , and C |
| $\Delta[QVC]$ analysis | See Table 6 |
| $[QVC]_s$ | $[Q_s]$, $[V_s]$, and C_s |
| $\Delta[QVC]_s$ analysis | See Table 3 |
| R | Gas constant |
| RA | Reduction of area |
| ΔS | The entropy change in an activation process |
| SBSD | Subgrain boundary strengthening by dislocations |
| SR | Stress relieving |
| T | Temperature in K |
| T_b | Average temperature of <i>Gr.IIIb</i> , see Figure 33 |
| TEM | Transmission electron microscopy |
| TP | Tempering parameter, $P = T(\log t + C)$ |
| T_{bi}/T_b | Ratio of imaginary temperature T_{bi} (°C) and average temperature T_b (°C) for <i>Gr.IIIb</i> |

| | |
|------------|---|
| TLF | Start time for Laves phase formation |
| TTP | Time-temperature-precipitation |
| TS | Tensile strength |
| TZF | Start time for Z-phase formation |
| V | Activation volume |
| $[V]$ | Second term of right side of Equation 2, $\sigma V/2.3RT$ |
| $V_{0.5}$ | Activation volume at 0.5% strain for $Gr.I$ |
| V_{free} | Free vanadium in at%, $V_{free} = V - N_{av}$ |
| V_s | Activation volume calculated based on strain rate |
| $[V_s]$ | Second term of right side of Equation 5, $\sigma V_s/2.3RT$ |
| V_{xx} | See XX |
| (VN) | Hardening parameter owing to VN defined by Equation 15 |
| XX | Suffix for T, σ, t , and QVC . Details are explained in Section 3. |
| Z | Coordinate number |

References

- Abe, F., Araki, H., & Noda, T. (1991). The effect of tungsten on dislocation recovery and precipitation behavior of low-activation martensitic 9Cr steels. *Metallurgical Transactions A*, 22A, 1991-2225. <https://doi.org/10.1007/BF02664988>
- Abe, F. (2006). Metallurgy for long-term stabilization of ferritic steels for thick section boiler components in USC power plant at 650 °C. In *Proceedings of the 8th Liege Conference on Materials for Advanced Power Engineering*, 2006, September 18-20, 2006, Liege, Belgium (pp. 965-980). Forschungszentrum Juelich, Germany. Retrieved from https://www.fz-juelich.de/zb/DE/Home/home_node.html
- Abe, F., Tabuchi, M., Semba, H., Igarashi, M., Yoshizawa, M., Komai, N., & Fujita, A. (2007a), Feasibility of MARBN steel for application to thick section boiler components in USC power plant at 650°C. *5th EPRI International Conference*, October 3-5, 2007, Marco Island, Florida, USA. <https://doi.org/10.1361/cp2007epri0092> Retrieved from https://www.asminternational.org/web/hts/am-p-magazine//journal_content/56/10192/CP2007EPRI0092/PUBLICATION
- Abe, F., Tanaka, H., & Murata, M. (2007b), Impurity effects on heat-to-heat variation in creep life for some heat resistant steels. *Proc. of BALTICA VII Intern. Conf. on Life Management and Maintenance for Power Plants*, June 12-14, Helsinki, Finland (pp.171-184). Retrieved from <https://www.researchgate.net/publication/288288250>
- Abe, F., Ohba, T., Miyazaki, H., Toda, Y., & Tabuchi, M. (2018). Long-term creep strength and rupture ductility of W-Mo-balanced 9Cr steel. In *Proceedings of 44th MPA-Seminar*, October 17-18, 2018, Stuttgart, Germany (pp. 1-15). Retrieved from <https://seminar.mpa.uni-stuttgart.de/s-2018/SitePages/Program.aspx>
- Aghajani, A., Somsen, Ch., & Eggeler, G. (2009). On the effect of long-term creep on the microstructure of a 12% chromium tempered martensite ferritic steel. *Acta Materialia*, 57, 5093-5106. <https://doi.org/10.1016/j.actamat.2009.07.010>
- Bazazi, A. A. (2009). *Evolution of microstructure during long-term creep of a tempered martensite ferritic steel*, (Dissertation of Dr. Eng.). Ruhr-University, Bochum, Germany. Retrieved from <https://www-brs.ub.ruhr-uni-bochum>
- Danielsen, H. K. (2007). *Z-Phase in 9-12%Cr steels* (Dissertation of Ph. D.). Technical University of Denmark, Lyngby, Denmark. Retrieved from <https://backend.orbit.dtu.dk/ws/files/4899462/HilmarThesis.pdf>
- Di-Gianfrancesco, A., Vipraio, S. T., & Venditti, D. (2013). Long-term microstructural evolution of 9-12%Cr steel grades for steam power generation plants. *Procedia Engineering*, 55, 27-35. <https://doi.org/10.1016/j.proeng.2013.03.214>
- Dudko, V., Belyakov, A., Molodov, D., & Kaibyshev, R. (2013). Microstructure evolution and pinning of boundaries precipitates in a 9 pct Cr heat resistant steel during creep. *Metallurgical and Materials Transactions A*, 44A, S162-S172. <https://doi.org/10.1007/s11661-011-0899-1>

- Dudova, N., Plotnikova, A., Molodov, A., Belyakov, A., & Kaibyshev, R. (2012). Structural changes of tempered martensitic 9%Cr–2%W–3%Co steel during creep at 650 °C. *Materials Science and Engineering: A*, 534, 632-639. <https://doi.org/10.1016/j.msea.2011.12.020>
- Ennis, P. J., & Czyrska-Filemonowicz, A. (2003). Recent advances in creep-resistant steels for power plant applications. *Sadhana*, 28, 709-730. <https://doi.org/10.1007/BF02706455>
- Esherby, J. D. (1956). The continuum theory of lattice defects. In F. Seitz & D. Turnbull (Eds.), *Solid State Physics: Advances in Research and Applications* (Vol. 3, pp. 79-145). NY. Academic Press Inc. [https://doi.org/10.1016/S0081-1947\(08\)60132-0](https://doi.org/10.1016/S0081-1947(08)60132-0)
- Fedoseeva, A., Nikitin, I., Dudova, N., & Kaibyshev, R. (2019). Creep behavior and microstructure of a prospective Re-containing 10%Cr-3%Co-3%W martensitic steel. In *Joint EPRE-123HiMAT International Conference on Advances in High-Temperature Materials: Proceedings from EPRI's 9th International Conference on Advances in Materials Technology for Fossil Power Plants and the 2nd International 123HiMAT Conference on High-Temperature Materials*, October 21-24, 2019, Nagasaki, Japan, ASM International (pp. 217-226). Retrieved from http://www.123himat-2019.mtl.titech.ac.jp/Leaflet_FinalProgram_191015_FinalVersion.pdf
- Gu, Y., West, G. D., & Thomson, R. C. (2014). Investigation of creep damage and cavitation mechanism in P92 steels. In *Advances in Materials Technology for Fossil Power Plants: Proceedings from the 7th International Conference (EPRI2013)*, October 22nd-25th, Hawaii, USA. ASM International, (pp. 596-606). Retrieved from https://repository.lboro.ac.uk/articles/Investigation_of_creep_damage_and_cavitation_mechanisms_in_P92_steels/9233744
- Hättestrand, M., & Andren, H.-O. (2001). Evaluation of particle size distribution of precipitates in a 9% chromium steel using energy filtered transmission electron microscopy. *Micron*, 32, 789-797. [https://doi.org/10.1016/S0968-4328\(00\)00086-X](https://doi.org/10.1016/S0968-4328(00)00086-X)
- Hald, J. (2008). Microstructure and long-term creep properties of 9-12% Cr steels. *International Journal of Pressure Vessels and Piping*, 85, 30-37. <https://doi.org/10.1016/j.ijpvp.2007.06.010>
- Hasegawa, Y. (2014). Grade 92 creep-strength-enhanced ferritic steel. In A. Shibli (Ed.), *Coal Power Plant Materials and Life Assessment - Development and Applications* (pp. 52-86). Cambridge, UK, Woodhead Publishing. <https://doi.org/10.1533/9780857097323.1.52>
- Hashizume, R., Tamura, O., Miki, K., Azuma, T., Ishiguro, T., Murata, Y., & Morinaga, M. (2009). Beneficial effect of Re on the long-term creep strength of high Cr ferritic heat resistant steels. *Tetsu-to-Hagane*, 95, 176-185. <https://doi.org/10.2355/tetsutohagane.95.176>
- Hayakawa, H., Terada, D., Yoshida, F., Nakashima, H., & Goto, Y. (2003a). Evaluation of mobile dislocation density of modified 9Cr-1Mo steel by stress change test. *Tetsu-to-Hagane*, 89, 1076-1081. https://doi.org/10.2355/tetsutohagane1955.89.10_1076
- Hayakawa, H., Terada, D., Yoshida, F., Nakashima, H., & Goto, Y. (2003b). Characterization of creep deformation mechanism and evaluation of dislocation mobility of modified 9Cr-1Mo steel by stress change test. *Journal of Japan Institute of metals*, 67, 22-26. https://doi.org/10.2320/jinstmet1952.67.1_22
- Hayakawa, H., Nakashima, S., Kusumoto, J., Kanaya, A., Terada, D., Yoshida, F., & Nakashima, H. (2007). Evaluation of creep deformation mechanism of heat resistant steel by stress change test. In *Proceedings of jmsr.ccsenet.org Journal of Materials Science Research Vol. 10, No. 2; 2021 60 CREEP8, 8th International conference on Creep and Fatigue at Elevated Temperatures*, July 22-26, 2007, San Antonio, Texas (CREEP2007-26501, pp. 1–10). ASME. Retrieved from <https://asmedigitalcollection.asme.org/proceedings>
- Iseda, A., Teranishi, H., Yoshikawa, K., Masuyama, F., Daikoku, T., & Haneda, H. (1988). Development of high strength 12Cr-1Mo-1W-V-Nb steel tube for boiler. *The Thermal and Nuclear Power*, 39(8), 897-907. Retrieved from <https://www.tenpes.or.jp>
- Jiang, J., Zhu, L., & Wang, Y. (2013). Hardness variation in P92 heat-resistant steel based on microstructural evolution during creep. *Steel Research International*, 84, 732-739. <https://doi.org/10.1002/srin.201200265>
- Kabadwal, A., Tamura, M., Shinozuka, K., & Esaka, H. (2010). Recovery and precipitate analysis of 9 pct Cr-1 pct MoVNb steel during creep. *Metallurgical and Materials Transactions A*, 41A, 364-379. <https://research.rug.nl/en/publications/3f2b8603-89de-486d-8b3e-2974fb054c6c>

- Kadoya, Y. & Shimizu, E. (2000). Behavior of dislocation substructures during high temperature creep of high-Cr ferritic steels. *Tetsu-to-Hagane*, 86(3), 189-195. DOI:10.2355/tetsutohagane1955.86.3_189 retrieved from isij.or.jp
- Karashima, S., Iikubo, T., Watanabe, T., & Oikawa, H. (1971). Transmission electron microscopy of substructures developed during high-temperature creep in alpha-iron. *Transactions of JIM*, 12, 369-374. <https://doi.org/10.2320/matertrans1960.12.369>
- Karashima, S., Iikubo, T., & Oikawa, H. (1972). On the high-temperature creep behavior and substructures in alpha-iron single crystal. *Transactions of JIM*, 13, 176-181. <https://doi.org/10.2320/matertrans1960.13.176>
- Kimura, K., Suzuki, K., Toda, Y., Kushima, H., & Abe, F. (2002). Precipitation of Z-phase and degradation behavior of mod.9Cr-1Mo steel. In *Proceedings of the 7th Liege Conference on Materials for Advanced Power Engineering 2002*, (pp. 1171-1180). Forschungszentrum Juelich, Germany. Retrieved from https://www.fz-juelich.de/zb/DE/Home/home_node.html
- Kimura, K., Sawada, K., Kubo, K., & Kushima, H. (2004). Influence of stress on degradation and life prediction of high strength ferritic steels. *Proceedings of the ASME Pressure Vessels and Piping Division*, July 25-29, 2004, San Diego, California, USA. ASME, PVP2004-2566, (pp. 11-18) <https://doi.org/10.1115/PVP2004-2566>
- Kimura, K. (2009). Creep rupture life prediction of creep resistant steels. *Journal of Japan Institute of Metals*, 73(5), 323-333. <https://doi.org/10.2320/jinstmet.73.323>
- Kimura, H., Sato, T., Bergins, C., Imano, S., & Saito, E. (2011). Development of technologies for improving efficiency of large coal-fired thermal power plants. *Hitachi Review*, 60(7), 365-371. Retrieved from http://www.hitachi.com/rev/pdf/2011/r2011_07_102.pdf
- Kimura, K. & Takahashi, Y. (2012a). Evaluation of long-term creep strength of ASME Grades 91, 92, and 122 type steels. In *ASME 2012 Pressure Vessels and Piping Conference*, July 15-19, 2012, Toronto, Ontario, Canada. ASME, PVP2012-78323, (pp. 309-316) <https://doi.org/10.1115/PVP2012-78323>
- Kimura, K., Sawada, K., Kushima, H., & Toda, Y. (2012b). Microstructural stability and long-term creep strength of Grade 91. *Energy Materials: Materials Science and Engineering for Energy System*. 4, 176-183. Retrieved from DOI:10.1179/174892312X13269692038897
- Kimura, K., Sawada, K., Kushima, H., & Toda, Y. (2013). Influence of chemical composition and heat treatment on long-term creep strength of Grade 91 steel. *Procedia Engineering*, 55, 2-9. <https://doi.org/10.1016/j.proeng.2013.03.211>
- Kocer, C., Abe, T., & Soon, A. (2009). The Z-phase in 9-12% Cr ferritic steels: A phase stability analysis. *Materials Science and Engineering A*, 505, 1-5. <https://doi.org/10.1016/j.msea.2008.10.028>
- Kushima, H., Kimura, K., & Abe, F. (1999). Degradation of mod. 9Cr-1Mo steel during long-term creep deformation. *Tetsu-to-Hagane*, 85, 841-847. https://doi.org/10.2355/tetsutohagane1955.85.11_841
- Kushima, H., Kimura, K., & Abe, F. (2002). Long-term creep strength prediction of high Cr ferritic creep resistant steels. In *Proceedings of the 7th Liege Conference on Materials for Advanced Power Engineering 2002*, (pp. 1581-1590). Forschungszentrum Juelich, Germany. Retrieved from https://www.fz-juelich.de/zb/DE/Home/home_node.html
- Larson, F. R., & Miller, J. (1952). A time-temperature relationship for rupture and creep stresses. *Transactions of the American Institute of Mining and Metallurgical Engineers*, 74, 765-775. Retrieved from <https://search.lib.virginia.edu/catalog/u744571>
- Lim, R., Sauzay, M., Dalle, F., Tournie, I., Bonnaillie, P., & Gourgues-Lorenzon, A. -F. (2011). Modelling and experimental study of the tertiary creep stage of Grade 91 steel. *International Journal of Fracture*, 169, 213-228. <https://link.springer.com/article/10.1007/s10704-011-9585-y>
- Maruyama, K., Nakamura, J., & Yoshimi, K. (2015). Prediction of long-term creep rupture life of Grade 122 steel by multi-region analysis, *J. Pressure Vessel Technol.* Apr 2015, 137(2): 021403 (5 pages) Paper No: PVT-14-1066. <https://doi.org/10.1115/1.4028203>
- Masuyama, F., Komai, N., Yokoyama, T., Yamamoto, S., Miyata, K, and Igarashi, M. (1998). 3-year experience with 2.25 Cr-1.6 W (HCM2S) and 12Cr-0.4Mo-2W (HCM12A) steel tubes in a power boiler, *JSME International Journal*, 41, 1098-1104. http://www.jstage.jst.go.jp/article/jsmeb1993/41/4/41_4_1098/_pdf

- Masuyama, F. (2001). History of power plants and progress in heat resistant steels. *ISIJ International*, 41, 612-625. <https://doi.org/10.2355/isijinternational.41.612>
- Mehrer, H. (2007). *Diffusion in Solids*, Berlin Heidelberg: Springer-Verlag <https://link.springer.com/book/10.1007/978-3-540-71488-0>
- Mitsuhara, M. (2022) Private communication.
- Monkman F. C. & Grant, N. J. (1956). An empirical relationship between rupture life and minimum creep rate in creep-rupture tests. *Proceedings of American Society for Testing and Materials*, 56, 593-620. Retrieved from http://www.astm.org/DIGITAL_LIBRARY/STP/MMR/PAGES/PRO1956-56.htm
- Morooka, S., Tomota, Y., Adachi, Y., Morito, S., & Kamiyama, T. (2008a). Hierarchical characterization by EBSD and neutron diffraction on heterogeneous deformation behavior of a martensitic steel. *Tetsu-to-Hagane*, 94, 313-320. <https://doi.org/10.2355/tetsutohagane.94.313>
- Morooka, S., Tomota, Y., & Kamiyama, T. (2008b). Heterogeneous deformation behavior studied by in situ-neutron diffraction during tensile deformation for ferrite, martensite and pearlite steels. *ISIJ International*, 48(4), 525-530. <https://doi.org/10.2355/isijinternational.48.525>
- Mura, T., & Mori, T. (1976). *Micromechanics-Dislocation and Inclusions*. Tokyo: Baihukan. ASIN: B000JA16HW. Retrieved from <https://iss.ndl.go.jp/books/R100000002-I000001129159-00>
- Muroki, M. (2017). The way to high efficiency boilers for power plant led by Ni-based alloy: from 600 °C -class ultra-super critical (USC) boilers to 700 °C-class advanced ultra-super-critical (A-USC) boilers. *IHI Engineering Review*, 50(1), 26-29. Retrieved from <http://www.ihico.jp/en/>
- Narita, K. (1975). Physical chemistry of the Groups IVa (Ti, Zr), Va (V, Nb, Ta) and the rare earth elements in steel. *Transaction of the Iron and Steel Institute of Japan*, 15, 145-152. <https://doi.org/10.2355/isijinternational1966.15.145>
- Nie, M., Zhang, J., Huang, F., Liu, J. W., Zhu, X. K., Chen, Z. L., & Ouyang, L. Z. (2014). Microstructure evolution and life assessment of P92 steel during long-term creep. *Journal of Alloys and Compounds*, 588, 348-356. <https://doi.org/10.1016/j.jallcom.2013.11.080>
- NIMS: Data Sheets on the Elevated-Temperature Properties of 9Cr-1Mo-V-Nb Steel Tubes for Boilers and Heat Exchangers, 9Cr-1Mo-V-Nb Steel Plates for Boilers and Pressure Vessels, and 9Cr-1Mo-V-Nb Steel Seamless Pipe for High Temperature Service, No. 43A. (2014). Tsukuba, Japan. Retrieved from http://www.nims.go.jp/mits/english/creep_lst_e.htm
- NIMS: Data Sheets on the Elevated-Temperature Properties of 9Cr-0.5Mo-1.8W-V-Nb Steel Tubes for Power Boilers and 9Cr-0.5Mo-1.8W-V-Nb Steel Pipe for High Temperature Service, No. 48B. (2018). Tsukuba, Japan. Retrieved from http://www.nims.go.jp/mits/english/creep_lst_e.htm
- NIMS: Data Sheets on the Elevated-Temperature Properties of 11Cr-2W-0.4Mo-1Cu-Nb-V stainless steel pipe for high temperature service (KA-SUS 410J3 TP), 11Cr-2W-0.4Mo-1Cu-Nb-V stainless steel plate for power plants (KA-SUS 410J3), and 11Cr-2W-0.4Mo-1Cu-Nb-V stainless steel tube for power boilers (KA-SUS 410J3 TB), No. 51B. (2020). Tsukuba, Japan. Retrieved from http://www.nims.go.jp/mits/english/creep_lst_e.htm
- NIMS: Data Sheets on the Elevated-Temperature Properties of 12Cr-2W-0.4Mo-1Cu-Nb-V stainless steel tube for power boilers (KA-SUS 410J3 DTB), No. 52B. (2021). Tsukuba, Japan. Retrieved from http://www.nims.go.jp/mits/english/creep_lst_e.htm
- Norton, F. H. (1929). *The Creep of Steel at High Temperatures*. NY: McGraw-Hill Book Co. Retrieved from <https://archive.org/details/creepofsteelathi00nort>
- Oikawa, H. (1982). Lattice self-diffusion in solid iron: A critical review. *Technology Reports of the Tohoku University*, 47, 67-77. Retrieved from <http://www.worldcat.org/title/technology-reports-of-thetohoku-university/oclc/2451160>
- Panait, C. G., Zielinska-Lipiec, A., Koziel, T., Czyska-Filemonowicz, A., Gourgues-Lorenzon, A.-F., & Bendick, W. (2010). Evolution of dislocation density, size of subgrains and MX-type precipitates in a P91 steel during creep and during thermal ageing at 600 °C for more than 100 000 h. *Materials Science and Engineering A*, 527, 4062-4069. <https://doi.org/10.1016/j.msea.2010.03.010>

- Pesicka, J., Aghajani, A., Somen, Ch., Hartmaier, A., & Eggeler, G. (2010). How dislocation substructures evolve during long-term creep of a 12% Cr tempered martensitic ferritic steel. *Scripta Materialia*, 62, 353-356. <https://doi.org/10.1016/j.scriptamat.2009.10.037>
- Parker, J. D., & Siefert, J. A. (2018). Creep fracture in tempered martensitic steels. *International Journal of Petrochemical Science & Engineering*, 3(1), 00068. <https://doi.org/10.15406/ipcse.2018.03.00068>
- Sawada, K., Maruyama, K., Komine, R., & Nagae, Y. (1997). Microstructural changes during creep and life assessment of mod. 9Cr-1Mo steel. *Tetsu-to-Hagane*, 83, 466-471. https://doi.org/10.2355/tetsutohagane1955.83.7_466
- Sawada, K., Taneike, M., Kimura, K., & Abe, F. (2004). Effect of nitrogen content on microstructural aspects and creep behavior in extremely low carbon 9Cr heat-resistant steel. *ISIJ International*, 44, 1243-1249. <https://doi.org/10.2355/isijinternational.44.1243>
- Sawada, K., Kushima, H., & Kimura, K. (2006). Z-phase formation during creep and aging in 9-12% Cr heat resistant steels. *ISIJ International*, 46, 769-775. <https://doi.org/10.2355/isijinternational.46.769>
- Sawada, K., Kushima, H., Kimura, K., & Tabuchi, M. (2007). TTP diagram of Z-phase in 9-12% Cr heat-resistant steels. *ISIJ International*, 47, 733-739. <https://doi.org/10.2355/isijinternational.47.733>
- Sawada, K., Kushima, H., Tabuchi, M., & Kimura, K. (2011). Microstructural degradation of Gr.91 steel during creep under low stress. *Materials Science and Engineering A*, 528, 5511-5518. <https://doi.org/10.1016/j.msea.2011.03.073>
- Sawada, K., Kushima, H., Hara, T., Tabuchi, M., & Kimura, K. (2014). Heat-to-heat variation of creep strength and long-term stability of microstructure in Grade 91 steels. *Materials Science and Engineering A*, 597, 164-170. <http://dx.doi.org/10.1016/j.msea.2013.12.088>
- Sawada, K., & Kimura, K. (2019). Stability of long-term creep strength and microstructure in high Cr steels. *Bulletin of The Iron and Steel Institute of Japan*, 24, 68-72. Retrieved from <https://www.isij.or.jp>
- Schoeck, G. (1980). Thermodynamics and thermal activation of dislocations. In F. R. N. Nabarro (Ed.), *Dislocations in Solids volume 3 Moving Dislocations* (pp. 63-159). Amsterdam: North-Holland Pub. Co. <https://doi.org/10.1115/1.3157584>
- Sherby, O. D., Orr, R. L., & Dorn, J. E. (1953). *Creep Correlations of Metals at Elevated Temperatures in 25th Techn. Rpt. Sr. 22 Issue 25 N7-on-295* (pp. 1-44). Berkeley, CA.: University of California. Retrieved from <http://www.dtic.mil/dtic/tr/fulltext/u2/005978.pdf>
- Sikka, V. K., Cowgill, M. G., & Roberts, B. W. (1983). Creep properties of modified 9 Cr-1Mo steel. In J. W. Davis & D. J. Michel (Eds.), *Proceedings of Topical Conference on Ferritic Alloys for Use in Nuclear Energy Technologies, Snowbird, Utah, June* (pp. 413-423). American Nuclear Society, La Grange Park, IL. <https://doi.org/10.2172/5687534>
- Straub, S., Meier, M., Ostermann, J., & Blum, W. (1993). Entwicklung der mikrostruktur und der festigkeit des stahles X20CrMoV 12-1 bei 823 K wahrend zeitstandbeanspruchung und gluhung. *VGB Kraftwerkstechnik*, 73, 744-752. Retrieved from <https://www.osti.gov/etdeweb/biblio/5792082>
- Sundman, B. Jansson, B., & Andersson, J.-O. (1985). The thermo-calc databank system. *Calphad*, 9(2), 153-190. doi:10.1016/0364-5916(85)90021-5
- Suzuki, K., Kumai, S., Kushima, H., Kimura, K., & Abe, F. (2000). Heterogeneous recovery and precipitation of Z-phase during long-term creep deformation of modified 9Cr-1Mo steel. *Tetsu-to-Hagane*, 86, 550-557. https://doi.org/10.2355/tetsutohagane1955.86.8_550
- Suzuki, K., Kumai, S., Kushima, H., Kimura, K., & Abe, F. (2003). Precipitation of Z-phase and precipitation sequence during creep deformation of mod.9Cr-1Mo steel. *Tetsu-to-Hagane*, 89, 691-698. https://doi.org/10.2355/tetsutohagane1955.89.6_691
- Tamura, M., Hayakawa, H., Yoshitake, A., Hishinuma, A., & Kondo, T. (1988). Phase stability of reduced activation ferritic steel 8%Cr-2%W-0.2%V-0.04%Ta-Fe. *Journal of Nuclear Materials*, 155-157, 620-625. [https://doi.org/10.1016/0022-3115\(88\)90384-4](https://doi.org/10.1016/0022-3115(88)90384-4)
- Tamura, M., Esaka, H., & Shinozuka, K. (1999). Stress and temperature dependence of time to rupture of heat resisting steels. *ISIJ International*, 39, 380-387. <http://dx.doi.org/10.2355/isijinternational.39.380>

- Tamura, M., Esaka, H., & Shinozuka, K. (2000). Physical meaning of the new creep rupture equation for heat resisting steels. *Materials Transaction, JIM*, 41, 272-278. <https://doi.org/10.2320/matertrans1989.41.272>
- Tamura, M., Abe, F., Shiba, K., Sakasegawa, H., & Tanigawa, H. (2013). Larson–Miller constant of heat-resistant steel. *Metallurgical and Materials Transactions A*, 44, 264-52661. <https://doi.org/10.1007/s11661-013-1631-0>
- Tamura, M. (2015). Method of estimating the long-term rupture strength of 11Cr-2W-0.4Mo-1Cu-Nb-V steel. *Metallurgical and Materials Transactions A*, 46, 1958-1972. <https://doi.org/10.1007/s11661-015-2784-9>
- Tamura, M. (2017). Verification of equation for evaluating dislocation density during steady-state creep of metals. *Journal of Materials Science Research*, 6(2), 20-62. <https://doi.org/10.5539/jmsr.v6n2p20>
- Tamura, M. & Abe, F. (2021a). Analysis on degradation in creep strength of 9Cr-W martensitic steel. *Journal of Materials Science Research*, 10(1), 1-27. <https://doi.org/10.5539/jmsr.v10n1p1>
- Tamura, M. & Abe, F. (2021b). Analysis of the degradation in the creep strength of Grades 91 and 92. *Journal of Materials Science Research*, 10(2), 1-70. <https://doi.org/10.5539/jmsr.v10n2p1>
- Tamura, M. (2022). Root cause of degradation in the creep strength of martensitic steel. *Journal of Materials Science Research*, 11(1), 1-39. <https://doi.org/10.5539/jmsr.v11n1p1>
- Taneike, M., Sawada, K., & Abe, F. (2003). Effect of Carbon concentration on precipitation behavior of $M_{23}C_6$ carbides and MX carbonitrides in martensitic 9Cr steel during heat treatment. *Metallurgical and Materials Transactions A*, 35A, 1255-1262. <http://dx.doi.org/10.1007/s11661-004-0299-x>
- Yan, W., Wang, W., Shan, Y.-Y., & Yang, K. (2013). Microstructural stability of 9-12%Cr ferrite/martensite heat-resistant steels. *Frontier Materials Science*, 7(1), 1-27. <https://doi.org/10.1007/s11706-013-0189-5>
- Yoshizawa, M., Igarashi, M., & Nishizawa, T. (2005). Effect of tungsten on the Ostwald ripening of $M_{23}C_6$ carbides in martensitic heat resistant steel. *Tetsu-to-Hagane*, 91, 272-277. https://doi.org/10.2355/tetsutohagane1955.91.2_272

Appendix

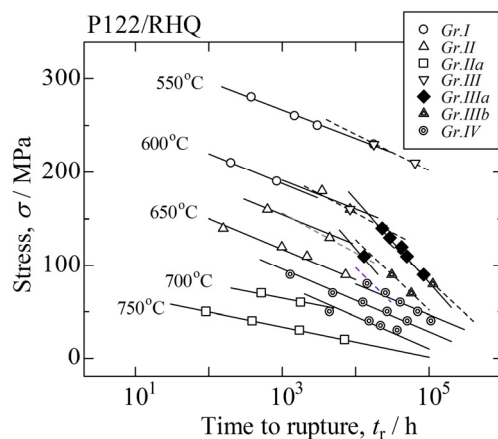


Figure A1. Stress vs. time to rupture relationship for P122/RHQ and regression lines for each data group

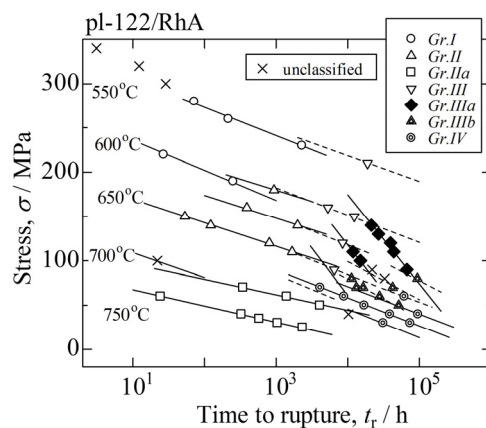


Figure A2. Stress vs. time to rupture relationship for pl-122/RhA and regression lines for each data group

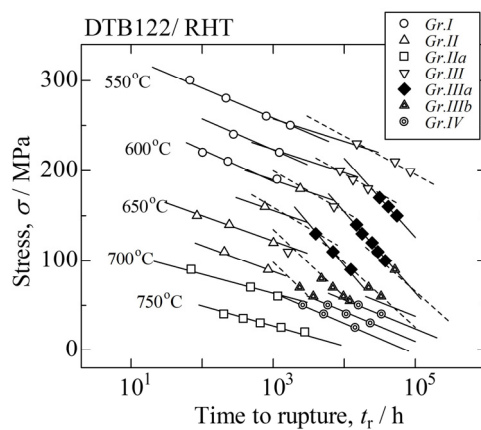


Figure A3. Stress vs. time to rupture relationship for DTB122/RHT and regression lines for each data group

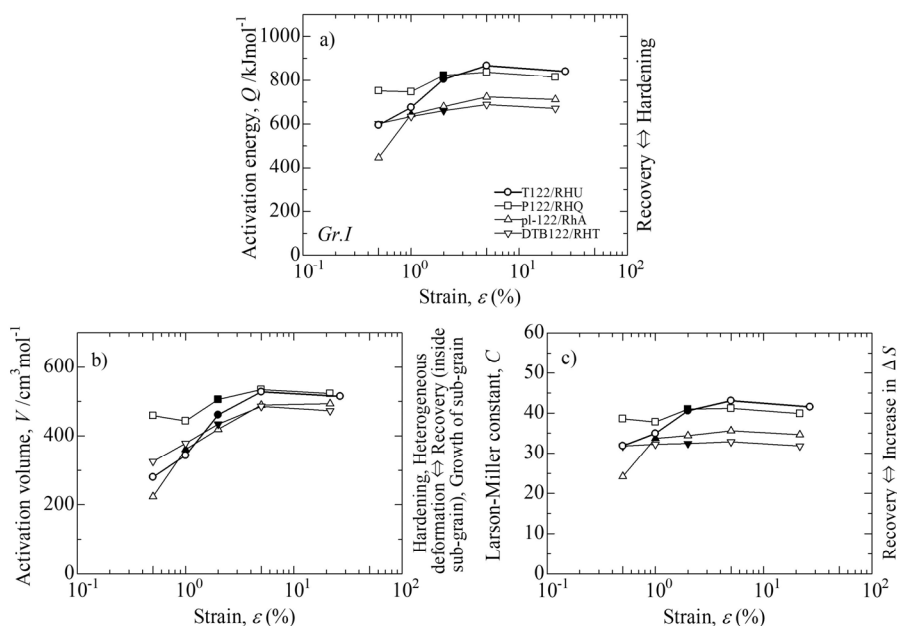


Figure A4. Results of the QVC analysis are shown as functions of creep strain for *Gr.s.I* of T122/RHU, P122/RHQ, pl-122/RhA, and DTB122/RHT; a) activation energy, b) activation volume, and c) Larson–Miller constant

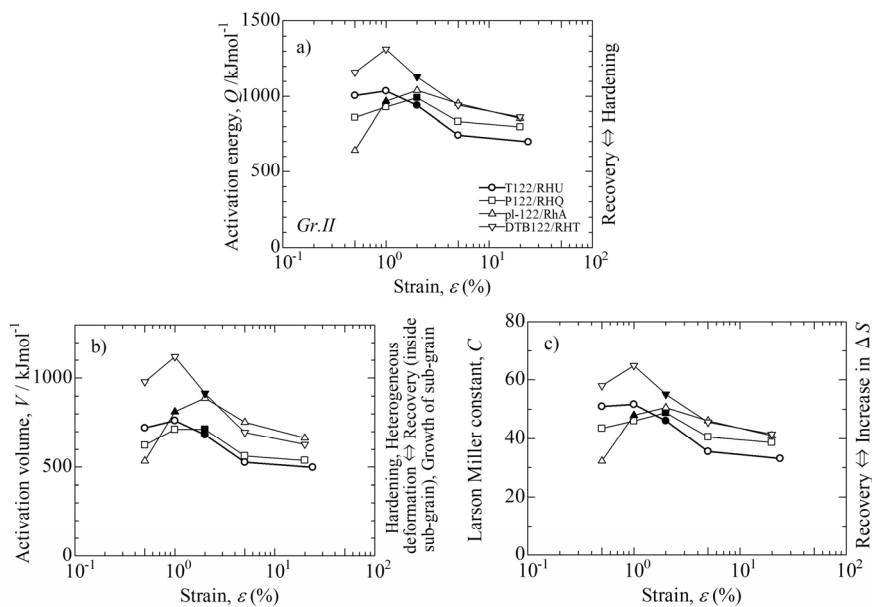


Figure A5. Results of the QVC analysis are shown as functions of creep strain for *Gr.s.II* of T122/RHU, P122/RHQ, pl-122/RhA, and DTB122/RHT; a) activation energy, b) activation volume, and c) Larson–Miller constant

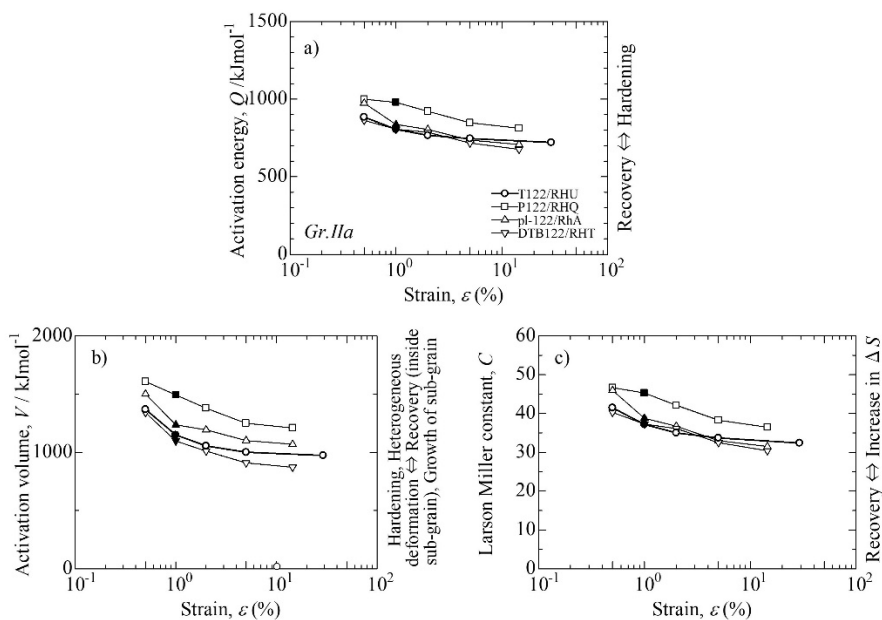


Figure A6. Results of the QVC analysis are shown as functions of creep strain for *Gr. IIa* of T122/RHU, P122/RHQ, pl-122/RhA, and DTB122/RHT; a) activation energy, b) activation volume, and c) Larson–Miller constant.

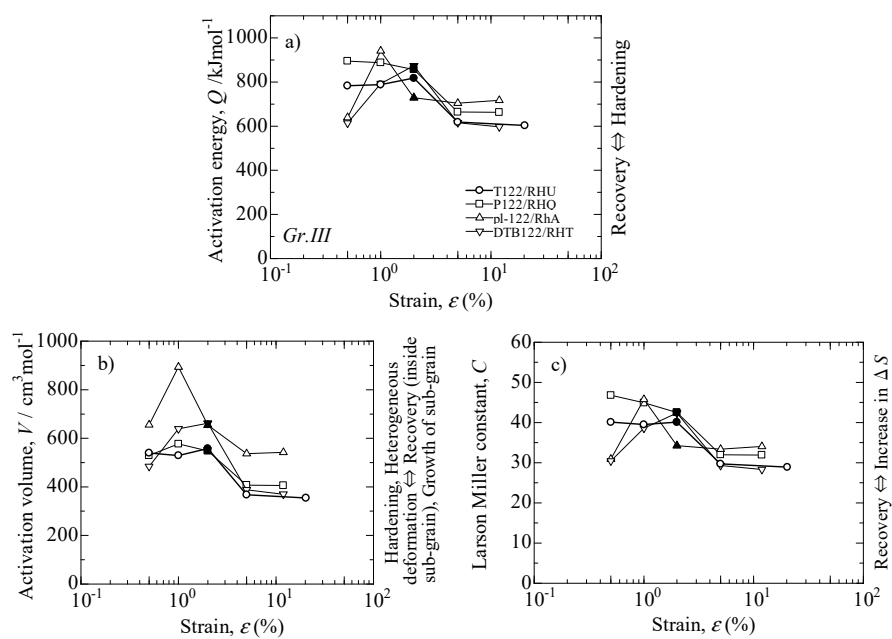


Figure A7. Results of the QVC analysis are shown as functions of creep strain for *Gr. III* of T122/RHU, P122/RHQ, pl-122/RhA, and DTB122/RHT; a) activation energy, b) activation volume, and c) Larson–Miller constant

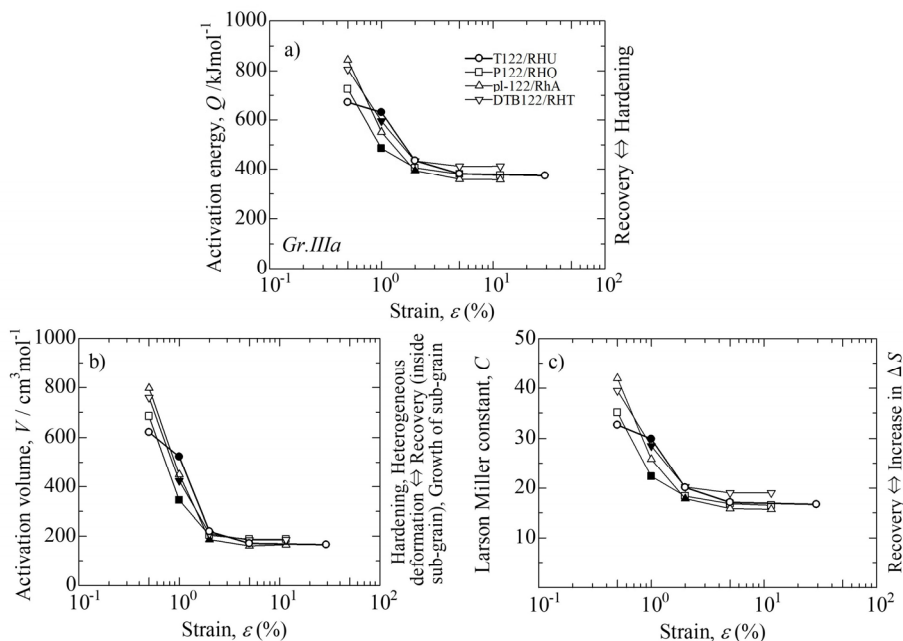


Figure A8. Results of the QVC analysis are shown as functions of creep strain for *Gr.IIIa* of T122/RHU, P122/RHQ, pl-122/RhA, and DTB122/RHT; a) activation energy, b) activation volume, and c) Larson–Miller constant

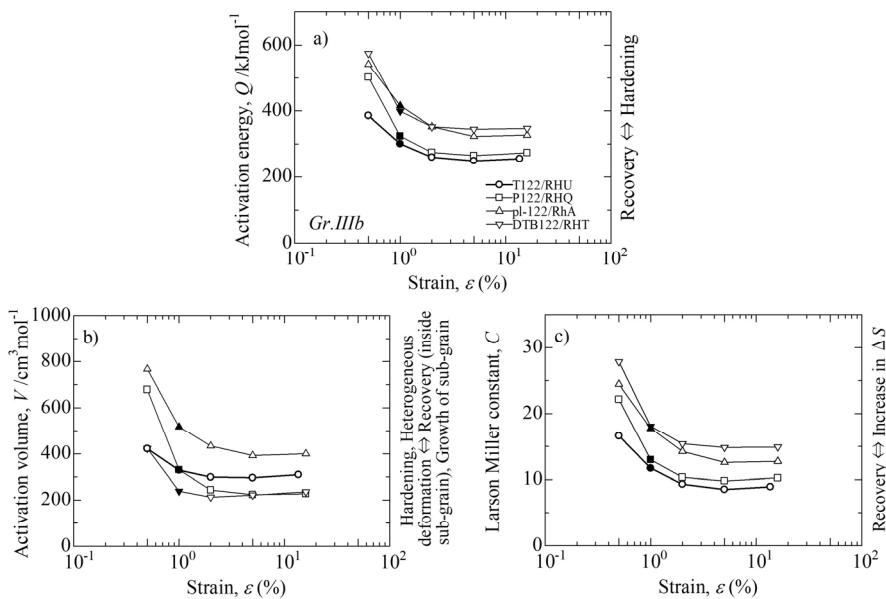


Figure A9. Results of the QVC analysis are shown as functions of creep strain for *Gr.IIIb* of T122/RHU, P122/RHQ, pl-122/RhA, and DTB122/RHT; a) activation energy, b) activation volume, and c) Larson–Miller constant

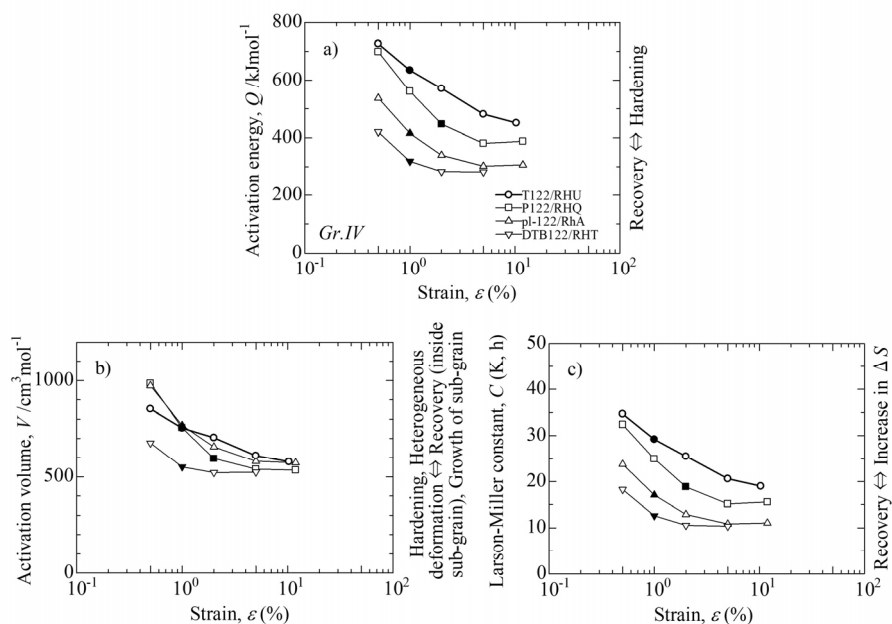


Figure A10. Results of the *QVC* analysis are shown as functions of creep strain for *Gr.IV* of T122/RHU, P122/RHQ, pl-122/RhA, and DTB122/RHT; a) activation energy, b) activation volume, and c) Larson–Miller constant

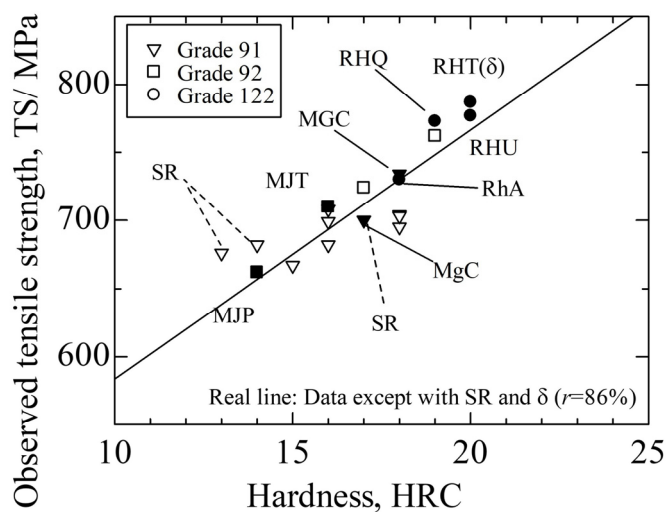


Figure A11. Correlation between observed HRC and TS. The regression line is given for the steel without δ -ferrite or SR treatment. The creep characteristics of steel with solid marks are explained in detail in this study

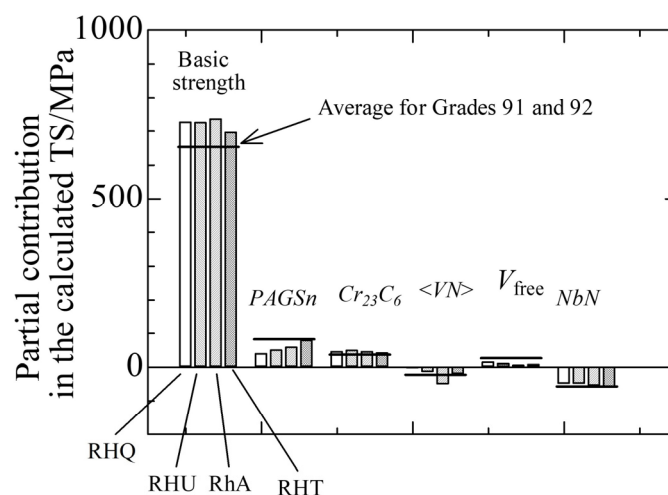


Figure A12. Partial contributions to the calculated TS for Grades 91, 92, and 122. The meanings of basic strength, $\langle VN \rangle$, and V_{free} are in Section 5.3

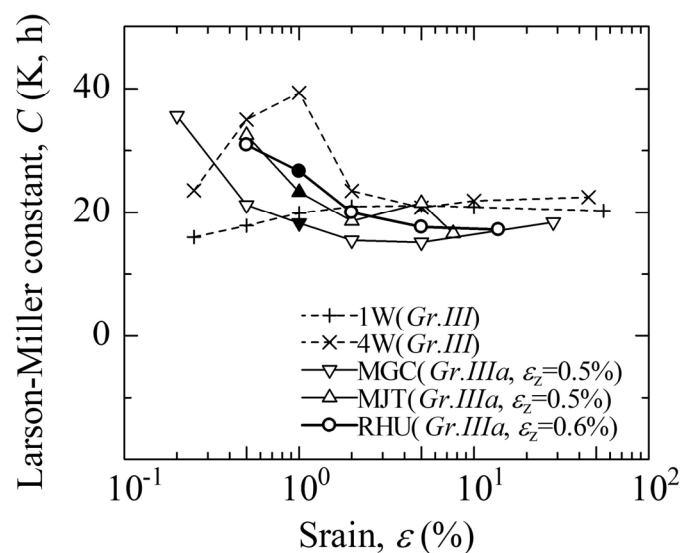


Figure A13. Larson–Miller constant, C , as functions of strain for *Gr.IIIa* of MGC, MJT, and RHU and for *Gr.III* of 1W and 4W. ϵ_z is a start strain for the Z-phase formation

Copyrights

Copyright for this article is retained by the author(s), with first publication rights granted to the journal.

This is an open-access article distributed under the terms and conditions of the Creative Commons Attribution license (<http://creativecommons.org/licenses/by/4.0/>).